



1949

**SEARCH FOR PARTICLES BEYOND THE STANDARD
MODEL WITH THE CMS DETECTOR**

PhD Thesis

János Karacsi

Supervisors: Dr. Viktor Veszprémi
Prof. Dr. Zoltán Trócsányi

UNIVERSITY OF DEBRECEN
Doctoral School of Physics

Debrecen, 2019

Készült
a Debreceni Egyetem
Fizikai Tudományok Doktori Iskolájának
Részecskefizika programja keretében
a Magyar Tudományos Akadémia
Atommagkutató Intézetben (MTA Atomki)

Prepared at
the University of Debrecen
Doctoral School of Physics,
and the Institute for Nuclear Research,
Hungarian Academy of Sciences

Ezen értekezést a Debreceni Egyetem Természettudományi és Informatikai Doktori Tanács Fizikai Tudományok Doktori Iskolájának Részecskefizika programja keretében készítettem a Debreceni Egyetem természettudományi doktori (PhD) fokozatának elnyerése céljából. Nyilatkozom arról, hogy a tézisekben leírt eredmények nem képezik más PhD disszertáció részét.

Debrecen, 2019

*Karancsi János
doktorjelölt*

Tanúsítjuk, hogy Karancsi János doktorjelölt 2010-2019 között a fent megnevezett Doktori Iskola Részecskefizika programjának keretében irányításunkkal végezte munkáját. Az értekezésben foglalt eredményekhez a jelölt önálló alkotó tevékenységével meghatározóan hozzájárult. Nyilatkozunk továbbá arról, hogy a tézisekben leírt eredmények nem képezik más PhD disszertáció részét. Az értekezés elfogadását javasoljuk.

Debrecen, 2019

*Dr. Trócsányi Zoltán, Dr. veszprémi Viktor
témavezetők*

Search for particles beyond the Standard Model with the CMS detector

Értekezés a doktori (PhD) fokozat megszerzése érdekében
a fizika tudományágban

Írta: Karancsi János okleveles fizikus

Készült a Debreceni Egyetem Fizikai Tudományok Doktori Iskolája
Részecskefizika programja keretében

Témavezetők: Dr. Veszprémi Viktor,
Prof. Dr. Trócsányi Zoltán

A doktori szigorlati bizottság:

elnök:	Prof. Dr. Nagy Ágnes
tagok:	Dr. Raics Péter Pál.....
	Prof. Dr. Palla László

A doktori szigorlat időpontja: 2017. június 22.

Az értekezés bírálói:

.....
.....

A bírálóbizottság:

elnök:
tagok:

Az értekezés védésének időpontja:

Contents

1	Introduction	1
1.1	The CMS Experiment	2
1.2	Supersymmetry Searches in the LHC	3
1.3	Razor variables	5
1.4	Boosted object tagging	7
2	The pixel detector of CMS	9
2.1	Hit efficiency measurement	10
2.1.1	Definition	11
2.2	Detector calibrations	14
2.2.1	Time alignment	14
2.2.2	High voltage bias scans	16
2.3	Results with the pixel detector in LHC Run 1 and 2	19
2.4	Results with the phase 1 upgrade pixel detector in LHC Run 2	22
3	Supersymmetry search with the Razor variables in boosted final states	27
3.1	The Signal	27
3.2	Search strategy	28
3.3	Datasets and Simulation Samples	30
3.4	Event reconstruction and object definitions	32
3.4.1	Primary vertex	32
3.4.2	Leptons	35
3.4.3	Photons	40
3.4.4	Jets and higher order objects, variables	40

3.5	Event selection	48
3.5.1	Baseline selection	48
3.5.2	Trigger	49
3.5.3	Signal selection	51
3.6	Background estimation	58
3.6.1	Extrapolation of events from loosened signal regions	60
3.6.2	$t\bar{t}$ and single top	61
3.6.3	$W(\rightarrow l\nu)+jets$	65
3.6.4	Multijet	67
3.6.5	$Z(\nu\nu)+jets$	70
3.6.6	Validation of the background estimation	81
3.7	Systematic Uncertainties and Corrections	83
3.7.1	Theory uncertainties	83
3.7.2	Jet/MET uncertainties	84
3.7.3	$b/W/top$ tagging	85
3.7.4	Lepton related uncertainties	87
3.7.5	Other uncertainties	88
3.7.6	Summary of uncertainties	90
3.8	Results and Interpretation	90
	Acknowledgements	98
	Summary	99
	Összefoglaló	103
	Bibliography	107
	Appendices	121
A	Boosted object tagging scale factors	121
B	Additional tables and figures	122

Chapter 1

Introduction

The Standard Model (SM) of particle physics had an extraordinary success in predicting a wide array of new fundamental particles. This includes the charm, bottom and top quarks, and leptons from the third family: the tau lepton and its neutrino; all of which are fermions. The model, which incorporated quantum chromodynamics (QCD), could explain the strong interaction through the exchange of a gluon, which is the mediator of the strong nuclear force. It also successfully predicted the existence of massive W and Z bosons responsible for the weak interaction and the Higgs boson, the particle that gives mass to other particles through the Higgs mechanism, which was discovered in 2012 by both the ATLAS and the CMS experiments. Despite all of its remarkable successes the model still cannot describe, among many others, the matter-antimatter asymmetry, the nature of dark matter, neutrino oscillations or give an explanation why the gravitational force is so much weaker than the others. These point to the need of theories Beyond the Standard Model (BSM) which can explain these issues. One of the widely popular extensions of the Standard Model is Supersymmetry (SUSY) [1, 2, 3, 4, 5, 6], which introduces a new space-time symmetry, known as the R-symmetry, that allows the existence of new particles, which are the so-called “superpartners” of their SM counterparts. The ordinary quantum numbers

of the new particles are the same as those of their SM counterparts except their spin which differ by a half-integer. However, the new R-symmetry needs to be spontaneously broken allowing the superpartners to differ in mass, otherwise the new particles must have been found already by now. Supersymmetric could explain many shortcomings of the Standard Model, for e.g./ why the observed Higgs boson is so light and give a new candidate for dark matter in the form of the neutralino, which is often believed to be the lightest superpartner (LSP). It could also provide a potential new way to unify all fundamental forces at very high energy scales. These compelling properties of Supersymmetry gave motivation to search for evidence of the predicted new particles.

1.1 The CMS Experiment

The Compact Muon Solenoid (CMS) Experiment [7] is one of the four major experiments of the Large Hadron Collider (LHC). The detector is located about 100 meters underground between the Jura Mountains and Lake Geneva, near Cessy, France. The prime motivation of the experiment is to study proton-proton and heavy ion collisions at 13 TeV and 2.75 TeV per nucleon center-of-mass energy respectively. The main areas of research includes the search for the Higgs boson, which was successfully discovered in 2012 [8, 9], supersymmetry and the search for extra dimensions. The experimental apparatus, which is illustrated on Figure 1.1, consists of an all-silicon pixel and strip tracker, a homogeneous lead-tungstate scintillator-crystals-based electromagnetic calorimeter (ECAL) surrounded by a brass/scintillator sampling hadron calorimeter (HCAL), a superconducting solenoid producing 3.8 T magnetic field, and a four station muon

detector system integrated with the iron return yoke of the magnet. The LHC beams, which were colliding in the center of the CMS detector, contained up to 2208 bunches each. The time spacing between bunch crossings were as low as 25ns. The detector is an excellent experimental tool which is used to test our understanding of the fundamental nature of our universe. As part of my PhD studies I began working in the CMS Experiment in 2010. The first part of my studies involved the calibration, operation and offline software reconstruction of the pixel detector. These studies will be discussed in Chapter 2.

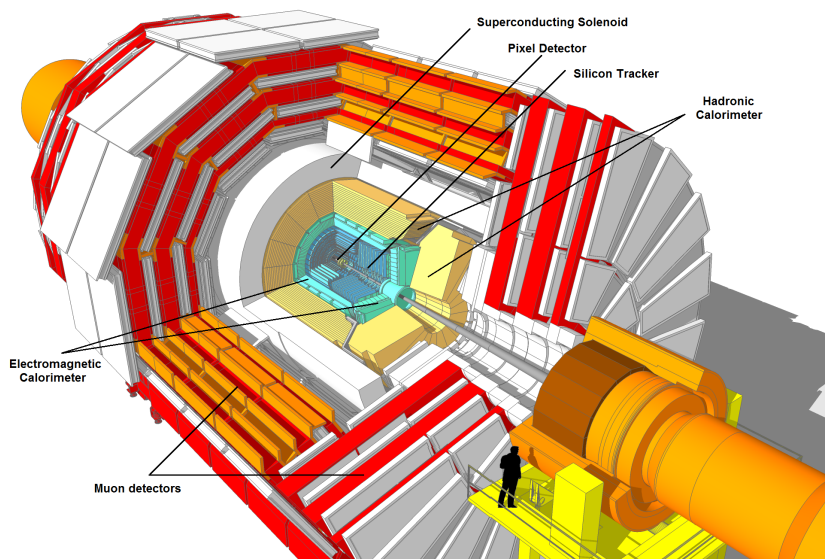


Figure 1.1: Schematic view of the CMS detector. Picture was taken from [30] with subdetector markers added by hand.

1.2 Supersymmetry Searches in the LHC

The second part of my studies involved the search for new particles predicted by the supersymmetric extension of the Standard Model. Up until now no

evidence of new particles beyond the Standard Model were found in the LHC. In their most cited papers, the two largest LHC experiments, CMS and ATLAS, both gave exclusions of supersymmetric particle masses beyond the TeV scale [10, 18, 19, 20, 21, 22][23, 24, 25, 26]. These searches typically looked for large jet multiplicity, b-tagged jets and significant amount of missing transverse energy. Based on the signature, the analyses usually selected or vetoed leptons, and used additional discriminators like H_T , which is the scalar sum of jet transverse momenta, or other more complicated ones e.g. α_T [19] or M_{T2} [22].

Most of these LHC searches use so-called simplified models [27, 28, 29] which consider only a few particles to be light. These models are described by effective Lagrangians with a small number of free parameters. These are usually the masses of particles, branching fractions and production cross-sections. This framework can be used to construct analyses that are sensitive to a wide range or more specific SUSY signatures.

In 2012 I participated in one of the Run 1 SUSY searches [10]. In this study I contributed to the determination of systematic uncertainties related to the single lepton identification, reconstruction and so-called “trigger” efficiencies. Triggers are fast response logical units which decide if a particular collision event will be recorded. They are used in order to thin down the otherwise huge data output of the LHC to include only the events which are interesting to the analyzers. Run 1 data allowed us to exclude the existence of gluinos above 1.1 TeV in some scenarios. In Run 2, the almost doubled collision energy and the increased luminosity motivated me to pursue the search further with a more specialized approach. The models of our interest were the ones where a pair of heavy gluinos or stops are produced each of which decay to various standard model particles and the weakly interacting

LSP. The latter are undetected and cause a large fraction of the momentum to be missing. More details about the models are given in Section 3.1. In these simplified models, the parameters of interest reduce down to the masses of the mother particles (gluinos or stops) and the neutralino. The branching fraction of the main particle decay is usually assumed to be 100%, although one can examine any lower branching fractions to set exclusion limits. In Chapter 3, I describe the main part of my PhD studies which was to conduct a search targeting specific SUSY models with a top quark in the final state.

Above the TeV scale, the top has a large chance to be boosted due to the decay of their heavy supersymmetric mothers. In our search, we chose to increase the sensitivity to such signals by incorporating boosted object tagging techniques. In order to further increase the sensitivity of this search we combined our results with a similar but more inclusive Razor analysis which vetoed our boosted object selection. All the work described in Chapter 2 and 3 are my own, except for the final combination results (the exclusion limits) which includes the work of another analysis group within CMS. Additionally, citations are given to all the methods and calculations that were derived by others, usually within our collaboration.

1.3 Razor variables

The razor variables [11, 12, 13], M_R and R^2 , have proven to be very sensitive discriminators in many analyses for signals with pair produced heavy objects which decay to hadrons and invisible particles. They estimate the mass scale of the of the new particles as a peak. Some information is lost due to the undetected particles, therefore the calculation of the variables

deal with a few key assumptions. Since the unknown mother particles are expected to be very heavy, it is assumed that the center-of-mass frame in which they are produced is approximately equivalent with their rest frames. The second assumption is that the transverse boost required to transform the four-momenta of the final state particles from the lab frame is negligible. With these approximations, the rough approximation-frame (R-frame) is found in which the magnitudes of the momenta of the visible decay products of the heavy SUSY particle pair are equal. The longitudinal boost invariant R-frame mass, M_R , is defined in Section 3.4.4, is proven to be a good estimator of $M_\Delta = \frac{M_G^2 - M_\chi^2}{M_G}$, where M_G and M_χ denote the mass of a hypothetical heavy mother particle and its weakly interacting (undetected) decay product. Standard Model background processes typically produce a nearly exponentially falling distribution, peaked near zero, while signals produce a peak typically at higher values for large mass differences between M_G and M_χ . However, alone M_R would lose its discriminating power for small mass differences, therefore another estimator, M_T^R is derived which estimates the same mass scale but using the information available in the transverse direction (in the plane perpendicular to the beam). This includes the measured momentum imbalance that can arise due to the presence of the undetected invisible particles which carry away a fraction of the momentum. The dimensionless ratio ($R \equiv \frac{M_T^R}{M_R}$) between these two estimators is the other razor variable, which peaks typically around 0.5 for signals and falls rapidly from a peak at zero for standard model backgrounds. The events in the signal region of this analysis are split into bins of M_R and R^2 . The advantage of this choice is that the discriminating power of the M_R variable increases as we test higher and higher gluino masses so it is easier to find a possible signal despite the much lower cross section.

1.4 Boosted object tagging

The masses of gluinos and stops are excluded to higher values each year since 2010 which means that a possible SUSY signature, if exists, will more likely contain boosted objects. An abundance of research papers were published in recent years targeting to provide tools to identify these objects. This analysis mainly focused on the hadronic decay of boosted *tops* and *Ws* both of which could be tagged in wide cone jets [17]. One of the difficulties with such approach was the presence of so-called “pile-up” events which did not originate from the main collision event but from other inelastic proton-proton collisions in the same bunch crossing. These pile-up events produced particles that overlapped with the jet of the main collision event, therefore one needed to identify and remove such particles if possible. One of such earlier procedures looked for tracks originating from other primary vertices, but such methods could only remove charged hadrons from the jet. Instead, the Pile-Up Per Particle Identification (PUPPI) [16] algorithm was used which was developed to give a weight to the four-momentum for all jet constituents, including neutral hadrons, based on the likelihood that they originate from pile-up events. The reweighted jet constituents yielded a boosted object mass that was more stable with respect to the number of reconstructed vertices than the one obtained with the charged hadron subtraction (CHS) technique. The tagging of the jets was done with substructure techniques. One of them was the so-called soft drop declustering algorithm [14] (Soft-Drop) which was used to remove soft wide-angle radiation from the jet in order to reduce contamination from initial state radiation or other particles which did not originate from the primary hard scattering. The mass of the remaining groomed jet was used as a powerful discriminator against light

quark and gluon jets emerging from QCD processes. The final substructure technique we used for top/W tagging was N-subjettiness [15] which gave information about the number of subjets resulting from the decay of the mother particle. In our case, the hadronically decaying boosted W s formed two subjets, while the boosted $tops$ had a third additional subjet originating from the b -quark (the subjet is referred to as b -tagged). The b -tagging of the (sub-)jets, for which the pixel detector played a crucial role, is explained in Section 3.4.4.

Chapter 2

The pixel detector of CMS

The pixel detector is the innermost part of the CMS tracking system which plays a crucial role in the detection of charge particle tracks originating from the interaction point. The detector, which was commissioned in 2008 and was in operation until 2016, had three barrel layers and two endcap disks on both sides. The detector went through the Phase-1 Upgrade and continued its operation in 2017. The upgrade detector had four barrel layers and three endcap disks. Figure 2.1 shows the comparison of both detectors. The number of pixels was originally 66 million then almost doubled to 124 million. The pixels have a size of $100\ \mu\text{m} \times 150\ \mu\text{m}$. This subdetector provides high resolution position measurements for leptons and charged hadrons with excellent efficiency. Each charged particle traversing through the pixel sensors deposits charges on multiple pixels. If the charges reach a certain minimum threshold, which is used to remove noise, the charge values are read out from each pixel. The analogue readings are converted to digital optical signals in order to avoid the interference of the magnetic field. These signals are then processed further away from the detector where the digital signals are decoded. During reconstruction single or multiple adjacent pixels are combined into clusters from which the expected particle positions, called hits, are determined. These, together with hits in the silicon strip detector

system, are used to reconstruct the tracks and the interaction points (vertices). The high precision of these measurements allows the reconstruction of additional displaced vertices that are used for the tagging of jets originating from bottom quark decay. Due to these important roles in physics, the careful operation and maintenance of this detector was very important for the success of the experiment.

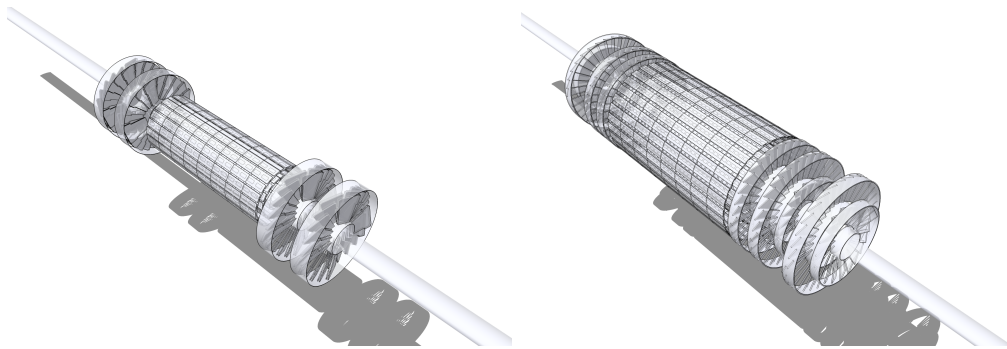


Figure 2.1: Schematic view of the pixel detector until 2016 (left) and the Phase-1 Upgrade detector (right). Plot is taken from [30].

2.1 Hit efficiency measurement

One of the important detector performance indicators is the hit finding efficiency. It was important to periodically monitor this quantity, which indicated the quality of detector calibrations, which include among others the time alignment, high voltage bias setting and threshold calibration. It also gives feedback about possible inefficiencies or failures of detector components.

2.1.1 Definition

For the measurement of the hit efficiency, we rely on the tracking algorithm, which uses a combination of pixel hits, so-called “seeds”, to establish a starting point for a track to which additional compatible hits in the silicon tracker can be attached. In the main algorithms, helical trajectories are fitted to pixel doublets or triplets (or triplets and quadruplets in case of the Phase-1 Upgrade detector which has an additional layer/disk). The algorithm uses this trajectory as a starting point and goes through all detector layers, starting from the innermost one, that are crossed in its path to determine if a compatible cluster is found within a certain distance. If such a hit is found it is known as a “valid” hit, otherwise the hit is “missing”. The algorithm allows only one hit to be missing and terminates if a 2nd one is found. The definition of hit efficiency on a measured module is the probability to find a valid hit by the tracking algorithm or otherwise there is a cluster within $500 \mu\text{m}$ distance from the expected particle positions determined by the crossing trajectory within the sensor plane [31]. This search window was increased to 1mm for the Phase-1 Upgrade detector. For the measurement we selected tracks coming from the primary vertex with $p_T \geq 1.0 \text{ GeV}$ and at least 11 hits in the strip detector system. We also required these tracks to be isolated, requiring no other hits within a distance of 5 mm on the same module. Additionally, it was required that the two closest layers or disks to the one being measured had valid hits on them, i.e. the track position was confirmed already by existing clusters. Figure 2.2 illustrate the cross-sectional view of the Phase-1 Upgrade detector. We required the tracks to satisfy the following very tight region-dependent impact parameter (distance to the primary vertex) cuts:

- Layer 1: $|d_0| < 0.1 \text{ mm}$, $|d_z| < 1.0 \text{ mm}$;
- Layer 2-3(4): $|d_0| < 0.2 \text{ mm}$, $|d_z| < 1.0 \text{ mm}$;
- Endcap: $|d_0| < 0.5 \text{ mm}$, $|d_z| < 5.0 \text{ mm}$;

where d_z and d_0 is the track-to-vertex distance along the beam and in the plane orthogonal to the beam, respectively.

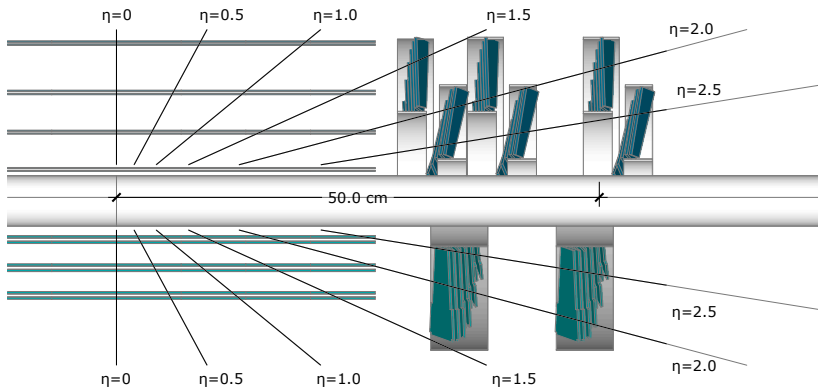


Figure 2.2: The schematic view of the Phase-1 Upgrade pixel detector in the plane defined by the beam axis and the radial direction. The straight lines illustrate the pseudorapidity coverage of tracks for the barrel layers and endcap disks. The plot is taken from [32].

This selection greatly reduced the number of tracks from secondary interactions and improved their purity by eliminating a large fraction of the fake ones. The probability to find a hit in regions where modules overlap within the same layer or disk is larger than elsewhere. In order to eliminate this upward bias, these regions were excluded from the measurement. Additionally, a fiducial region was defined for each module excluding module and readout chip edges to allow for residual misalignment. Permanently or intermittently bad modules were also excluded. The latter includes those for which errors were signaled by the front-end driver, and Single Event Upsets

(SEUs). An SEU occurs when an ionizing particle traversing through the detector changes the state of a control register causing a temporary failure of the affected detector part [33]. The systematic uncertainty of the measurement is estimated to be 0.2–0.3 %. Figure 2.3 shows the measured hit efficiency in 2011.

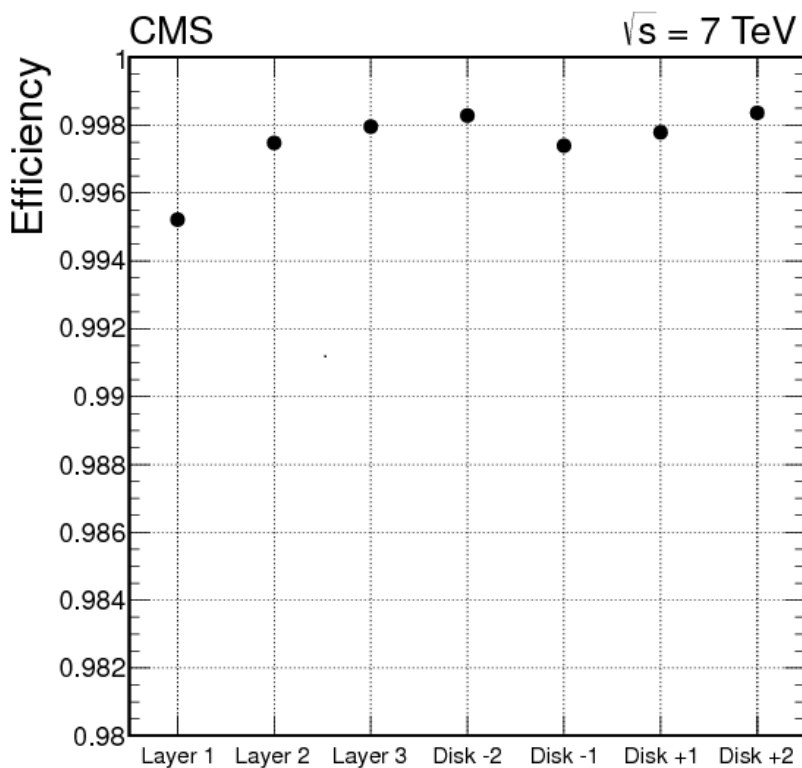


Figure 2.3: The average hit efficiency of the pixel detector barrel layers and endcap disks in 2011.

2.2 Detector calibrations

The continuous irradiation of the detector causes a change in the cluster properties. It requires constant monitoring and calibration efforts in order to mitigate possible efficiency and resolution losses. Figure 2.4 shows the change of the cluster size and charge as a function of the total integrated luminosity between 2011 and 2016. The plot provides feedback to the operation team, who used it to determine when a pixel threshold adjustment is needed, and the offline reconstruction group who uses it to schedule corrections to the parameters of the analogue-to-digital pixel charge conversion, which is called gain calibration. The plot also indicates that the radiation effect cannot be mitigated indefinitely. At least the innermost layer (layer one) needs periodic replacements. One such occasion was the Phase-1 Upgrade of the detector in 2017 which replaced the entire detector.

2.2.1 Time alignment

In the beginning of the data taking period of each year, the time alignment of the detector was checked by performing so-called delay scans in which the common global delay of the detector is tuned w.r.t the phase of the LHC bunch-crossing clock [33]. A working point was established by choosing a setting at which the hit efficiency reaches a point on the plateau and the cluster size is nearly at the maximum point. Figure 2.5 shows the results of the 2011 timing scan in LHC Run 1 and Figure 2.6 the results of the first scan in 2015 in the beginning of LHC Run 2. Every year this common setting and also the internal time alignment of each readout group, which are the lowest fraction of the detector in which the timing can be adjusted, was validated, and if needed, synchronized. The latter synchronization only

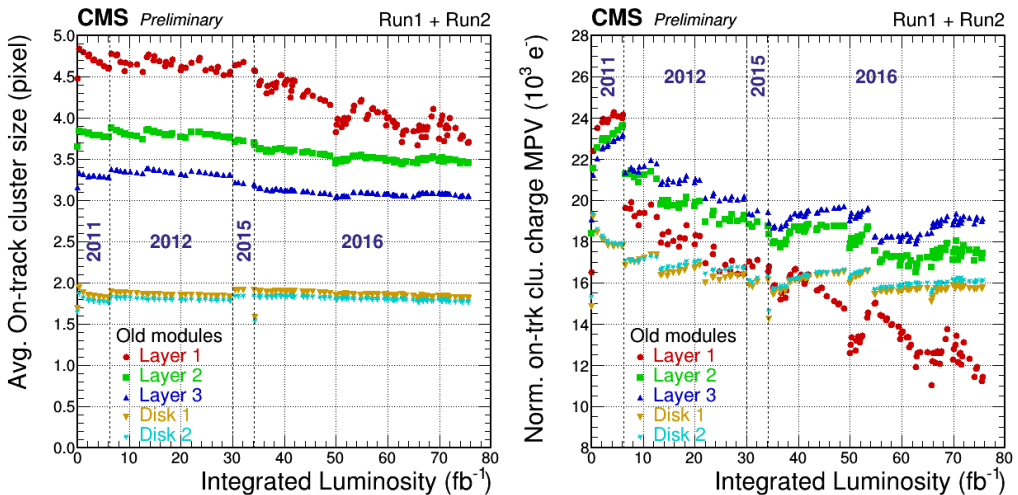


Figure 2.4: The average on-track cluster size (left) and the most probable value of the normalized cluster charge (right) vs. total integrated luminosity between 2011 and 2016. Some broken modules were replaced during the Long Shutdown 1 between 2013 and 2014, these plots only shows those which were not. Threshold and gain calibrations cause discontinuities in the cluster size and charge respectively.

needed to be done once for each LHC run. The spread of the most optimal timing settings within a readout group was also measured to be around 2-3 ns. This could not be tuned further by the design of the detector. In all cases a safe common setting was chosen that would be near the end of the hit efficiency plateau, usually around 2ns delay below the setting which provided maximum cluster size. This setting was seen to be appropriate throughout the entire run period.

The time alignment of the detector in 2017 was much more challenging. It was discovered too late that the PROC600 chip [35] which was used in the innermost barrel layer had a constant timing offset compared to what the chips used in the same readout group in layer two. The difference was approximately 12 ns which is nearly half of the time between each bunch-crossings. In order to cope with this constraint a setting was carefully chosen

which is nearly fully efficient for both layer one and two. The decision was to use a setting which provides the maximum cluster size and consequently the best possible position resolution for layer one, which is the most important layer for physics, while allowing a slightly less optimal setting for layer two. The latter layer was further optimized with various other calibrations and voltage setting. The results of the last timing setting is shown in Figure 2.7 [36].

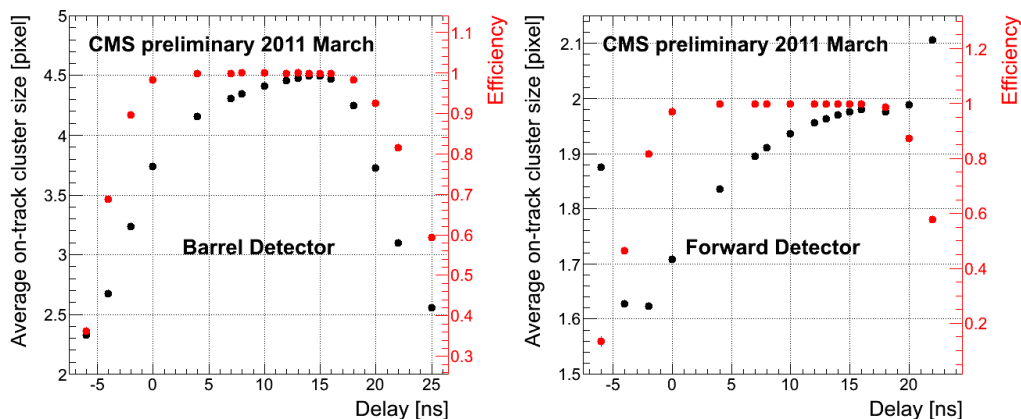


Figure 2.5: The average on-track cluster size (black) and the hit efficiency (red) vs. various time delay settings for the barrel (left plot) and the endcap (right plot) in 2011. The chosen operation point was at 13 ns which provided maximum hit efficiency and nearly maximum cluster size.

2.2.2 High voltage bias scans

Another important scan which is performed throughout the lifetime of each pixel detector is the high voltage bias scan [37, 38, 39, 40, 41]. The voltage setting of the detector is chosen such that the hit efficiency is at maximum and the cluster size is adjusted to provide the best overall hit position resolution for the period in which the setting is used. The bias voltage cannot

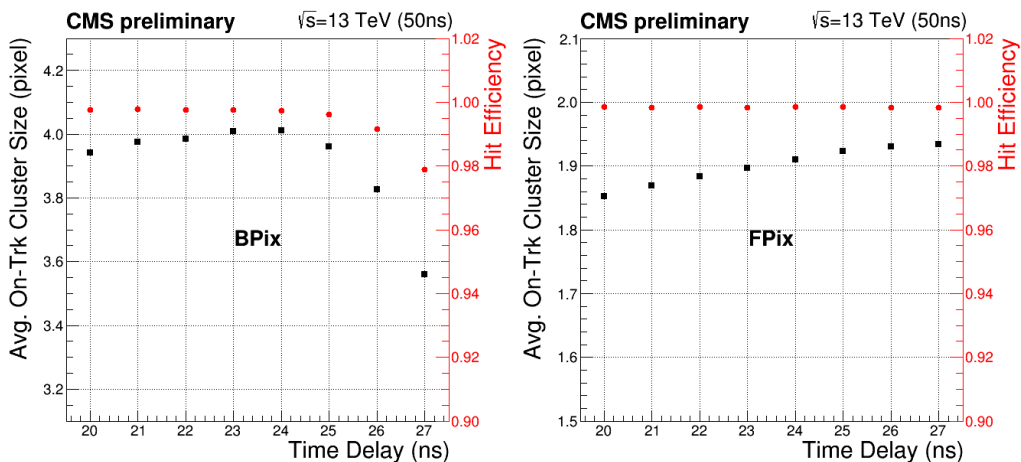


Figure 2.6: The average on-track cluster size (black) and the hit efficiency (red) vs. various time delay settings for the barrel (left plot) and the endcap (right plot) in 2015. The chosen operation point was at 22 ns.

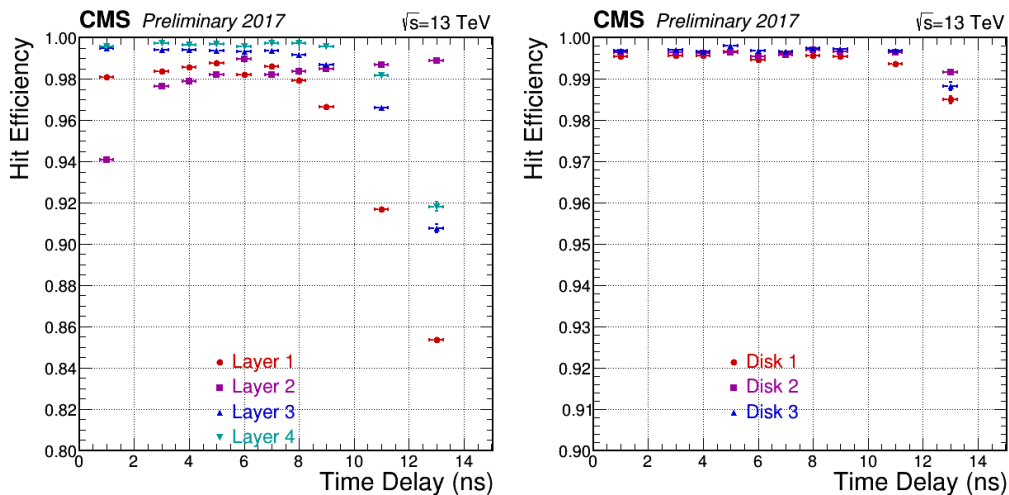


Figure 2.7: The hit efficiency vs. various time delay settings for the barrel (left plot) and the endcap (right plot) in 2017. The chosen operation point was at 6 ns which provided a nearly maximum efficiency working point for all layers and disks.

be too high, because it would reduce the Lorentz drift of the charge carriers inside the sensor due to the increased electric field. This would cause the cluster size in the direction perpendicular to both the magnetic field and the electric field to shrink and would consequently reduce the precision in which the hit position can be determined during the reconstruction. For this reason, periodic scans were taken to measure both the hit efficiency and cluster properties like size and charge for various bias settings. The results of the Run 1 scans for the innermost, highest irradiated layer is shown in Figure 2.8. Similar results for the endcap disk 1 is shown in Figure 2.8.

Due to the continuous drift of the average cluster charge (as seen on Figure 2.4) and the non-flat plateau observed on the charge vs bias voltage curves (right plot on Figure 2.8), the charge collection efficiency was not well defined. Instead of that, we used the hit efficiency to monitor the evolution of the radiation damage of the detector. The hit efficiency curves on Figure 2.8 (left plot) were fitted with sigmoid functions. The voltage at which the efficiency is 1% below the maximum was extracted and is shown in Figure 2.10. All layers were seen to be type-inverted [43] within around the first 20 fb^{-1} in Run 1, which means that the effective doping of the initially n-type sensor changed to p-type. In other words, the electric field flipped sign due to the irradiation induced positive charge holes. This is visible from the initially decreasing trend in the voltage corresponding to the beginning of the efficiency plateau in Figure 2.10. In order to mitigate the effects of charge trapping, the high voltage bias applied on layer one was increased from 150V to 200V for Run 2, the rest of the layers remained at 150V and the endcap at 300V until the replacement of the detector. Some of the endcap modules had worse voltage vs. current characteristics in the initial module grading process. Due to this a larger operational voltage was

chosen from the start which proved to mitigate inefficiencies arising on the module edge pixels without compromising much the hit position resolution.

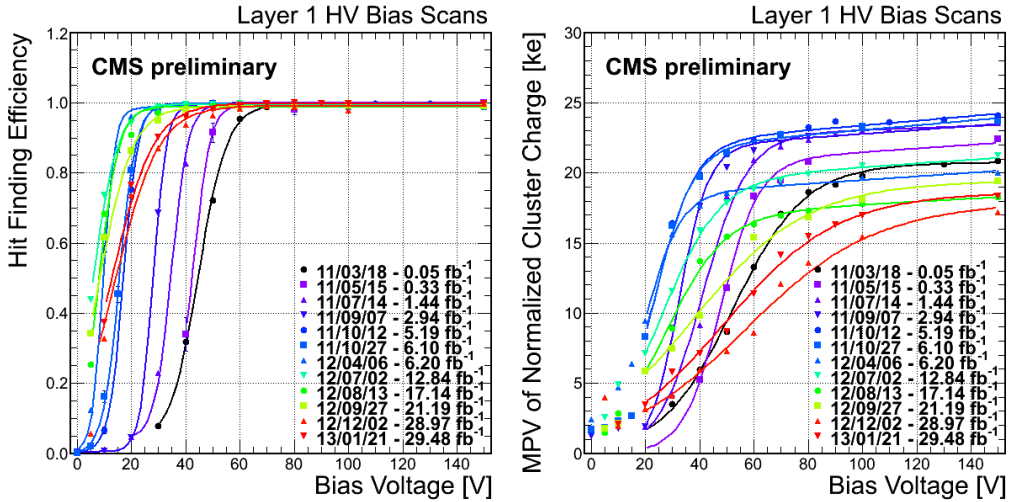


Figure 2.8: The hit efficiency (left) and the most probable value of the normalized on-track cluster charge (right) vs. various high voltage bias settings for the innermost layer in LHC Run 1. The chosen operation point in Run 1 was 150V for the barrel.

2.3 Results with the pixel detector in LHC Run 1 and 2

While the efficiency of the pixel detector remained very high at low detector occupancies, a large inefficiency was observed at high luminosities [33, 37, 38, 39, 40, 41, 42]. Figure 2.11 shows the efficiency in LHC Run1. The source of the inefficiency is due to the limited size of the buffers for each double column in the readout chips. At high luminosities, the chance to fill the same buffer within a short period of time increases, and this causes data losses. At low pseudorapidities, where the charged particles cross the

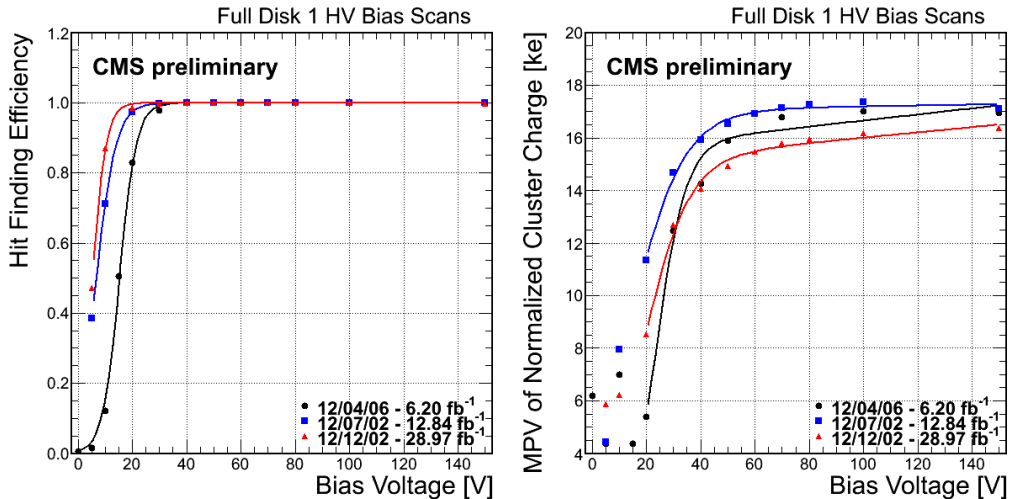


Figure 2.9: The hit efficiency (left) and the most probable value of the normalized on-track cluster charge (right) vs. various high voltage bias settings for the first endcap disk in LHC Run 1. The chosen operation point in Run 1 was 300V for the forward disks.

sensor in large angles, the cluster size is usually small and the chance to lose the entire cluster due to data loss in a double column is larger. At shallow angles, the clusters are larger; although, the probability to lose them is small, truncation or cluster splitting may greatly reduce the hit resolution and increase the position bias. For this reason, the buffers of the phase 1 upgrade detector was increased, and the readout mechanism improved in order to mitigate these effects [44]. During the first long shutdown (LS1) of the LHC, we developed a simulation of the double column inefficiencies [45] in order to improve the agreement between the MC simulation and the collision data. Such improvement of the simulation leads to a better description of the tracking efficiency and the hit resolution, and therefore also a better agreement of flavor tagging efficiency and fake rate between data and simulation in the physics analyses. In the second LHC run, starting in 2015, several changes contributed to the increase of the particle fluence: the center-

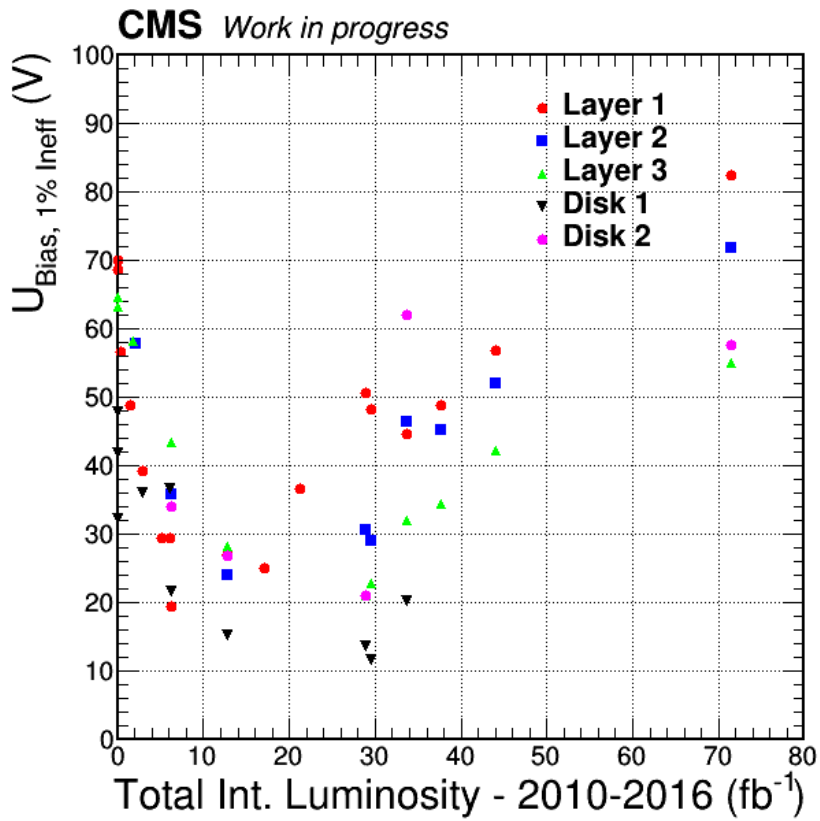


Figure 2.10: The bias voltage at which the inefficiency is 1% vs. the total integrated luminosity for all pixel detector layers and disks.

of-mass energy increased from 8 TeV to 13 TeV which increased the average number of charge particles emitted in each inelastic proton-proton collision. The average number of simultaneous collisions, known as pile-up, also increased, but the major change came from the operation mode change of the LHC. The time spacing between each colliding bunches decreased from 50ns to 25ns in 2015 allowing a larger number of colliding bunches to be filled in the LHC ring. Figure 2.12 shows the efficiency in 2015 for different filling schemes [46, 47]. These factors all contributed to the increase of data loss in the detector. The maximum instantaneous luminosity in 2016, which roughly doubled compared to 2012, reached values above $1.4 \times 10^{34} \text{ cm}^{-2} \text{ s}^{-1}$. This was well above the value the detector was designed to operate in. The inefficiency at high instantaneous luminosities (see Figure 2.13) reached 6% on layer one [48, 49, 50], which signaled the need to replace the detector within the phase 1 upgrade project. These measurements served as an input to readjust the inefficiency parameters of the simulation each year, and provided useful information for the finalization of the layer one readout chip design for the Phase-1 Upgrade detector [44, 51].

2.4 Results with the phase 1 upgrade pixel detector in LHC Run 2

The upgrade of the pixel detector was successfully completed in the extended year end technical stop between 2016 and 2017. The improved design allowed the detector to collect data with high efficiency even at particle rates surpassing the previous years. Figure 2.14 shows the measured efficiency with the new detector confirming the improvement [36].

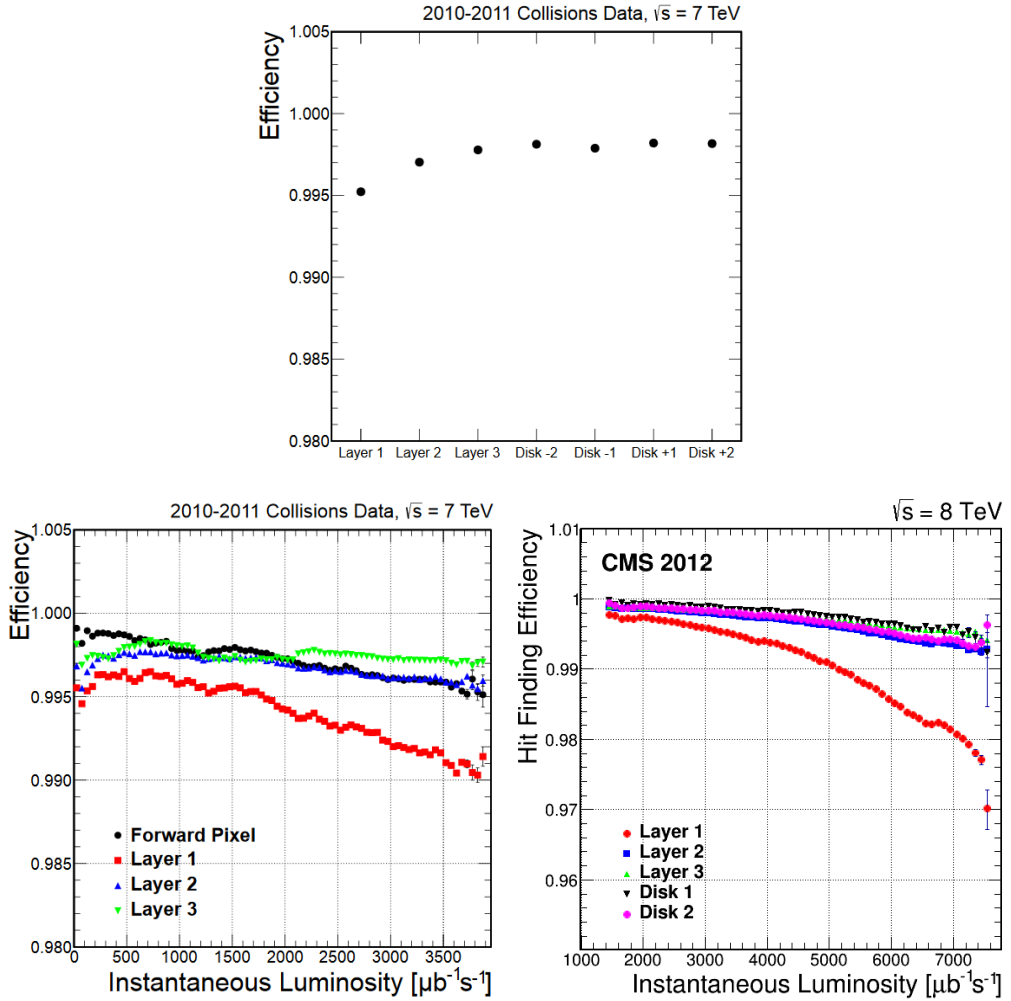


Figure 2.11: The average hit efficiency in 2010 and 2011 (top) and vs. instantaneous luminosity in 2010 and 2011 (bottom left) and 2012 (bottom right) for all layers and disks.

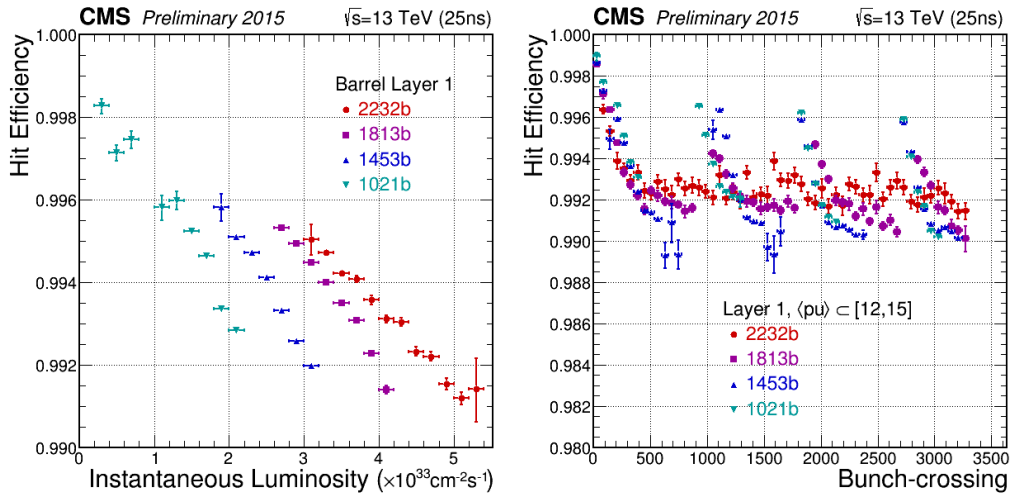


Figure 2.12: The hit efficiency of layer one vs. instantaneous luminosity (left) and vs. the bunch crossing number around the LHC orbit (right) for various number of colliding bunches in 2015. The average number of pile-up on the right plot was between 12 and 15 in order to select events with similar occupancy. There is a so-called abort gap between 3300 and 3600 during which the internal buffers of the readout chip has time to clear, therefore the efficiency reaches 100% in the first colliding bunch. Data overflow causes a rapid efficiency drop in the consecutive bunches until an equilibrium is reached between the filling and emptying of buffers. There are larger gaps between bunch trains for lower number of colliding bunch schemes which also allows a partial recovery of efficiency.

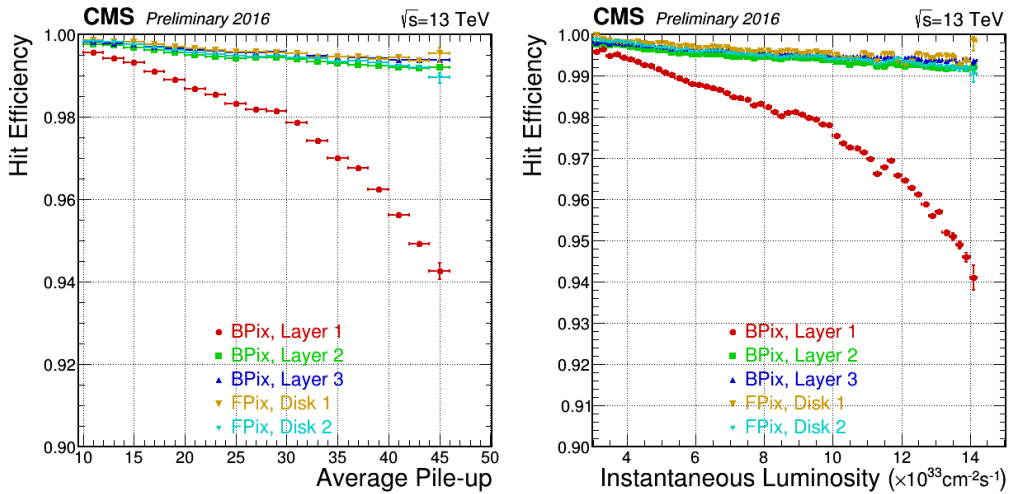


Figure 2.13: The hit efficiency vs. pile-up (left) and vs. instantaneous luminosity (right) in 2016 for all layers and disks.

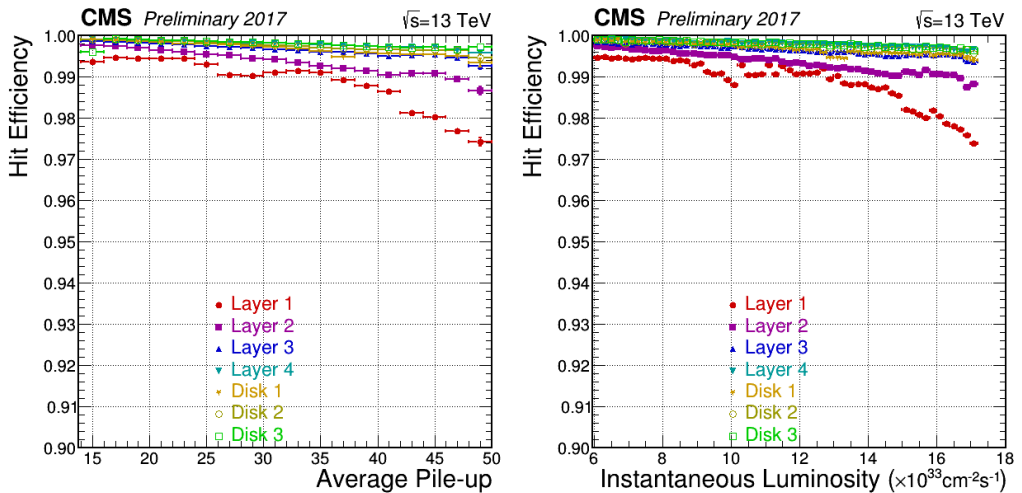


Figure 2.14: The hit efficiency vs. pile-up (left) and vs. instantaneous luminosity (right) for all layers and disks of the phase 1 upgrade pixel detector.

Chapter 3

Supersymmetry search with the Razor variables in boosted final states

3.1 The Signal

The simplified SUSY models of our interest had gluino or *top* squark (or simply *stops* denoted by \tilde{t}_1) pairs decaying to *top* quarks. The event selection required that the *tops* decay hadronically and at least one of them was boosted enough that either the *W* or also the *b*-quark was within a single wide cone jet. The models also contained the lightest neutralinos, denoted by $t\tilde{\chi}_1^0$.

In the *T1tttt* models, the gluinos decay directly to $t\bar{t}\tilde{\chi}_1^0$. In the *T5ttcc* model each gluino decay to a $t\tilde{t}_1$ where the *top* squark subsequently decays to a $c\tilde{\chi}_1^0$. The direct production of *top* squarks (*T2tt*) were also considered, where each *stop* decays a $t\tilde{\chi}_1^0$. These models are shown in Figure 3.1.

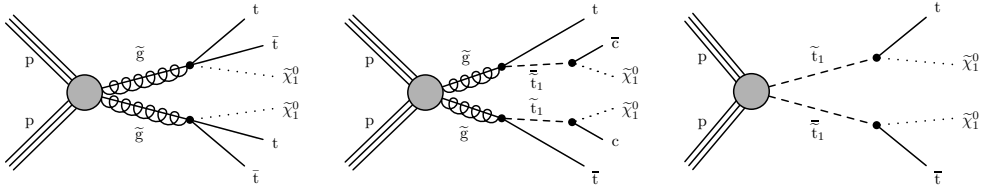


Figure 3.1: The models considered in this analysis: (left) T1tttt: pair-produced gluinos, each decaying to a $t\bar{t}$ and the LSP; (middle) T5ttcc: pair-produced gluinos, each decaying to top and a low mass $stop$ the latter which decays to a charm quark and the LSP; (right) T2tt pair-produced top squarks each decaying to a top and the LSP.

3.2 Search strategy

The gluinos of interest had a large mass, typically in the range of 1.0 TeV to 2.0 TeV while the top squarks had a mass around half of that. The top quarks leaving the gluino decay had a large probability to gain a Lorentz boost. This is shown in Figure 3.2, in which the generator level W and top p_T distributions are compared for the standard model $t\bar{t}$ and signals with varying gluino mass in a loose preselection region.

The decay products of boosted objects are typically merged within a single cone with a distance parameter of $\Delta R \sim 2m/p_T$, where m is the mass of the originally decaying particle. This analysis used wide cone jets with $R = 0.8$. Using this formula, the hadronically decaying W and tops are very likely merged within this cone size if their p_t is larger than 200 GeV and 430 GeV, respectively. This search is looking for an excess of events on top of the standard model background predictions in bins of M_R and R^2 in fully hadronic final states. The data driven background estimation is done by defining and counting events in control regions sufficiently enriched by the most significant irreducible background processes, and using MC signal-to-control region transfer factors to derive predictions in the signal region.

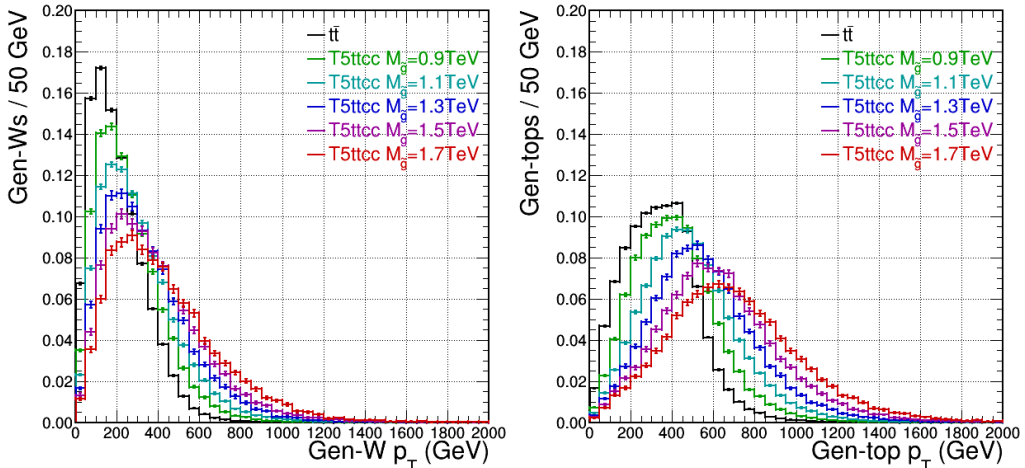


Figure 3.2: The p_T distribution of generator Ws (left) and tops (right) for several gluino mass points of the T5ttcc model and Standard Model $t\bar{t}$ events. Events were skimmed with a loose requirement of an AK8 jet with $p_T > 200$ GeV and $R^2 > 0.04$.

Additionally, the signal depleted control regions serve as a tool to validate the modelling of each major background. Finally, so-called “closure tests” are done to check the validity of the method in two separate validation regions which are similar to the signal region.

The analysis [105] presented in this thesis is looking for at least one highly boosted hadronically decaying W boson and b quark jet in one of the search regions or a boosted top in the other. The boosted object tagging techniques were introduced in Section 1.4. In order to discriminate signal events from background the events were counted in bins of the razor variables explained in Section 1.3. The steps of the analysis is described in detail in this chapter. First, the datasets and simulation samples are specified in Section 3.3, the object selection in Section 3.4 and the event selection in Section 3.5 which includes the trigger choice, the baseline and signal region definitions. The background estimation methods and the estimation

of systematic uncertainties are described in Section 3.6 and 3.7. Finally, the results and its interpretation is given in Section 3.8.

3.3 Datasets and Simulation Samples

The data for this analysis consist of 35.867 fb^{-1} data collected by the CMS detector in 2016 at a center-of-mass energy of 13 TeV. The data was recorded with so-called triggers which are systems which decide in a very short time during collisions if a specific event that took place at the LHC is worthy for recording for physics studies. The main trigger used for this study, specified in Section 3.5.2, was selecting events either with a H_T requirement, which is the scalar sum of all jet transverse momenta in the event, or wide cone jets which pass a certain p_T threshold. Additionally, for trigger efficiency measurements, single lepton (electron or muon), single photon or MET (missing transverse energy) triggers were used.

We also used Monte Carlo simulation samples for the Standard Model background and the SUSY signal processes which were generated centrally by the CMS collaboration. From here on it is referred to them as MC. The QCD multi-jet sample (or in short “QCD”), which includes the production of multiple jets originating from the five lightest quarks and gluons, as well as the $W/Z/\text{Drell-Yan}/\gamma$ +jets and the SUSY signals were generated in Leading Order (LO) accuracy with MADGRAPH v5 [53] and interfaced with PYTHIA 8.212 [54] for showering, fragmentation and hadronization. The matrix elements were matched to the parton showers using the MLM prescription [55, 56]. Additional Next-to-Leading Order (NLO) samples were generated with MADGRAPH5_aMC@NLO v2.2.2 [57], including $W(l\nu)$ +jets, s-channel single top, $t\bar{t} + W/Z/\gamma/t\bar{t}$, the triboson (WWW,

WWZ, WZZ and ZZZ) and some of the diboson samples (WZ, $ZZ(2q2\nu)$ and $ZZ(2q2l)$). The bracket behind a mother particle denotes its considered decay channel, and l means charged leptons. The matching between matrix elements and parton shower simulations were done with the FxFx merging algorithm [58]. The remaining samples were generated with POWHEG BOX v2 [61, 62, 63] in case of the $t\bar{t}$ [64], the t and Wt channel single top [65, 66] and the other part of diboson samples [67, 68] (WW, $ZZ(2l2\nu)$ and $ZZ(4l)$). Similar to the LO MCs, the NLO ones were interfaced with PYTHIA 8.212 [54] too. MADSPIN [59, 60] was used for the aMC@NLO diboson, single top t channel, $t\bar{t}W$ and $t\bar{t}\gamma$ samples.

The CUETP8M1 [69] event generator tune was used for the majority of simulation samples except for the $t\bar{t}$, single top s channel and the $t\bar{t}t\bar{t}$ backgrounds for which the CUETP8M2T4 [70] tune was used, which was specifically derived for $t\bar{t}$ events. The NNPDF3.0 [71] parton distribution functions, which have NLO accuracy, were used for all samples. The “full simulation” (FullSim) of the detector response to the generated particles was based on GEANT 4 [72] for the background. And the CMS Fast Simulation [73] (FastSim) package was used for the signal MCs, which allowed to generate a large sample for a wide range of SUSY mass parameters. Corrections were derived to correct for the differences between the two types of simulation.

Whenever available, higher order theoretical cross section calculations were used in order to normalize the simulations. Table 3.1 and 3.2 show the used values and accuracies. For top related backgrounds the recommendations of the LHC Top Physics Working Group were used. The cross section for the $t\bar{t}$ processes were calculated with the Top++2.0 program [77] in NNLO accuracy including the resummation of next-to-next-to-leading-

logarithmic soft-gluon terms. For the single top t and s channels the calculation was done in next-to-leading order (NLO) in perturbative QCD using the HATHOR program [74, 75], and approximately in next-to-next-to-leading order (NNLO) for the Wt channel [76].

The $Z + jets$ and Drell-Yan ($\gamma^*/Z+jets$) process samples are rescaled to NNLO accuracy using the calculation with the FEWZ 3.1 [78] simulation code.

3.4 Event reconstruction and object definitions

The CMS detector was introduced in Section 1.1. Events are reconstructed with the particle-flow (PF) algorithm [80] which takes into account all the information available from the detector to classify and identify physics objects. The PF candidates are categorized as electrons, muons, photons or charged/neutral hadrons from which higher-level objects e.g./ jets and isolation quantities are derived. These loosely defined objects then has to satisfy further identification and isolation criteria for the use in an analysis. This section provides information about these definitions.

3.4.1 Primary vertex

The primary vertices are reconstructed from charged particle tracks as described in [31]. Each event must contain one such vertex, which needs to have more than four degrees of freedom and located at the center of the pixel detector: $|z| < 24$ cm, $|\rho| < 2$ cm, where z is the direction along the beam and ρ is the distance in the plane transverse to the beam. In both cases

Table 3.1: Part 1 of the cross sections and their accuracies for various background processes. If there is no additional bracket denoting a considered decay channel then all possible decays are simulated. Additional phase space cuts on generator related quantities are given wherever relevant.

Sample	σ (pb)	Accuracy
$t\bar{t}$	831.76	NNLO
s -channel t/\bar{t}	10.32	NNLO
t -channel t	136.02	NNLO
t -channel \bar{t}	80.95	NNLO
Wt-channel t/\bar{t} (no fully hadronic decays)	$35.85 \times (BR = 1 - 0.676^2)$	NNLO
QCD, $H_T \in [50, 100]$ GeV	248600000.0	LO
QCD, $H_T \in [100, 200]$ GeV	279900000.0	LO
QCD, $H_T \in [200, 300]$ GeV	1712000.0	LO
QCD, $H_T \in [300, 500]$ GeV	347700.0	LO
QCD, $H_T \in [500, 700]$ GeV	32100.0	LO
QCD, $H_T \in [700, 1000]$ GeV	6831.0	LO
QCD, $H_T \in [1000, 1500]$ GeV	1207.0	LO
QCD, $H_T \in [1500, 2000]$ GeV	119.9	LO
QCD, $H_T > 2000$ GeV	25.24	LO
$\gamma^*/Z(qq)+\text{jets}$, $H_T > 180$ GeV	1187.0	LO
$Z(qq)+\text{jets}$, $H_T > 600$ GeV	5.67	LO
$W(qq)+\text{jets}$, $H_T > 180$ GeV	2788.0	LO
$W(qq)W(qq)$	51.723	NLO
$Z(qq)Z(qq)$	6.842	NLO
$W(l\nu)+\text{jets}$, $p_T^W < 50$ GeV	57280.0	NLO
$W(l\nu)+\text{jets}$, $p_T^W \in [50, 100]$ GeV	3258.0	NLO
$W(l\nu)+\text{jets}$, $p_T^W \in [100, 250]$ GeV	676.3	NLO
$W(l\nu)+\text{jets}$, $p_T^W \in [250, 400]$ GeV	23.94	NLO
$W(l\nu)+\text{jets}$, $p_T^W \in [400, 600]$ GeV	3.031	NLO
$W(l\nu)+\text{jets}$, $p_T^W > 600$ GeV	0.4524	NLO
$Z(\nu\nu)+\text{jets}$, $H_T \in [100, 200]$ GeV	$280.35 \times (k = 1.23)$	NNLO
$Z(\nu\nu)+\text{jets}$, $H_T \in [200, 400]$ GeV	$77.67 \times (k = 1.23)$	NNLO
$Z(\nu\nu)+\text{jets}$, $H_T \in [400, 600]$ GeV	$10.73 \times (k = 1.23)$	NNLO
$Z(\nu\nu)+\text{jets}$, $H_T \in [600, 800]$ GeV	$2.559 \times (k = 1.23)$	NNLO
$Z(\nu\nu)+\text{jets}$, $H_T \in [800, 1200]$ GeV	$1.1796 \times (k = 1.23)$	NNLO
$Z(\nu\nu)+\text{jets}$, $H_T \in [1200, 2500]$ GeV	$0.28833 \times (k = 1.23)$	NNLO
$Z(\nu\nu)+\text{jets}$, $H_T > 2500$ GeV	$0.006945 \times (k = 1.23)$	NNLO

Table 3.2: Part 2 of the cross sections and their accuracies for various background processes. If there is no additional bracket denoting a considered decay channel then all possible decays are simulated. Additional phase space cuts on generator related quantities are given wherever relevant.

Sample	σ (pb)	Level
$\gamma^*/Z(l\bar{l})+\text{jets}, m_{l\bar{l}} \in [5, 50] \text{ GeV}, H_T \in [100, 200] \text{ GeV}$	$224.2 \times (k = 1.23)$	NNLO
$\gamma^*/Z(l\bar{l})+\text{jets}, m_{l\bar{l}} \in [5, 50] \text{ GeV}, H_T \in [200, 400] \text{ GeV}$	$37.19 \times (k = 1.23)$	NNLO
$\gamma^*/Z(l\bar{l})+\text{jets}, m_{l\bar{l}} \in [5, 50] \text{ GeV}, H_T \in [400, 600] \text{ GeV}$	$3.581 \times (k = 1.23)$	NNLO
$\gamma^*/Z(l\bar{l})+\text{jets}, m_{l\bar{l}} \in [5, 50] \text{ GeV}, H_T > 600 \text{ GeV}$	$1.124 \times (k = 1.23)$	NNLO
$\gamma^*/Z(l\bar{l})+\text{jets}, m_{l\bar{l}} > 50 \text{ GeV}, H_T \in [200, 400] \text{ GeV}$	$40.99 \times (k = 1.23)$	NNLO
$\gamma^*/Z(l\bar{l})+\text{jets}, m_{l\bar{l}} > 50 \text{ GeV}, H_T \in [400, 600] \text{ GeV}$	$5.678 \times (k = 1.23)$	NNLO
$\gamma^*/Z(l\bar{l})+\text{jets}, m_{l\bar{l}} > 50 \text{ GeV}, H_T \in [600, 800] \text{ GeV}$	$1.367 \times (k = 1.23)$	NNLO
$\gamma^*/Z(l\bar{l})+\text{jets}, m_{l\bar{l}} > 50 \text{ GeV}, H_T \in [800, 1200] \text{ GeV}$	$0.6304 \times (k = 1.23)$	NNLO
$\gamma^*/Z(l\bar{l})+\text{jets}, m_{l\bar{l}} > 50 \text{ GeV}, H_T \in [1200, 2500] \text{ GeV}$	$0.1514 \times (k = 1.23)$	NNLO
$\gamma^*/Z(l\bar{l})+\text{jets}, m_{l\bar{l}} > 50 \text{ GeV}, H_T > 2500 \text{ GeV}$	$0.003565 \times (k = 1.23)$	NNLO
$\gamma+\text{jets}, H_T \in [40, 100] \text{ GeV}$	20730.0	LO
$\gamma+\text{jets}, H_T \in [100, 200] \text{ GeV}$	9226.0	LO
$\gamma+\text{jets}, H_T \in [200, 400] \text{ GeV}$	2300.0	LO
$\gamma+\text{jets}, H_T \in [400, 600] \text{ GeV}$	277.4	LO
$\gamma+\text{jets}, H_T > 600 \text{ GeV}$	93.38	LO
$t\bar{t}W(l\nu)$	0.2043	NLO
$t\bar{t}W(qq)$	0.4062	NLO
$t\bar{t}Z(l\bar{l}/\nu\nu)$	0.2529	NLO
$t\bar{t}Z(qq)$	0.5297	NLO
$t\bar{t}\gamma+\text{jets}$	3.697	NLO
$t\bar{t}t\bar{t}$	0.009103	NLO
$W(l\nu)W(qq)$	49.997	NLO
$W(l\nu)W(l\nu)$	12.178	NLO
$W(qq)Z(\nu\nu)$	6.488	NLO
$W(l\nu)Z(qq)$	10.71	NLO
$W(l\nu)Z(\nu\nu)$	3.033	NLO
$W(qq)Z(l\bar{l})$	5.595	NLO
$W(l\nu)Z(l\bar{l})$	4.712	NLO
$Z(qq)Z(\nu\nu)$	4.04	NLO
$Z(qq)Z(l\bar{l})$	3.22	NLO
$Z(l\bar{l})Z(\nu\nu)$	0.564	NLO
$Z(l\bar{l})Z(l\bar{l})$	1.256	NLO
WWW	0.2086	NLO
WWZ	0.1651	NLO
WZZ	0.05565	NLO
ZZZ	0.01398	NLO

0cm is the point that corresponds to the center of the detector. These cuts on the vertex positions ensure that they are within the cylinder defined by the innermost pixel layer and disks. The “leading” vertex with the highest $\sum p_T^2$ is selected as the main collision event, and all the rest of the vertices are considered to originate from pile-up. The leading vertex serves as the reference to consecutive event reconstruction steps.

3.4.2 Leptons

In the search for possible dark matter candidates, like the neutralino which carry away a fraction of the total transverse momentum, we would like to minimize the number of events which have neutrinos. It is impossible to detect them directly, because they only interact via the weak interaction which happens extremely rarely. However, one can eliminate a large fraction of them by considering the most likely production mode which is the leptonic decay of W bosons. In this process, the neutrino is accompanied by a charged lepton which is much easier to detect. The neutrino pair coming from the Z boson decay remains an irreducible background which needs to be estimated. This will be discussed more in detail in Section 3.6.5. In this subsection I discuss mainly the very loose charged lepton definitions which are used to veto leptonic events. They are also used for trigger efficiency measurements and the estimation of lost lepton which either evade the detection or somehow do not pass the selection requirements and can contaminate the signal region. To minimize this occurrence, we used a very loose definition of charged leptons. I also introduce a tighter selection for muons and electrons which was used to select $Z(\bar{\mu}^+\mu^-)$ or $Z(\bar{e}^+e^-)$ events for normalization of the $Z(\bar{\nu}\nu)$ cross section which is very hardly measurable

background.

Electrons

The tracks of the silicon tracker are associated with clusters of energy in the electromagnetic calorimeter as described in [81]. This reconstruction is done by matching the geometrical location and the momentum-energy compatibility between the track and the cluster. These reconstructed electrons are then loosely identified by two highly efficient MultiVariate classifier Algorithms (MVAs) based on a gradient boosted decision tree one of which was developed for the Higgs search with four leptons [82, 83]. We used the cuts recommended by the CMS electron and photon Physics Object Group (EGamma POG). We selected electrons with a p_T cut of 5 GeV and a cut on the pseudorapidity ($|\eta| < 2.5$) corresponding to the acceptance of the silicon tracker. These loose electrons also need to be compatible with the leading vertex of the event by satisfying a loose cut on the impact parameter significance, which is the closest distance of the track from the vertex divided by its error. Loose p_T -dependent isolation cuts are also applied. The absolute isolation is defined as the sum of the transverse momenta within a cone of $\Delta R = 0.3$ around the lepton for charged and neutral hadrons and photons from which an estimated neutral hadron pile-up contribution is subtracted. The neutral pile-up contribution for electrons is estimated using a jet area method [84]. The so-called “mini-isolation” is defined in a similar way, except that the cone has a variable size depending on the p_T of the lepton.

The cone radius is:

$$R_{\text{mini-iso}}(p_T^{\text{lep}}) = \begin{cases} 0.2 & \text{if } p_T^{\text{lep}} < 50 \text{ GeV}, \\ \frac{10 \text{ GeV}}{p_T^{\text{lep}}} & \text{if } p_T^{\text{lep}} \in [50, 200] \text{ GeV}, \\ 0.05 & \text{if } p_T^{\text{lep}} > 200 \text{ GeV}. \end{cases}$$

Cutting on this isolation variable ensures isolation in the Lorentz-boosted regime. All of the requirements for the loose electron selection can be found in Table 3.3.

Table 3.3: Loose electron definition.

Variable	Requirement
p_T	$> 5 \text{ GeV}$
$ \eta $	< 2.5
EGamma POG recommended very loose ID:	
- for $p_T < 10 \text{ GeV}$: $H(ZZ \rightarrow 4l)$ MVA ID	cut on the discriminator
- for $p_T \geq 10 \text{ GeV}$: General purpose MVA ID	cut on the discriminator
3d impact parameter significance	< 4
- for $p_T < 20 \text{ GeV}$: absolute isolation	$< 10 \text{ GeV}$
- for $p_T \geq 20 \text{ GeV}$: mini isolation / p_T	< 0.2

A tighter electron selection is also defined which was used for the Z(l) control region. It incorporates a slightly higher p_T cut, and the barrel-endcap transition region is also excluded with an additional η cut. The medium working point recommended by the EGamma POG was used for the identification. The impact parameter cuts and the isolation criteria are tighter. The summary of the tight selection is found in Table 3.4.

Differences in the reconstruction, identification and isolation efficiencies between data and MC are corrected in the simulation by using scale factors.

Table 3.4: Tight electron definition.

Variable	Requirement
p_T	> 10 GeV
$ \eta $	< 2.5 and not in $[1.44, 1.56]$
EGamma POG recommended medium ID:	
Cut based ID	pass all cuts
track $ \Delta\rho $	< 0.05 cm
track $ \Delta z $	< 0.1 cm
mini isolation / p_T	< 0.1

Muons

Muons are reconstructed by the PF algorithm using the tracks of the silicon tracker combined with the track segments found in the dedicated muon system as described in [85]. Similar to electrons, two definitions of muons are used in the analysis. We use the loose ID definition of the Muon POG for the loose selection. The other requirements are the same as that for loose electrons except for pseudorapidity range, which is slightly tighter due to the acceptance of the muon system, and the absolute isolation. The difference in the latter is in the cone size which is $\Delta R = 0.4$ and in the pile-up correction of the neutral hadron component. The contribution from pile-up is estimated by summing over the scalar value of the charged hadron transverse momenta originating from pile-up vertices and multiplying by a factor of 0.5 (corresponding to the phenomenological neutral-to-charged hadron production ratio). This subtraction is called the $\Delta\beta$ correction. The full selection is summarized in Table 3.5.

For the tightly identified selection, which is used only for the $Z(\rightarrow ll)+\text{jets}$ control region, the muons are required to pass the Muon POG recommended medium ID. The rest of the cuts are similar to that of the tight

Table 3.5: Loose muon definition.

Variable	Requirement
p_T	> 5 GeV
$ \eta $	< 2.4
Muon POG recommended loose ID:	pass all cuts
3d impact parameter significance	< 4
- for $p_T < 20$ GeV: absolute isolation	< 10 GeV
- for $p_T \geq 20$ GeV: mini isolation / p_T	< 0.2

electrons, except the η range and a slightly looser mini-isolation cut. The selection can be seen in Table 3.6.

Table 3.6: Tight muon definition.

Variable	Requirement
p_T	> 10 GeV
$ \eta $	< 2.4
Muon POG recommended medium ID:	pass all cuts
track $ \Delta\rho $	< 0.05 cm
track $ \Delta z $	< 0.1 cm
mini isolation / p_T	< 0.2

Differences in the tracking, identification and isolation efficiencies between data and MC are corrected in the simulation by scale factors.

Taus

The τ s decay around 35% of the time leptonically to neutrinos and either an electron or muon. The primary objective is to veto charged leptons so in case of the leptonic τ decays, the previously introduced loose electron and muon definitions are used. In every other case, the taus decay to an undetected neutrino and hadrons which can be identified. These tau leptons, denoted

by τ_h , are reconstructed and identified using the “hadron-plus-strips” algorithm (more details can be found in [86]). The charged and neutral particles found by the PF algorithm are clustered into a jet with a distance parameter of $\Delta R = 0.5$ by the anti- k_T algorithm [87]. These jets are serving as the τ_h candidates for the reconstruction step which selects only the ones which are compatible with possible hadronic decay modes of the τ . For the identification they are required to pass further isolation criteria that greatly reduce the fake rate due to quark and gluon jets. The Tau POG recommended loose isolation working point was used for the veto selection. Also, the kinematic cuts were kept the same as the ones determined by the reconstruction step ($p_T > 18$ GeV and $|\eta| < 2.5$).

3.4.3 Photons

Photons are reconstructed from ECAL clusters as described in [88]. Further identification steps are based on the ratio of energy deposits between HCAL and ECAL, shower shape variables and isolations. In this analysis, the EGamma POG recommended cut based medium ID was applied for a photon enriched control sample that was used in the estimation of the $Z(\nu\nu)+\text{jets}$ contribution to the signal region. Reconstructed electrons which are compatible with the same supercluster are vetoed. The full selection is shown in Table 3.7.

3.4.4 Jets and higher order objects, variables

Jets in this analysis are clustered from the physics objects of the PF algorithm by the anti- k_T algorithm [87] using the FASTJET implementation [89] with two separate distance parameters, $\Delta R = 0.4$ for ordinary (abbreviated

Table 3.7: The definition of photons.

Variable	Requirement
p_T	$> 80 \text{ GeV}$
$ \eta $	< 2.5
EGamma POG recommended cut based Medium ID	pass all cuts
electron veto	pass

as “AK4”) and b-tagged jets (or simply b jets) and $\Delta R = 0.8$ for W and top-tagged jets (which will be referred to as “AK8” jets from now on). Charged hadrons which do not originate from the leading vertex are removed using the Charged Hadron Subtraction(CHS) method [90] which greatly reduces the number of jets originating from pile-up. Then the 4-momentum of the jets are corrected by a jet-area-based method [84, 91, 97] which removes any remaining contributions from pile-up and corrects for non-uniform detector response and residual jet energy scale differences between data and simulation. Finally, a jet energy resolution smearing technique [97] is used in the simulation to better match the resolution observed in data. After these reconstruction steps, the jets are identified using the Jet-MET POG recommended “loose” and “tight” jet IDs [17] for AK4 and AK8 jets respectively. The identification is based on the neutral and charged particle energy fractions measured both in the ECAL and HCAL and the number and type of jet constituents. The AK4 and AK8 jet selections are shown in Table 3.8 and 3.9 respectively.

***b*-tagged jets**

The AK4 jets defined in the previous subsection which satisfy further *b* quark decay identification criteria are referred to as b-tagged jets. In order to

Table 3.8: The AK4 jet selection.

Variable	Requirement
R	$= 0.4$
p_T	≥ 30 GeV
$ \eta $	< 2.4
JetMET POG recommended loose jet ID	pass

Table 3.9: The AK8 jet selection.

Variable	Requirement
R	$= 0.8$
p_T	≥ 200 GeV
$ \eta $	< 2.4
JetMET POG recommended tight jet ID	pass

discriminate from light flavor quark and gluon jets, the combined secondary vertex (CSV) multivariate b-tagging algorithm [93] is used which takes into account the longer lifetime of the bottom quark decay (which can result in the finding of a displaced secondary vertex), the higher invariant mass and multiplicity of decay products. The CMS BTag POG recommended “loose” working point is used for vetoing, which has an efficiency of around 81% and a mistagging rate of 8.9%. Additionally, the “medium” working point is used for selecting jets which has an efficiency of 63% and a mistagging rate of 0.9%. Differences in the performance of the algorithm between data-MC and also FastSim-FullSim was corrected by the application of scale factors.

Boosted W s and $tops$

As introduced in Section 1.4, the hadronically decaying boosted W bosons and top quarks are tagged with the wider cone AK8 jets. For the determi-

nation of the jet 4-momentum, the CHS algorithm and the corresponding jet energy scale corrections are used. The jets are also matched to similar jets but clustered after the application of PUPPI weights [16] to its jets constituents and groomed with the SoftDrop algorithm [14]. The mass of these jets, which is used for the boosted object tagging, is seen to be more stable with respect to the number of pile-up [17], therefore we used the PUPPI corrected values to “mass-tag” the jets by applying cuts close to the W and top mass peak. In order to further reduce the multijet background, the N-subjettiness variables [15] are calculated for matched PUPPI jets, which are defined as

$$\tau_N = \frac{1}{R_0 \sum_i p_{T,i}} \sum_i p_{T,i} \min(\Delta R_{1,i}, \Delta R_{2,i}, \dots, \Delta R_{N,i}), \quad (3.1)$$

where N stands for the number of candidate subjet axes, i is the number of jet constituents and R_0 is the characteristic jet radius. The ratios of $\tau_{21} = \tau_2/\tau_1$ and $\tau_{32} = \tau_3/\tau_2$ are used for tagging W bosons and top quarks respectively. Finally, one of the subjets of the top-tagged jets also need to satisfy a b-tagging requirement using the CSV algorithm [93]. The full selection for selected W s and $tops$, which was recommended by the CMS Jet-MET POG, is shown in Table 3.10. The W selection has an efficiency of around 66% with a QCD mistagging rate of 4%, while the top selection has an efficiency of 15% with a 0.1% mistagging rate [17]. The discrepancies in performance between Data-MC and FastSim-FullSim are corrected with scale factors.

Table 3.10: Definition of tagged W s and tops.

Variable	Requirement for W	Requirement for top
p_T (CHS)	> 200 GeV	> 400 GeV
$ \eta $ (CHS)	< 2.4	< 2.4
SoftDrop mass (PUPPI)	$\subset [65, 105]$ GeV	$\subset [105, 210]$ GeV
τ_2/τ_1 (PUPPI)	< 0.4	–
τ_3/τ_2 (PUPPI)	–	< 0.46
subjet btag CSV (CHS)	–	> 0.5426 (loose WP)

Missing transverse momentum

The visible momentum imbalance vector, which is also known as the missing transverse momentum and denoted as \vec{p}_T^{miss} , is reconstructed [94] by using the visible final state particles of the PF algorithm. It is defined as the negative vector sum of the transverse momenta of all PF particles which are consistent with the leading primary vertex of the event. The magnitude of this vector is referred to as p_T^{miss} . Further corrections are applied to the value in order to adjust for minimum energy thresholds and non-linearities in response to hadrons in the calorimeters and inefficiencies and p_T thresholds that are present in the tracker. These, so-called ‘‘Type-1’’ corrections are done by propagating the effects of jet energy corrections applied to jets to the vectorial sum. In order to remove anomalous events, which contain misreconstructed physics objects or detector failures, filters are applied to both data and simulations. The list of these filters are as follows:

- a primary vertex filter: removes events which do not contain at least one good vertex (defined in Section 3.4.1) compatible with the LHC beam;
- ECAL filters: detect spurious deposits due to missing information from

partly dead cells or particle interactions, which produce anomalously high energy superclusters;

- HCAL filters: identify events with significant noise which arise in the hybrid photodiodes and readout electronics of the barrel or due to direct particle interactions with the endcap components;
- Beam halo filter: removes events where large deposits of energy are found in the detector due to LHC beam collisions with beam gas that results in highly energetic particles (beam halo) traveling nearly parallel to the beam;
- Reconstruction filters: eliminate events which contain badly reconstructed muon or charged hadron PF candidates due to misreconstruction of the particle trajectory from the silicon tracker informations.

Razor variables

The Razor variables were briefly introduced in Section 1.3. The exact definitions are given here. Let us suppose that massive pair-produces particles, denoted by G_1 and G_2 , which in our case can be the gluinos or the top squarks, each decay to a massless visible particle Q_1 and Q_2 , and a massive, stable and undetected particle, corresponding to the neutralino, which is denoted by χ_1 and χ_2 .

In the rough-approximation (R-) frame the magnitudes of the visible decay products of the heavy particle pair are equal:

$$|\vec{p}_{Q_1}^R| = |\vec{p}_{Q_2}^R| = \frac{M_\Delta}{2}, \quad (3.2)$$

and can be used to estimate the characteristic mass scale, $M_\Delta = \frac{M_G^2 + M_\chi^2}{M_G}$.

With the rough approximation, the R-frame is calculated as:

$$\beta_R = \frac{E_{Q_1}^{lab} - E_{Q_2}^{lab}}{p_{z,Q_1}^{lab} - p_{z,Q_2}^{lab}}. \quad (3.3)$$

The longitudinal boost invariant R-frame mass, which is defined as $M_R \equiv 2|\vec{q}^R| = M_\Delta$ can then be expressed with purely lab-frame quantities as:

$$M_R \equiv \sqrt{\frac{(p_{z,Q_1} E_{Q_2} - p_{z,Q_2} E_{Q_1})^2}{(p_{z,Q_1} - p_{z,Q_2})^2 - (E_{Q_1} - E_{Q_2})^2}}. \quad (3.4)$$

In order to separate the visible, hadronic decay products of the main collision event, all visible particles are clustered into AK4 jets with the definition given in Section 3.4.4. The Razor calculation requires at least two such jets in the event to establish the dijet topology. If there are additional jets in the event their 4-momenta are merged into that of the existing two jets to form so-called ‘‘megajets’’ depending on the following criteria: the constituents of the megajets are required to be on two separate hemispheres in such a way that the invariant mass of the two megajets reaches the smallest value. This choice of megajets are meant to separate the visible decay products for each pair-produced hypothetical heavy particle.

There exists an improved definition of M_R [95], where the transverse component of the boost required to transform to the center-of-mass frame is not neglected:

$$M_R \equiv \sqrt{(|\vec{p}_{j_1}| + |\vec{p}_{j_2}|)^2 - (p_z^{j_1} + p_z^{j_2})^2}, \quad (3.5)$$

where j_1 and j_2 denote the two megajets explained above.

A second way to estimate the characteristic mass scale, M_Δ , uses only the transverse momentum information and therefore gives a way to account

for the momentum imbalance given by neutralinos. With the assumption, that the missing momentum is divided equally among the neutralinos, the transverse mass estimator, M_T^R is then defined as:

$$M_T^R \equiv \sqrt{\frac{p_T^{miss}(p_T^{j1} + p_T^{j2}) - \vec{p}_T^{miss} \cdot (\vec{p}_T^{j1} + \vec{p}_T^{j2})}{2}}. \quad (3.6)$$

The above two variables estimate the same mass scale, so their ratio, the dimension-less R-frame razor variable, is a useful additional discriminator which is defined as:

$$R \equiv \frac{M_T^R}{M_R}. \quad (3.7)$$

It typically peaks around 0.5 for the signal (due to the geometrical limitation of only using the transverse information) and around 0 for the background.

In the analysis, it is customary to use the square of the above value R^2 . There is one more quantity related to the Razor calculation, that is useful in the suppression of the multijet background. It is the angle $\Delta\phi$ between the two megajets in the projected plane transverse to the beam axis. Most backgrounds with no invisible particles (which create non-zero p_T^{miss}) produce megajets which are very likely back-to-back, so $|\Delta\phi|$ tends towards π . While signals which have invisible particles, like the neutralino, have a larger probability to produce smaller $|\Delta\phi|$ values, so this quantity is an additional useful signal discriminator.

3.5 Event selection

This section describes a common baseline selection (including the trigger choice) and the signal region. The baseline selection is a minimal event selection that is common for both the signal and control regions (defined in Section 3.6). Events in the control region are also used for the background estimation.

3.5.1 Baseline selection

In the baseline selection, each event is required to:

1. pass all missing transverse momentum filters specified in Section 3.4.4;
2. have at least one identified AK8 jet;
3. have at least three (or four) identified AK4 jets for *top* (and *W*) final states;
4. satisfy very loose cuts on the Razor variables: $M_R \geq 800$ GeV and $R^2 \geq 0.08$;
5. pass the hadronic trigger selection which is specified in the next subsection 3.5.2.

The AK8 jet is required so that there is at least one candidate jet that can satisfy the boosted object tagging requirements. Although the Razor algorithm only requires two AK4 jets, it was seen from a sensitivity study that requiring slightly more jets give a better sensitivity to the boosted phase space of the SUSY signals. This is explained in Section 3.5.3. Figure 3.3 shows the distribution of the razor variables after the baseline selection.

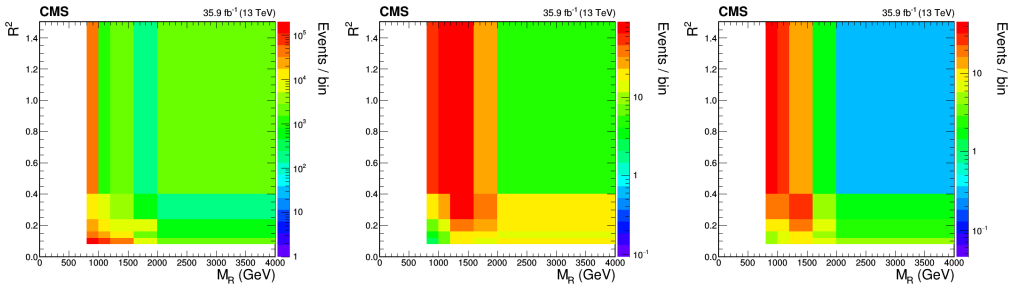


Figure 3.3: Two dimensional Razor distributions of R^2 vs M_R for the standard model background (left) and two selected signal samples in the baseline selection region. The middle plot shows the T5ttcc signal with $m_{\tilde{g}} = 1.4$ TeV, $m_{\tilde{t}} = 320$ GeV and $m_{\tilde{\chi}_1^0} = 300$ GeV. The right plot depicts the distribution for the T2tt model with $m_{\tilde{t}} = 850$ GeV and $m_{\tilde{\chi}_1^0} = 100$ GeV.

3.5.2 Trigger

Data events were selected by a two-level trigger system. A so-called “level 1” hardware filter preselects events in real time based on the raw detector data and passes them to a “high-level” trigger (or HLT in short). Compared to the hardware filter, the HLT performs a slightly slower and more complicated, so-called “online” event reconstruction still during the data collection. It makes the final decision whether to record the events for analysis. This decision is still much faster than the lengthy “offline” reconstruction which provides the ultimate precision and accuracy that is required for the analysis. The events were selected by fully hadronic triggers which select events based on the presence of an AK8 jet with $p_T \geq 450$ GeV or if the scalar sum of the AK4 jets, denoted by H_T , is at least 800 GeV or 900 GeV. These triggers are not fully efficient in the signal and control regions, therefore the efficiency of their combination was measured in datasets collected with other, orthogonal control triggers. These triggers selected either one muon (denoted as `SingleMuon`), electron (`SingleElectron`) or a photon

(SinglePhoton), or required a minimum value on the missing transverse momentum (MET). Additionally, the collected events were required to pass the baseline selection of Section 3.5.1. The charged leptons were required to be isolated. The minimum p_T threshold of muons was 24 GeV, while the one for electrons changed during the year from 23 GeV initially and 27 GeV later on in the same year. Additionally, we required them to pass the loose object definitions of Section 3.4.2. The photon thresholds in the online reconstruction ranged from 22 – 600 GeV, but a large fraction of the events were discarded below 165 GeV. The photons in these events had to pass the photon definition in Section 3.4.3. The requirement for the missing transverse momentum trigger was $p_T^{miss} > 120$ GeV. In all cases, we vetoed events which contained at least one lepton which was not selected by any of the single lepton triggers. The efficiencies of the hadronic analysis triggers were measured as a function of the variables, shown in Figure 3.4, which were used to select the events during data collection. The measurements were done in bins along two dimensions, after which the measurement points in each bin were “unrolled” into a single one-dimensional plot in order to better visualize them together with their uncertainties. These efficiencies were used to weight the background and the signal simulation events both of which were not required to pass any simulated trigger decision that is often not very reliable (the difference can be seen on the plots). Figure 3.5 shows the efficiencies as a function of the Razor variables which indicate that the triggers are nearly fully efficient in the most sensitive search bins which are usually the higher M_R and R^2 bins. Due to significant observed differences between measurements in the various datasets because of the existence of a lepton or a photon, the events were weighted by the measurement corresponding to the presence of the specific physics object. In case no such object (lepton or

photon) existed in the event, the weight was taken from the measurement in the MET dataset. This decision was seen to improve Data-MC agreement in the control regions which are defined in later sections. The statistical error of the trigger efficiency measurement was calculated with the Wilson score interval and used as a systematic uncertainty.

The difference of trigger efficiency measured with the different control triggers is mainly due to the mismeasurement of the photon or lepton contribution to the jet energy when these objects are parts of the jet constituents. Figure 3.6 show the distribution of photons as a function of the photon-jet distance vs./ photon/AK4 jet p_T ratio and the distribution of this ratio for tightly matched photons. There is an inconsistency seen in data which is larger than that seen in the simulation. Similar differences are seen for muons and electrons and also AK8 jets. The online measurements of H_T and AK8 jet p_T , which are used for the trigger decision, are also affected by the mismeasurement, which explains the different efficiency measured in the various datasets.

3.5.3 Signal selection

The signal regions must satisfy the baseline selection criteria as described in Section 3.5.1. On top of that, charged leptons are vetoed in order to suppress leptonic background events which have a high probability to also contain undetected neutrinos. In order to suppress the QCD multijet background, a cut is required on the $|\Delta\phi|$ between the two megajets. All possible signals of interest have at least two *top* quarks in them, so the chance that one of them gains a sufficient boost is high. Therefore, the events are split into different categories based on the presence of at least one *top*-tagged AK8

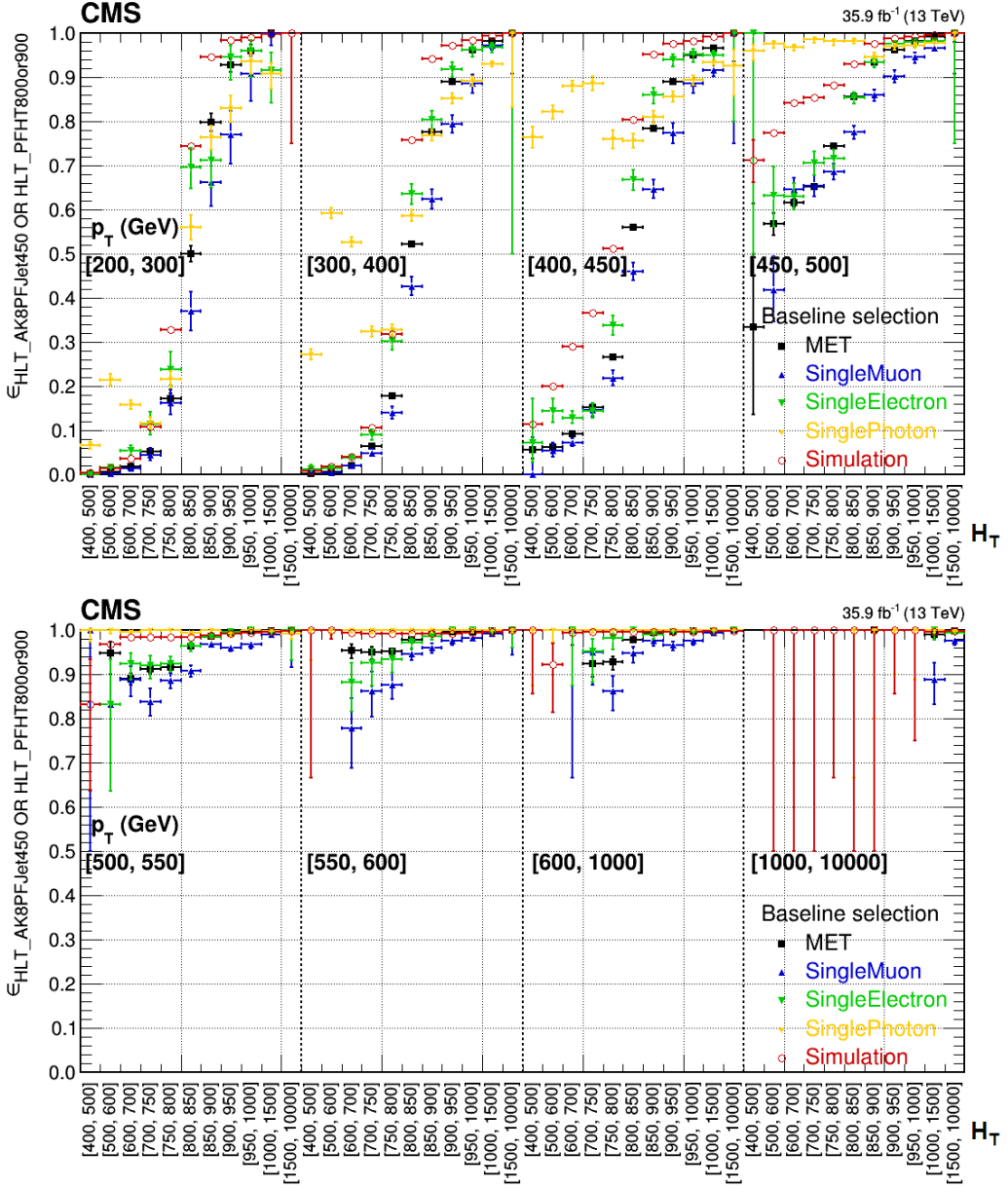


Figure 3.4: Unrolled trigger efficiencies as a function of H_T and AK8 jet p_T obtained from the SingleElectron, SingleMuon, SinglePhoton, MET datasets and Simulation for the lower 4 (top) and higher 4 (bottom) hardest jet p_T bins. The x-axis show H_T values for each bin.

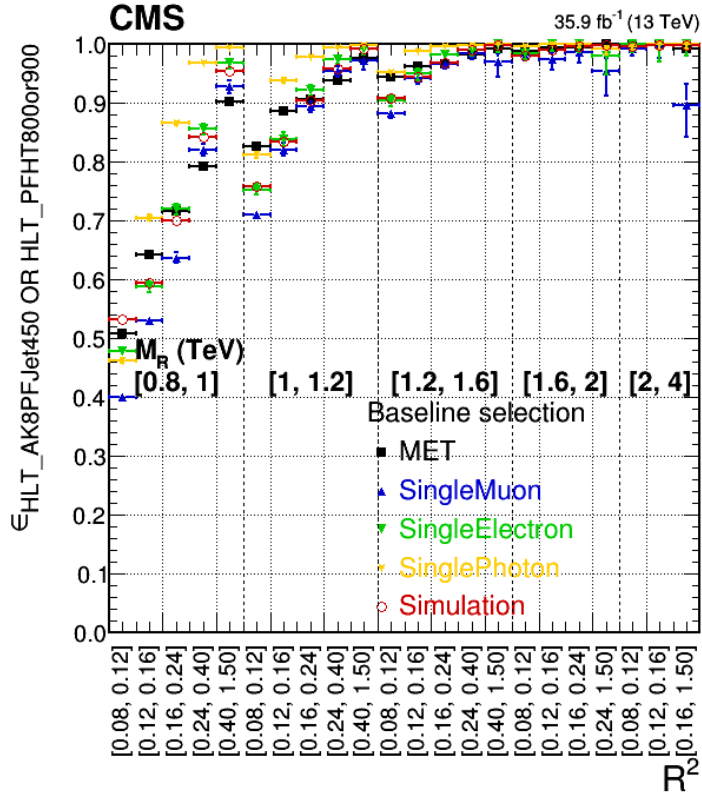


Figure 3.5: Unrolled trigger efficiencies as a function of M_R and R_2 obtained from the SingleElectron, SingleMu, SinglePhoton, MET datasets and Simulation.

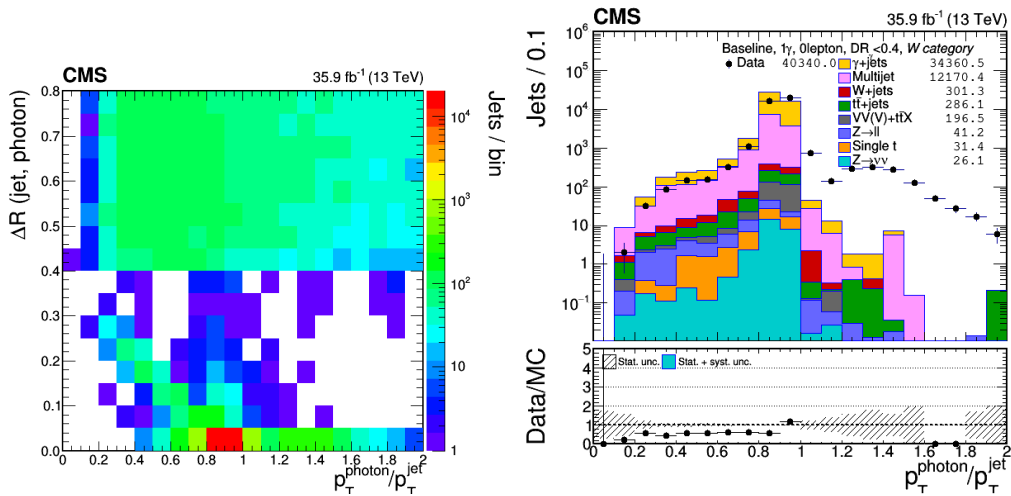


Figure 3.6: (Left) AK4 jet-photon distance vs ratio of photon p_T to AK4 jet p_T in data and (right) the distribution as a function of the ratio for photons tightly matched to the jet ($\Delta R < 0.4$) for both data and simulation. The plotted event region is defined by the baseline selection, exactly one selected photon, which is added to the missing transverse momentum, and lepton veto. There is a discrepancy both between the energy reconstruction of the jet and the photon and also between data and simulation.

jet, or in case no such jet is present, at least one W -tagged AK8 jet and a b -tagged AK4 jet. The reason for the difference in the number of required jets in the baseline selection is partly due to the difference in the level of boost one of the top quarks receives. In case of the boosted top final states, one of the $tops$ is sufficiently boosted so that the decay products (a b jet and two light quark jet from the W decay) end up in one large cone jet which is tagged. On top of that it is only required to have at least two other jets from initial state radiation or the decay of the other top quark. In case of the W final states one of the $tops$ decay to a b jet and another highly energetic boosted W jet so, similarly to the boosted top scenario, it is required to have only two additional jets. The distributions of the number of jets are shown in Figure 3.7. The boosted W event categories are subdivided based on the jet multiplicity, which defines all together three separate signal regions which are summarized in Table 3.11. The binning in jet multiplicity gives additional sensitivity for low or larger jet multiplicity signals. For example, the T1tttt model has two additional $tops$ in the final state compared to the T2tt, so a larger jet multiplicity bin is more sensitive.

The signal regions are further subdivided to bins of $M_R = 800, 1000, 1200, 1600, 2000, 4000$ and bins of $R^2 = 0.08, 0.12, 0.16, 0.24, 0.4, 1.50$. This binning was seen to provide optimal significance in the high M_R high R^2 ranges. Some of these sensitive bins were merged in order to reduce the statistical uncertainty: the R^2 bins $[0.24, 0.4, 2.0]$ are merged for $M_R = [1600, 2000]$ and the R^2 bins $[0.16, 0.24, 0.4, 2.0]$ are merged for $M_R = [2000, 4000]$. Figure 3.8 shows the distribution of simulation events in these bins for the three event categories.

Table 3.11: Signal region definitions.

Selection	W categories	top category
Trigger	$H_T^{online} \geq 800$ GeV OR $p_{T,AK8jet}^{online} \geq 450$ GeV	
Razor	$M_R \geq 800$ GeV, $R^2 \geq 0.08$, $ \Delta\phi < 2.8$	
Lepton	0 loose electron, 0 loose muon, 0 tau	
Boosted obj. p_T $ \eta $ $M_{Soft-drop}$ N-sub. Subjet b -tag	$\geq 1W$ (and 0 top) ≥ 200 GeV < 2.4 [65, 105[GeV $\tau_{21} < 0.4$ -	$\geq 1top$ ≥ 400 GeV < 2.4 [105, 210[GeV $\tau_{32} < 0.46$ ≥ 1 (loose)
b-tag	$\geq 1b$ (medium)	-
N_{jet}	[4, 5]	≥ 6
		≥ 3

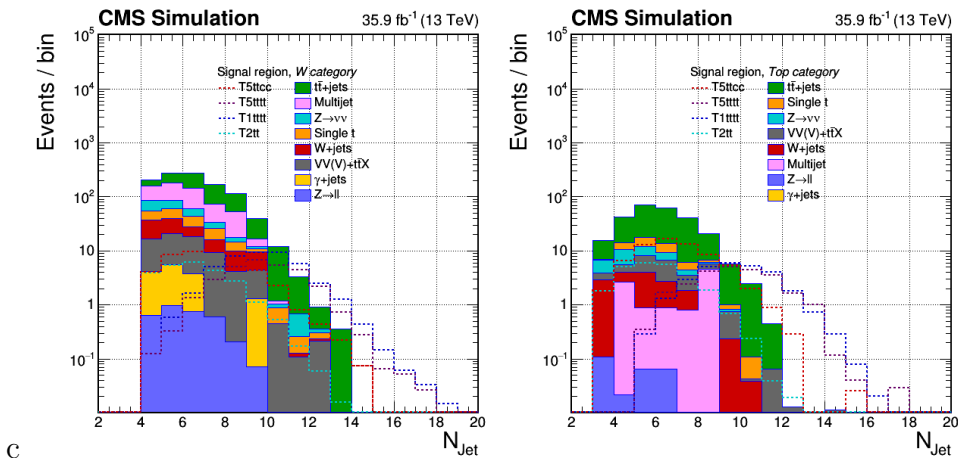


Figure 3.7: The distribution of AK4 jet multiplicities the background and selected signal points in the W (left) and top (right) event categories. The signal benchmarks shown are T5ttcc ($m_{\tilde{g}} = 1.4$ TeV, $m_{\tilde{t}} = 320$ GeV and $m_{\tilde{\chi}_1^0} = 300$ GeV), T1tttt ($m_{\tilde{g}} = 1.4$ TeV and $m_{\tilde{\chi}_1^0} = 300$ GeV) and T2tt ($m_{\tilde{t}} = 850$ GeV and $m_{\tilde{\chi}_1^0} = 100$ GeV).

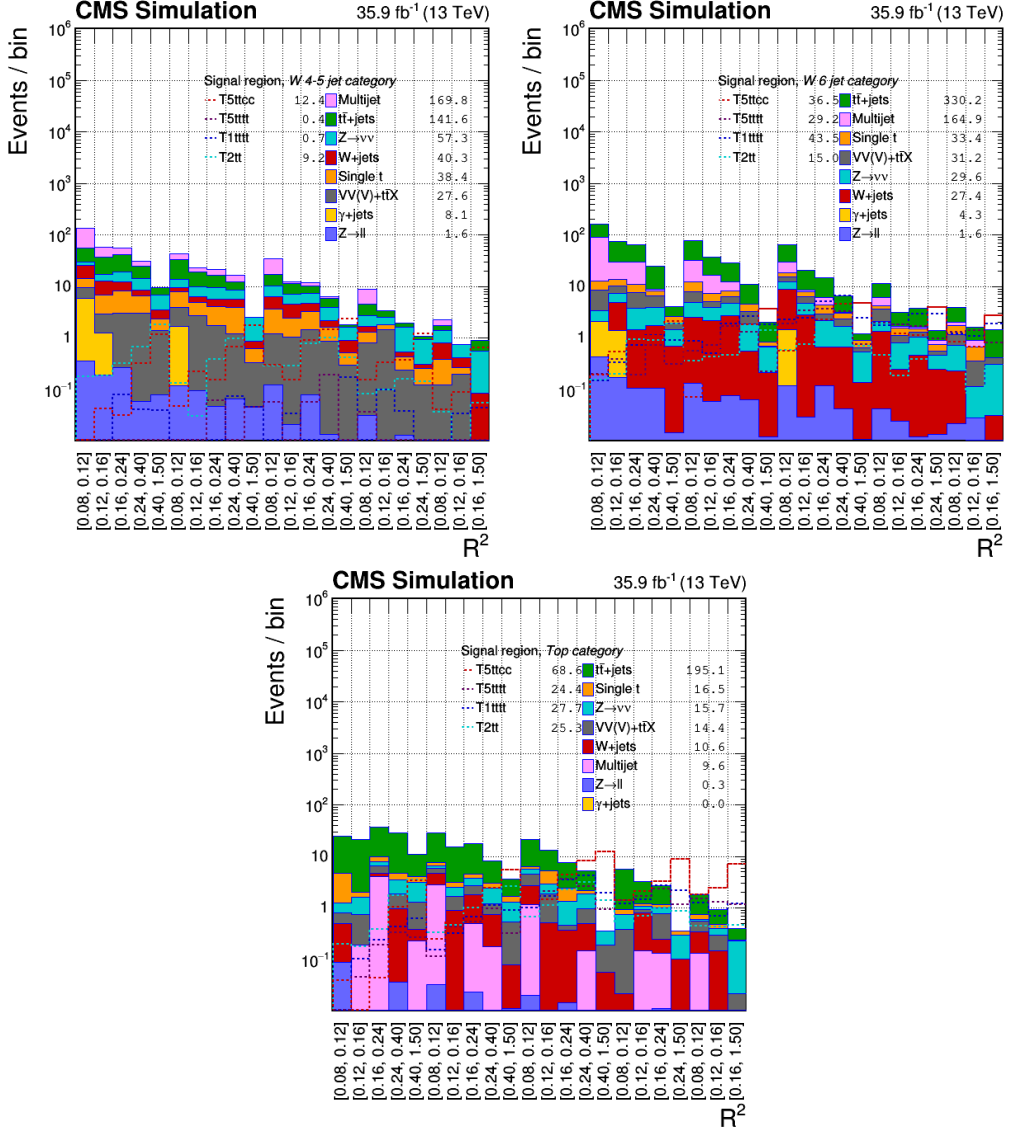


Figure 3.8: The distribution of events in the unrolled razor bins for the *W* 4-5 jet (top left), *W* 6 ≤ jet (rop right) and *top* (bottom) categories. The signal benchmarks shown are T5ttcc ($m_{\tilde{g}} = 1.4$ TeV, $m_{\tilde{t}} = 320$ GeV and $m_{\tilde{\chi}_1^0} = 300$ GeV), T1tttt ($m_{\tilde{g}} = 1.4$ TeV and $m_{\tilde{\chi}_1^0} = 300$ GeV) and T2tt ($m_{\tilde{t}} = 850$ GeV and $m_{\tilde{\chi}_1^0} = 100$ GeV).

3.6 Background estimation

There are three types of backgrounds in the signal regions. The most dominant one contains one lepton which is not found. It can be either because the lepton fails isolation or identification criteria, or it was not reconstructed due to inefficiencies or fell outside the acceptance of the detector (eg. went through gaps). In the largest production mode of these leptons, a neutrino is also present which can give rise to a large missing transverse momentum, which in turn is responsible for a large R^2 . The largest such background is $t\bar{t}$ (dominantly semi-leptonic decays) or single $tops$ (mostly the leptonic decay of $tops$ produced by the Wt channel). This background is the most dominant, because there is a very high chance that a top quark in the event decays hadronically and it can produce either a tagged top or a tagged W and a b jet, depending on the level of the boost. These processes are estimated together. The other significant lost lepton background is W +jets, where the W boson decays leptonically while one of the jets in the event fakes a tagged top or W . The second type of background is the multijet which is dominantly produced by QCD but also includes hadronic decays of gauge bosons and Drell-Yan. In these processes, the tagged boosted objects can be real or fake (mostly the latter). There are no neutrinos which could cause a larger momentum imbalance; instead, the missing transverse momentum could only arise from the mismeasurement of the jet p_T , therefore the R^2 distributions of these processes fall more rapidly compared to the lost lepton backgrounds which have a neutrino. The third most dominant and irreducible background type is Z +jets, where the Z boson decays to a pair of undetected neutrinos and the additional jets are mistagged as a top or a W and b jet. For the estimation of the backgrounds, we could not fully

rely on the MC. The simulation was only used to estimate the rarer processes. For the four main backgrounds, a data driven estimation procedure was used. Control regions were defined which try to isolate or approximately mimic each main process without being contaminated by any possible signal contribution. The non-dominant processes are subtracted from the control region (CR) data counts and MC correction factors are derived for each signal region (SR) bin using the ratio of events between data and MC in the control region. These multiplication factors, which are applied bin-by-bin on the simulated event yields, correct for possible residual differences between data and MC. The background estimation method is then validated with so-called ‘‘closure-tests’’ in regions which are very similar to the signal region. These tests are found in Section 3.6.6. The general formula for the background estimation procedure is shown in Equation 3.8.

$$N_{i,SR}^{Est} = \left(N_{i,CR}^{data} - N_{i,CR}^{MC, not\ process} \right) \cdot \frac{N_{i,SR}^{MC, process}}{N_{i,CR}^{MC, process}} \quad (3.8)$$

where N stands for the event counts, and i is the search bin. Since this procedure relies partly on simulation there was an issue with bins which did not have any MC events. The procedure to deal with this was different for the control and signal regions. For the former, an additional merging of nearby bins allowed to eliminate the problem. This modified Equation 3.8 the following way:

$$N_{i,SR}^{Est} = \sum^{process} \left[\left(N_{j,CR}^{data} - N_{j,CR}^{MC, not\ process} \right) \cdot \frac{N_{i,SR}^{MC, process}}{N_{j,CR}^{MC, process}} \right] + \sum^{rare} N_{i,SR}^{MC, rare}.$$

For the empty signal region bins, the solution was to extrapolate events from a slightly looser signal region which had relaxed N-subjettiness re-

quirements. This is explained in the next subsection. The only exception to the above formula is for the estimation of $Z(\rightarrow \nu\nu)+\text{jets}$ events which is slightly different and is explained in detail in Section 3.6.5.

3.6.1 Extrapolation of events from loosened signal regions

In order to retain the kinematic characteristics of the signal regions as much as possible, a looser signal region is defined which has the same selection as that of the signal region except for the N-subjettiness requirement of the tagged objects. The loose region is defined by modifying the following criteria of the signal regions:

- W category: remove the τ_{21} cut and allow so-called “low purity” W tags.
- top category: loosen the τ_{32} selection to the loosest top tagging working point defined by the JetMET POG, which is $\tau_{32} < 0.8$.

It was seen that the distribution of events as a function of the razor variables in the loosened region had a very similar shape to that of the signal region, but the number of events was considerably higher. For this reason, the loosened region which contained events in most of the empty bins of the signal region was very suitable to be used as a base for the extrapolation to the signal region for the empty bins. Figure 3.9 shows the extrapolation for the $W+\text{jets}$ process. Despite the loosening, it is possible that a few bins remain unpopulated. For these bins, a Garwood upper limit is set (shown with the red color), which is 1.83 times the RMS event weight of the previous populated bin. From the observed similarity of the shape of the razor distributions for the populated bins a constant ratio between the two distributions

is assumed. An estimate of this ratio is used as a multiplication factor to extrapolate from the loose region to the signal region. The ratio is estimated from convoluted Gaussian distributions with means corresponding to the ratios of loose-to-signal region events in the populated signal region bins and widths corresponding to the statistical error of these bin ratios (using the black points in the lower panels of the plots in Figure 3.9). These Gaussians are shown with purple colors in Figure 3.10. They are then convoluted for each M_R bin separately, which is shown with the green colors. Then the medians and up/down limits corresponding to the 68% area are computed for each M_R bin. The average of these medians, which is used as the estimated extrapolation factor, and their up/down limits which correspond to the assigned (conservative) extrapolation uncertainty are shown in Figure 3.10 with the solid lines. As a comparison, the same quantities are shown for the total convolution of all Gaussians (shown with black curve) denoted by the dashed lines which in general are close to the previous averages.

The following subsections cover the estimation of the four main backgrounds in more detail.

3.6.2 $t\bar{t}$ and single top

The control region for single top and $t\bar{t}$ background is very similar to the signal except for the vetoing of charged leptons, in that exactly one loose electron or muon is required in the event. It enriches this region with events with very similar kinematics except that the lepton is not lost. In order to greatly reduce signal contamination from SUSY events, a cut on the W transverse mass, M_T , is applied, which is computed from the lepton four-momentum and p_T^{miss} . In theory, this quantity is always smaller than the

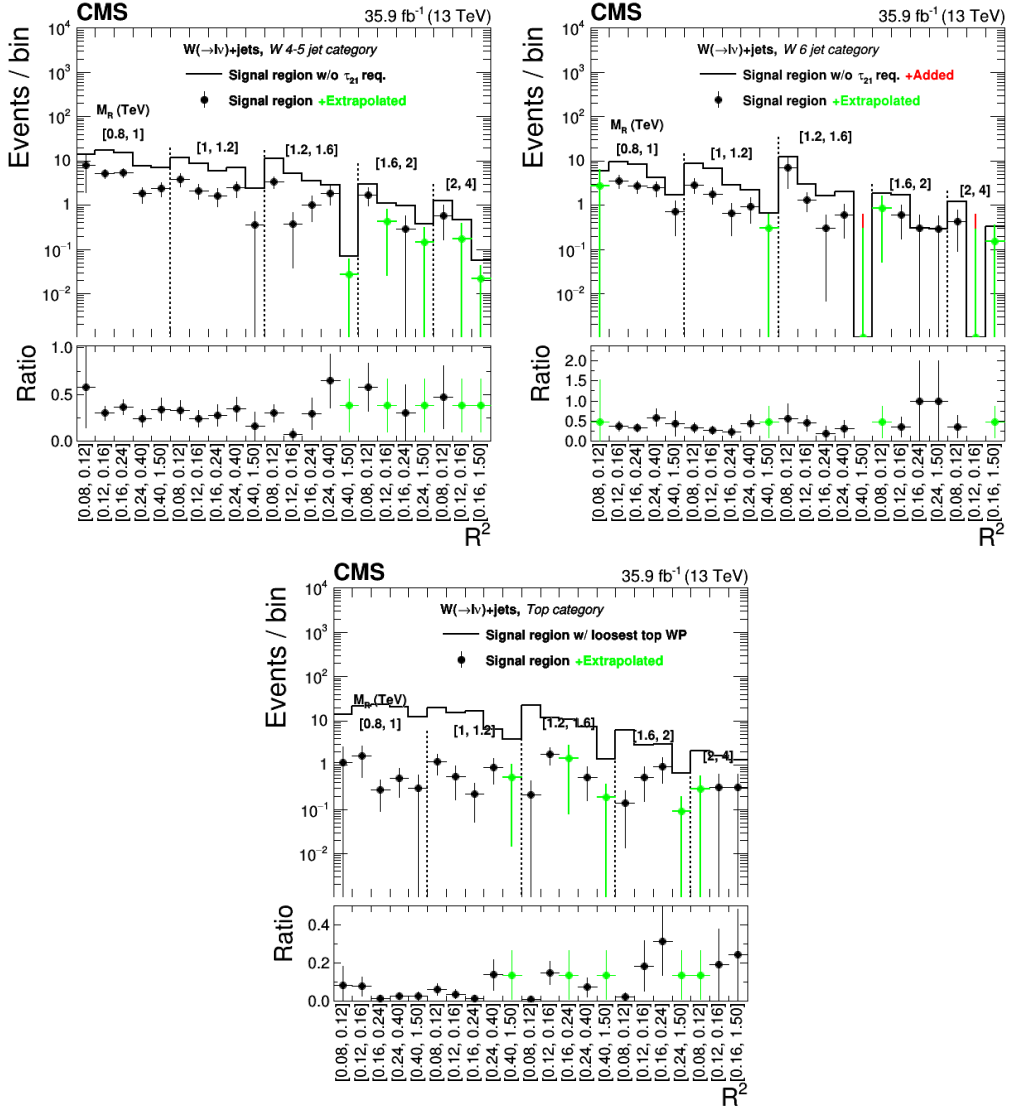


Figure 3.9: Extrapolation of $W(\rightarrow l\nu)+\text{jets}$ events to the signal region from events of the loose signal region for the W 4–5 jet, W $6 \leq$ jet and top event categories. The black markers of the upper panel show the signal region and the black line the loosened signal region event distributions of the simulation. The red error bars show estimated upper limits on the zero count bins of the loose region obtained by multiplying 1.83 times the RMS event weight of the previous populated bin. The green dots show the extrapolated signal region counts by multiplying the loose region counts by the estimated event ratio. Black dots of the lower panels show the loose-to-signal region ratios. The green dots show the estimated extrapolation factor from a convolution method.

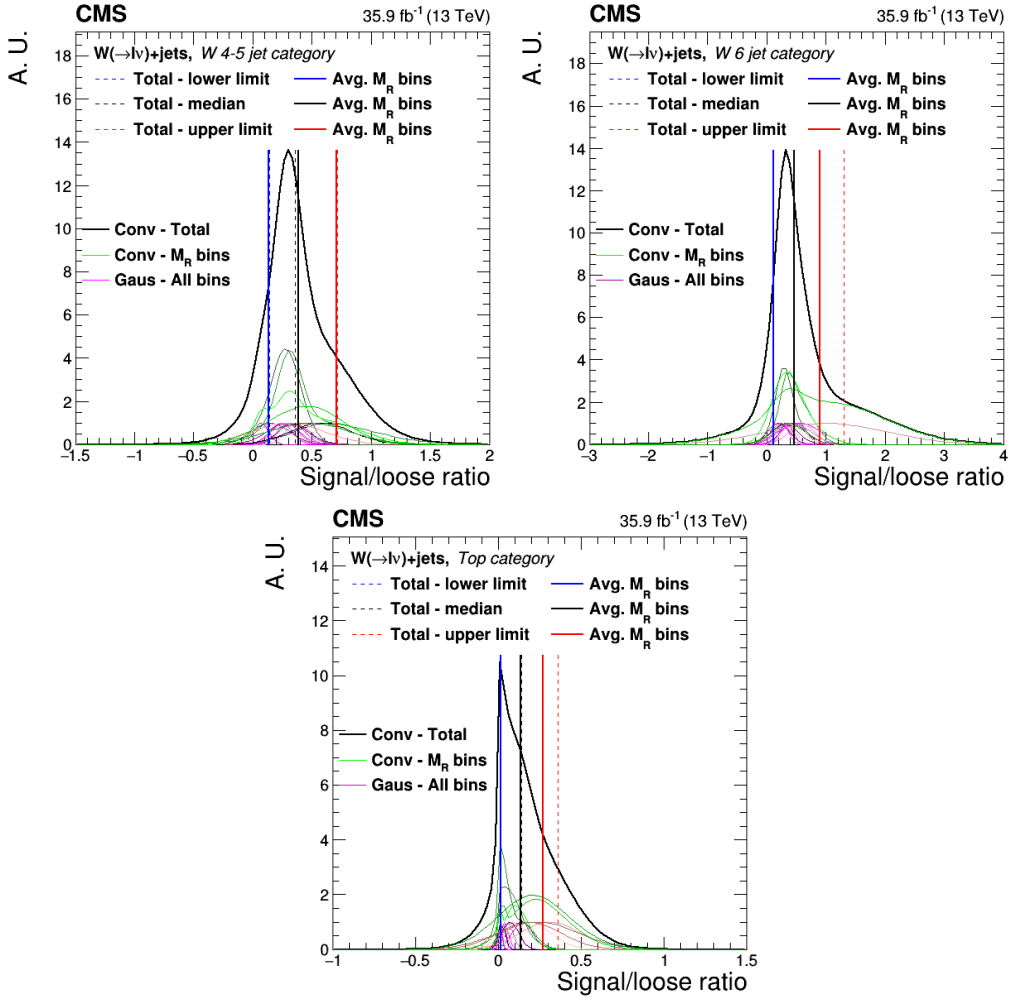


Figure 3.10: Estimation of loose-to-signal region extrapolation ratio uncertainties for the $W(\rightarrow l\nu)+\text{jets}$ simulation events for the W 4–5 jet, W $6 \leq$ jet and *top* event categories. Please, refer to the text for further details on this procedure.

actual mass of the W ; therefore, it can be used to purify the selection to include only one leptonically decaying W , while SUSY signals tend to have much larger values due to the neutralinos. Figure 3.11 shows the M_T distributions before applying the specific cut on them (we refer to them as “N-1” distributions). The applied cut is $M_T < 100$ GeV which create a region that is more than 85% pure in single top and $t\bar{t}$ events with negligible signal contamination. The bottom panel of these plots (and many similar plots shown later) include the ratio of Data to MC events and the corresponding statistical error with black markers. It also contains the statistical and all of the additional systematic uncertainties (added in quadrature) on the MC prediction shown with the dashed and grey bands respectively. The systematic uncertainties are described more in detail in Section 3.7.

The full selection of the top control region is then:

- baseline selection;
- = 1 loose electron or muon;
- W category: ≥ 1 medium b jet and ≥ 1 W -tagged AK8 jet;
- top category: ≥ 1 top -tagged AK8 jet;
- $|\Delta\phi_{mega,jets}| < 2.8$;
- $M_T < 100$ GeV.

Figure 3.12 shows the unrolled version of the two-dimensional M_R vs. R^2 distribution of events in the $t\bar{t}$ and single top enriched control region. The obtained region is more than 85% pure in $t\bar{t}$ and single top events. The corresponding contribution to the total background in the signal region is then estimated with Equation 3.9.

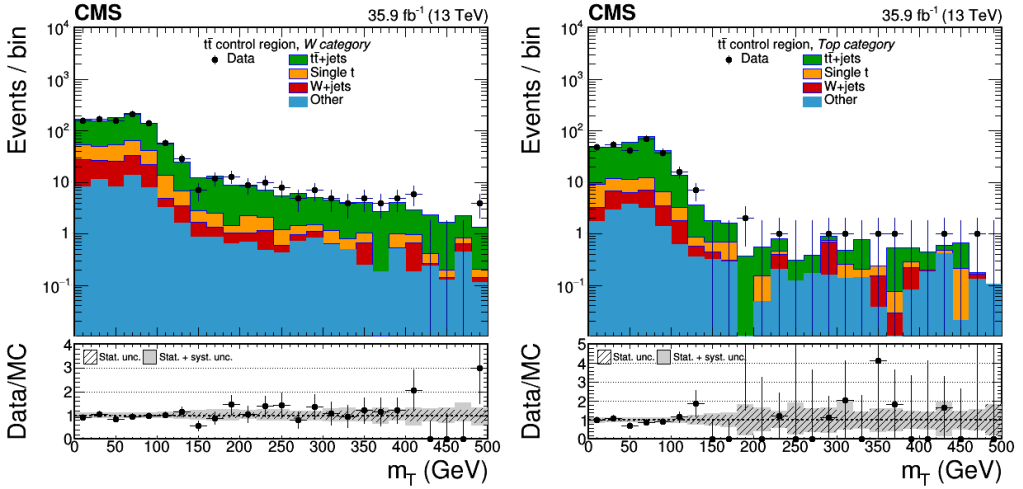


Figure 3.11: $N - 1$ distributions for W transverse mass M_T in the $t\bar{t}$ and single top enriched control region for the W (right) and top (left) categories. The lower panel shows the ratio of events between Data and simulation together with the uncertainties on the MC prediction.

3.6.3 $W(\rightarrow l\nu)+\text{jets}$

The estimation of the $W(\rightarrow l\nu)+\text{jets}$ background is very similar to that of the single top and $t\bar{t}$ processes. It includes the selection of exactly 1 loose electron or muon, and the $M_T < 100$ GeV cut. Additionally, a lower $M_T \geq 30$ GeV cut is added in order to reduce the multijet contribution. One of the differences, however, is that the b quarks are vetoed both for AK4 jets and AK8 subjets. The other main difference to the previous background is that the tagged boosted W or top is not real, because the W boson decays leptonically and the additional jets in the event can form an AK8 jet with high enough p_T that can be mistagged. In order to increase the number of events in this control region, no cut on the N -subjettiness (τ_{21} and τ_{32}) is required.

The full selection is then:

- baseline selection;

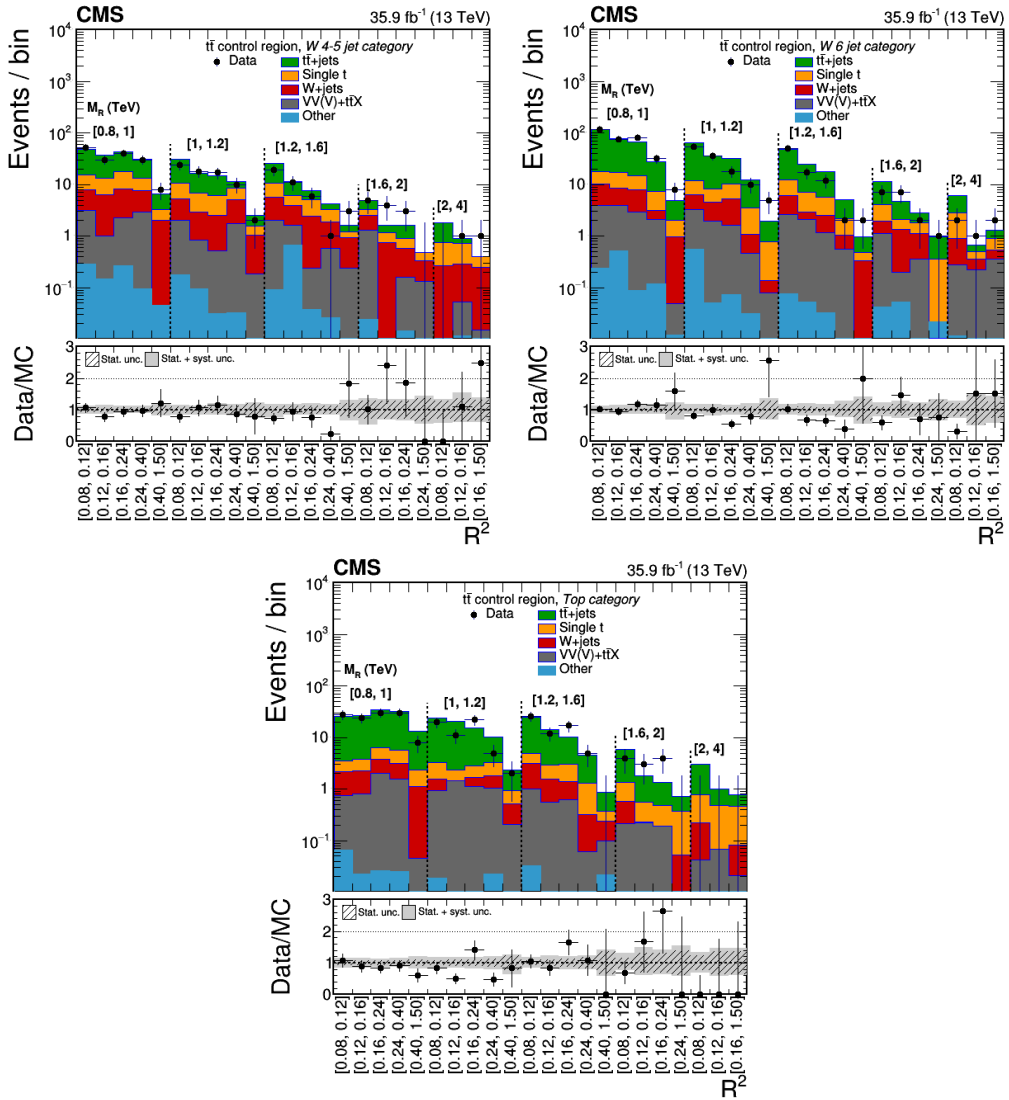


Figure 3.12: The distribution of events in the unrolled razor bins for the W 4–5 jet (top left), W $6 \leq$ jet (top right) and top (bottom) categories in the $t\bar{t}$ and single top control region.

- = 1 loose electron or muon;
- W category: 0 loose b jet and ≥ 1 W mass-tagged AK8 jet;
- top category: 0 loose b jet and ≥ 1 top mass-tagged AK8 jet (also veto on subjet b -tag);
- $|\Delta\phi_{megajets}| < 2.8$;
- $30 \text{ GeV} \leq M_T < 100 \text{ GeV}$.

Figure 3.13 shows the N-1 distributions for the loose b -tags and the W transverse mass, M_T .

Figure 3.14 shows the distribution of events in the unrolled M_R - R^2 bins for the three event categories. These regions contain $W(\rightarrow l\nu)$ +jets events with at least 80% purity. The corresponding contribution to the total background in the signal region is estimated with Equation 3.9.

3.6.4 Multijet

A control region enriched in QCD multijet events is obtained by inverting three selections: the b -tag requirement (for both AK4 jets and AK8 subjets), the N-subjettiness requirement of the mass-tagged jet (or “anti-tagged” in short) and finally the $|\Delta\phi_{megajets}|$ cut.

The full selection is then:

- baseline selection;
- 0 loose leptons;
- W category: 0 loose b jet and ≥ 1 W anti-tagged AK8 jet;
- top category: 0 loose b jet and ≥ 1 top anti-tagged AK8 jet (also veto on subjet b -tag);
- $|\Delta\phi_{megajets}| \geq 2.8$;

The obtained region is more than 90% pure in multijet events. The N-1

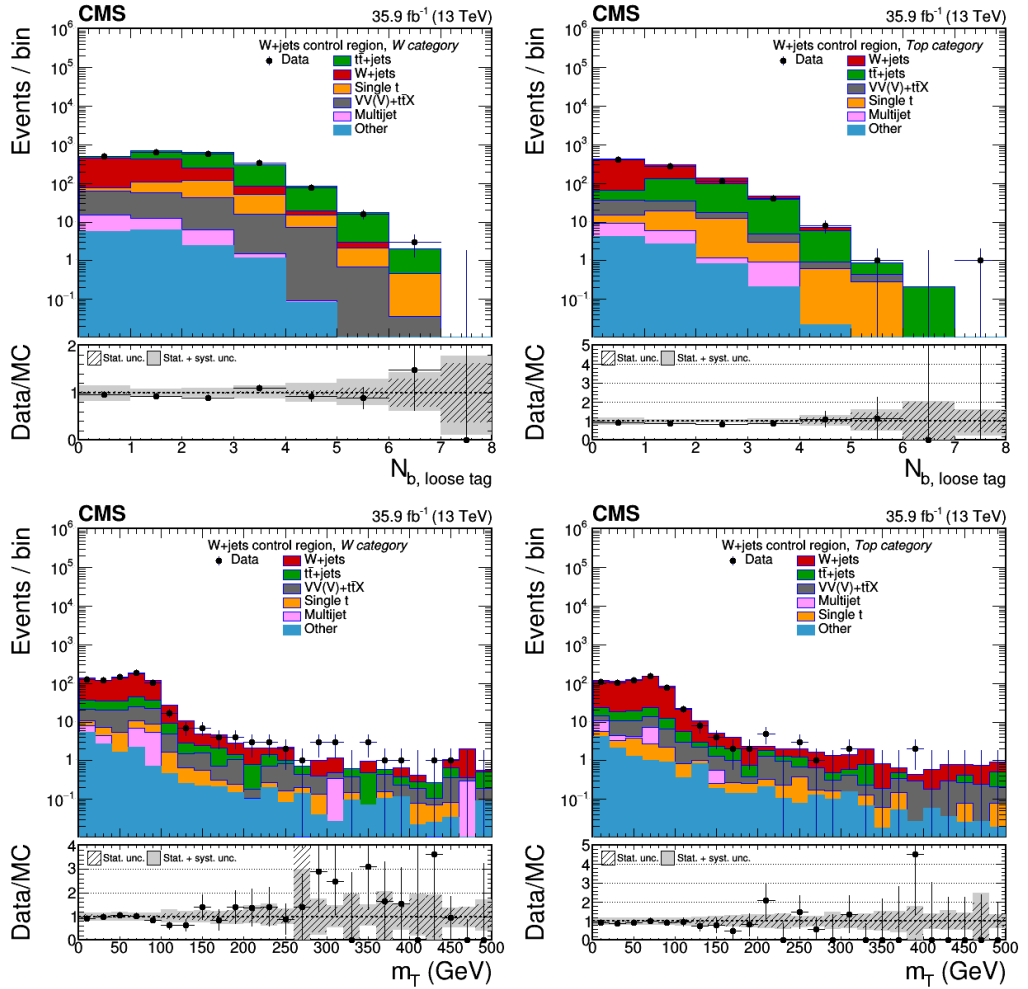


Figure 3.13: The $N-1$ loose b -tag (top) and M_T (bottom) distributions for the W (left) and top (right) event categories in the W +jets control region.

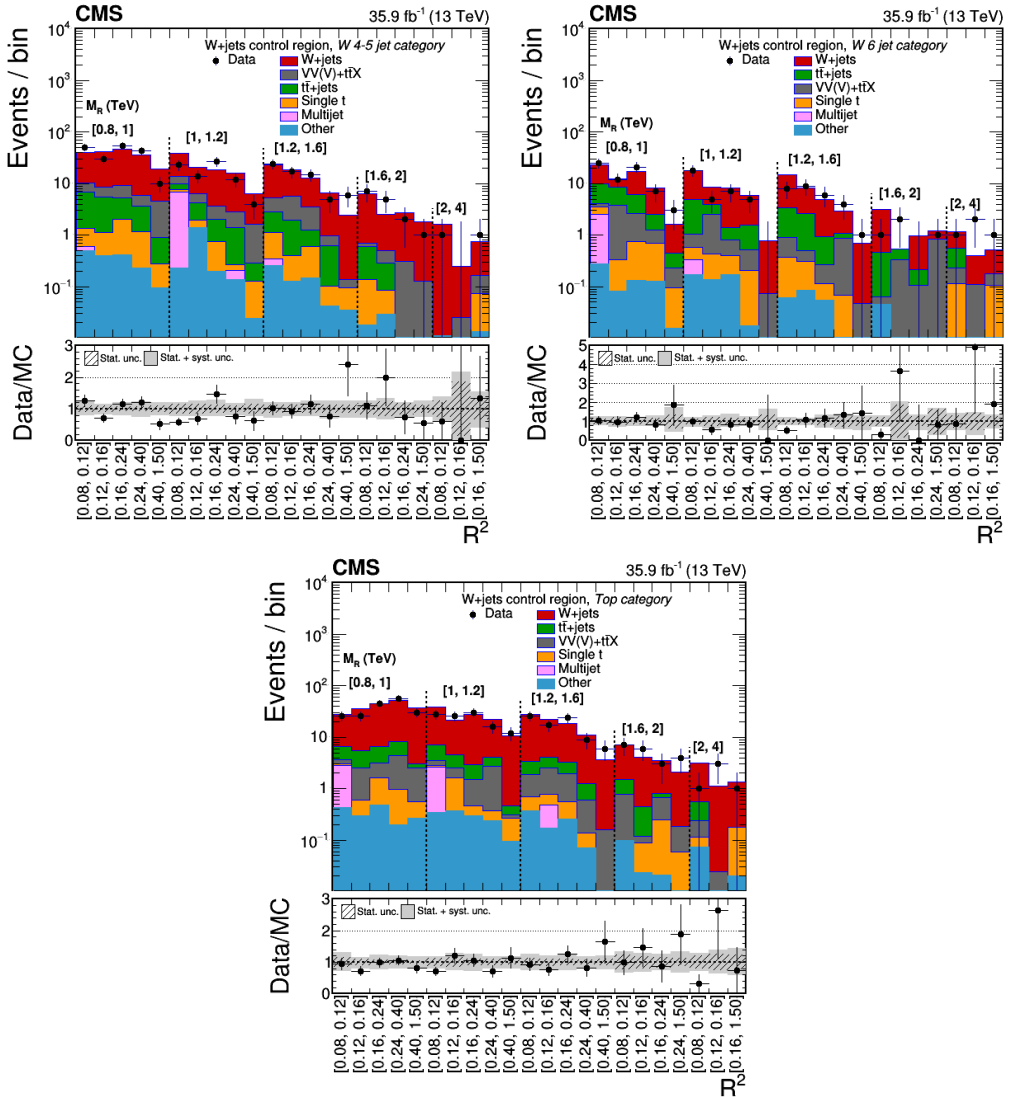


Figure 3.14: The distribution of events in the unrolled razor bins for the W 4-5 jet (top left), W $6 \leq \text{jet}$ (top right) and top (bottom) categories in the $W(\rightarrow l\nu)+\text{jets}$ control region.

distributions for the variables corresponding to the reverted selections are shown in Figure 3.15.

Similar to the previous processes, the multijet contribution to the total background in the signal region is also estimated with Equation 3.9.

3.6.5 $Z(\nu\nu)+\text{jets}$

There is no selection similar enough to the signal region that can isolate with sufficient purity the invisible decay of the Z boson. Attempts to create such a control region were seen to include significant multijet and lost lepton $W(\rightarrow l\nu)$ events which can be very similar. However, there are processes with comparable event kinematics to $Z(\rightarrow \nu\nu)+\text{jets}$, that can be used to estimate the signal region contribution. The $\gamma+\text{jets}$, $Z(\rightarrow ll)+\text{jets}$ and $W(\rightarrow l\nu)+\text{jets}$ processes all show very similar kinematics to that of the invisible Z boson decay; therefore, control regions enriched in these processes were used to model the razor kinematics. One of the crucial ingredients to this procedure was that the non-jet objects, including the γ and the lepton(s), were removed from the event and their four-momenta was added to the missing transverse momentum for the calculation of R^2 . The main estimate was derived from a photon enriched region and normalized by using a $Z(\rightarrow ll)+\text{jets}$ control region. Finally, a cross check of the estimate was done by using a $W(\rightarrow l\nu)+\text{jets}$ enriched control region.

Main estimate using $\gamma+\text{jets}$ and $Z(\rightarrow ll) + \text{jets}$ control regions

A photon enriched control region was defined using the following selection:

- = 1 photon (where \vec{p}_T^γ was added to the \vec{p}_T^{miss});
- baseline selection (including modified Razor variables);

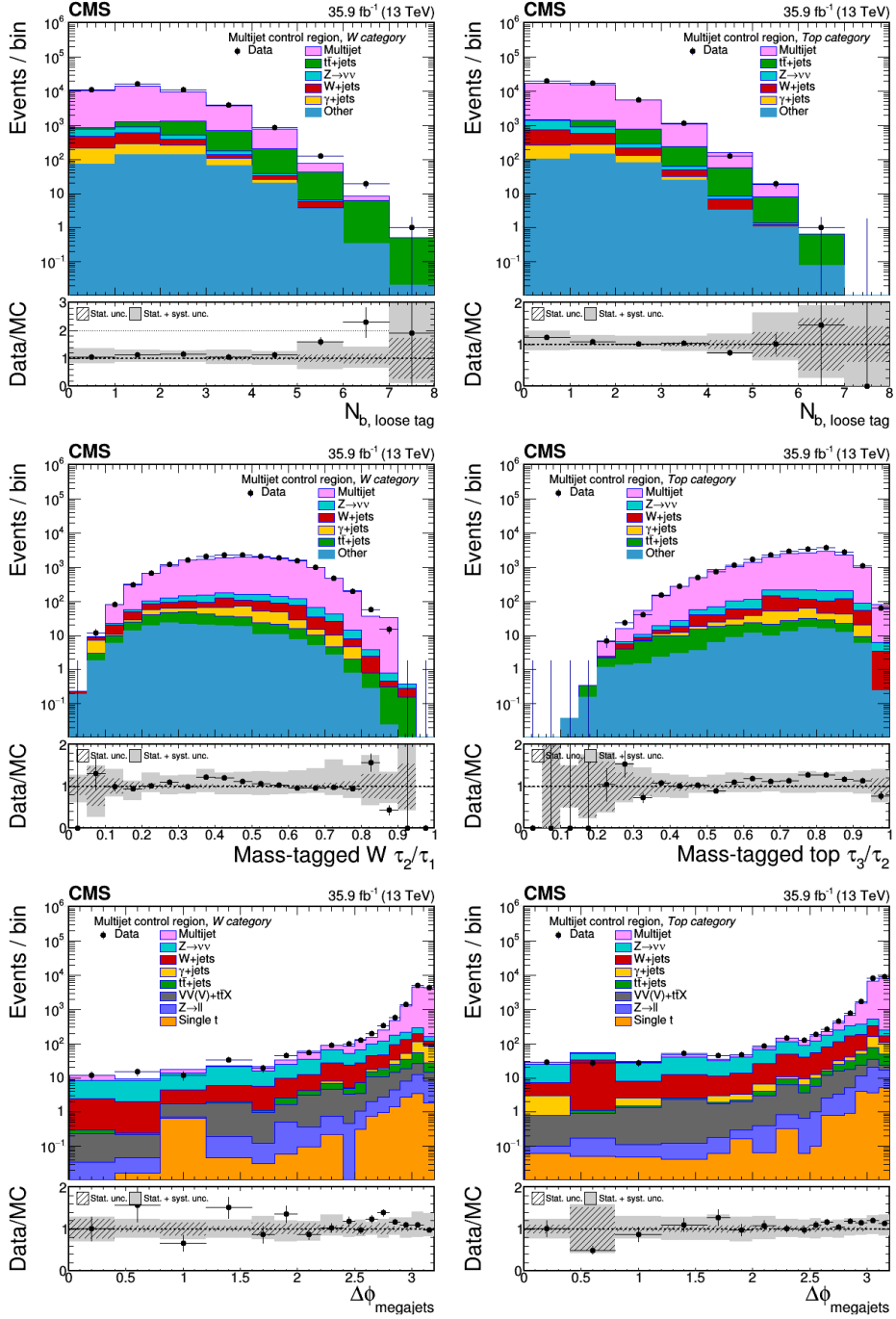


Figure 3.15: The $N-1$ distributions for loose b -tags (top) N -subjettiness (middle) and $|\Delta\phi_{megajets}|$ (bottom) for the W (left) and top (right) event categories in the multijet control region.

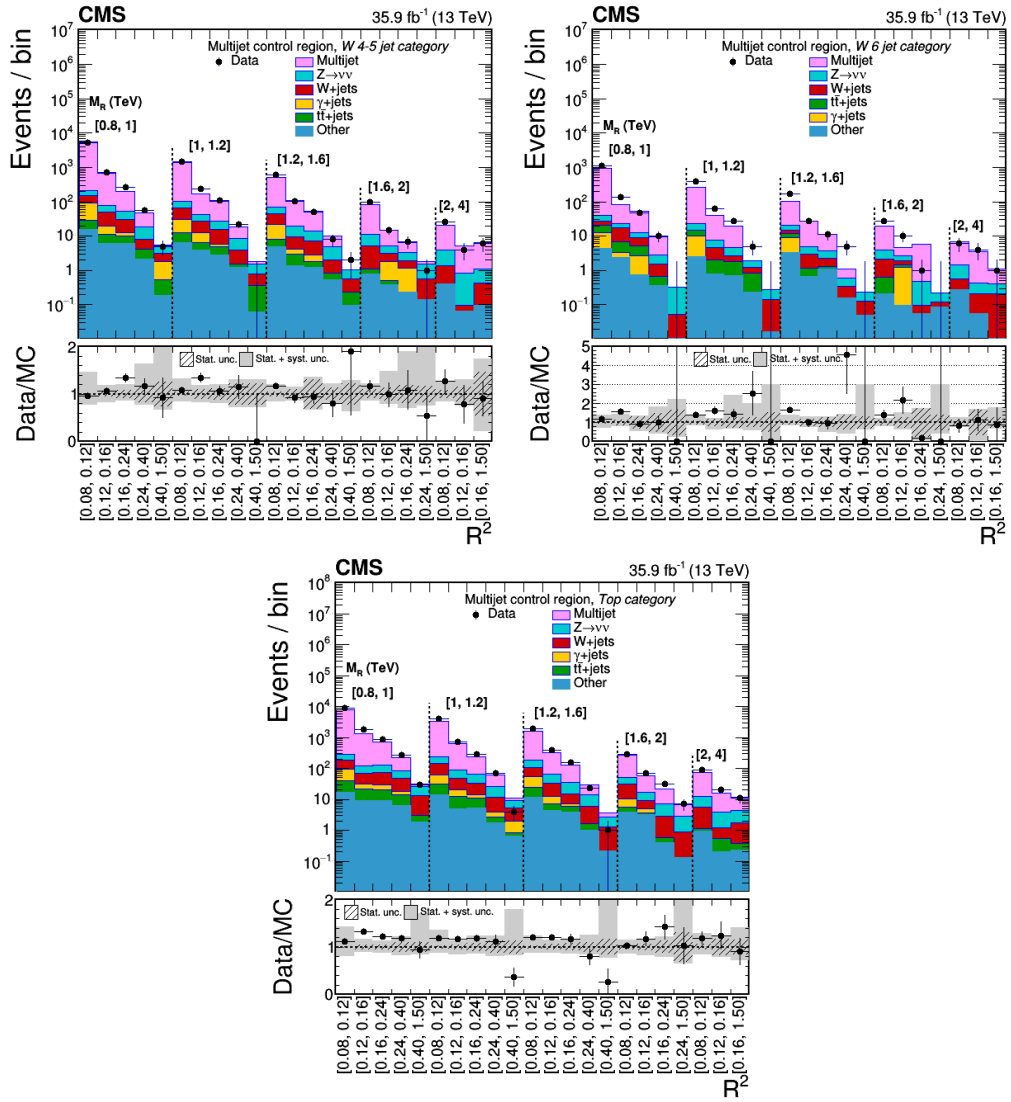


Figure 3.16: The distribution of events in the unrolled razor bins for the W 4–5 jet (top left), W $6 \leq$ jet (top right) and top (bottom) categories in the multijet control region.

- 0 loose lepton;
- W category: ≥ 1 W mass-tagged AK8 jet;
- top category: ≥ 1 top mass-tagged AK8 jet (no b -subjet requirement);
- $|\Delta\phi_{megajets}| < 2.8$ (calculated from modified megajets).

The probability for the photon to be clustered in a jet with other soft (low p_T) hadrons is very high and due to the large transverse momentum ($p_T^\gamma \geq 80$ GeV) they tend to provide most of the jet energy. Therefore these jets are also removed and are not merged into the megajets if they satisfy $0.5 \geq p_T^\gamma/p_T^{jet} < 2.0$. This ratio was already shown in Figure 3.6. The slightly wide range allows to account for the possible differences between the energy reconstruction of photons and jets without removing high p_T jets which would otherwise overlap with the photon. The distribution of events in the photon enriched control region is shown in Figure 3.17.

The purity of this region is less than that of the other control regions, it is only around $> 70\%$. Due to the difference of the process between the signal- and control region, Equation 3.9 cannot be used. Instead the following formula was used:

$$N_{i, SR}^{Est, Z(\nu\nu)} = N_{j, \gamma CR}^{data} \cdot P_\gamma \cdot f \cdot R^{data/MC} \left(\frac{N_{Z(ll) CR}^{Z(ll)}}{N_{\gamma CR}^\gamma} \right) \frac{N_{i, SR}^{MC, Z(\nu\nu)}}{N_{j, \gamma CR}^{MC, \gamma}} \quad (3.9)$$

where P_γ and f are the photon purity and non-fragmentation photon fraction described below. $R^{data/MC}$ is a normalization factor, known as the double ratio, based on the $Z \rightarrow ll$ control region which is introduced later in this section. Finally, the last term is a MC transfer factor between the control and the signal region.

Due to the lower purity of this region, the subtraction of the other background contributions, which is mainly multijet, is less reliable based on the

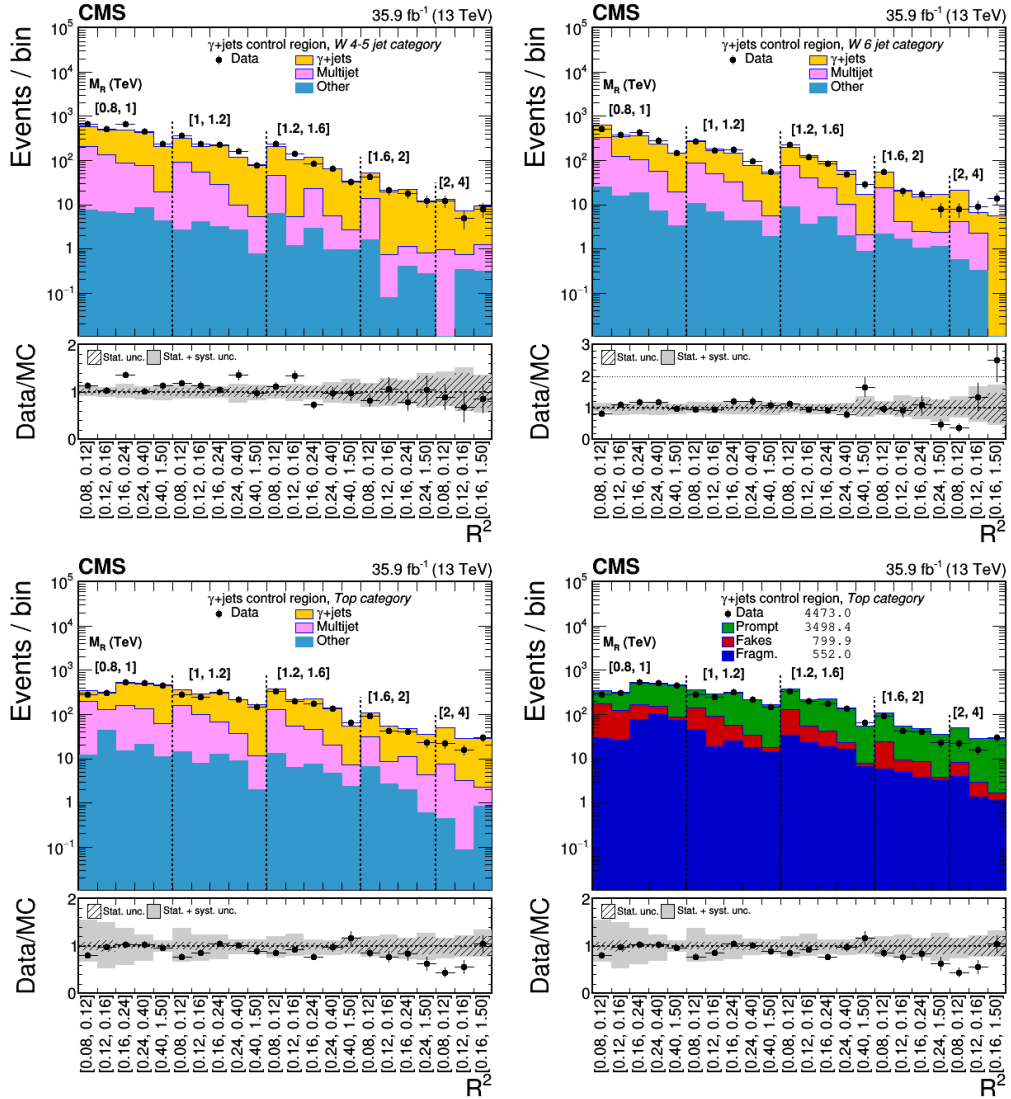


Figure 3.17: The distribution of events in the unrolled razor bins for the W 4-5 jet (top left), W $6 \leq$ jet (top right) and top (bottom) categories in the γ +jets enriched control region. The bottom right plot shows the prompt (photons originating from the hard interaction), fragmentation and fake photons in the top event category.

simulation. Therefore, the measurement of the photon purity was done using a data-driven template fit to the photon charged isolation distributions. The fraction of background events was measured for all M_R and R^2 bins separately. Figure 3.18 shows an example of these measurements. After the subtraction of the multijet background, the fraction of fragmentation photons which do not originate from the hard process was estimated using the simulation. The reason for subtracting these photons is because there is no similar production mode for the Z +jets; so, in order to remain kinematically similar to the $Z \rightarrow \nu\nu$ process, only the photons originating from the hard proton-proton interaction are considered.

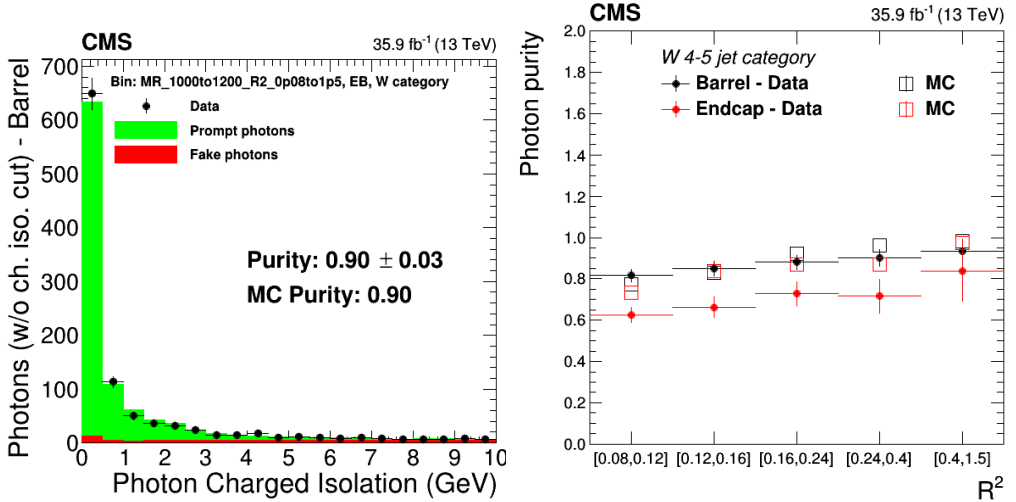


Figure 3.18: An example template fit to the data for the $M_R \in [1000, 1200]$ GeV bin in the barrel region of the electromagnetic calorimeter (left) and the results of all measurements in the R^2 bins (right) for the W 4–5 jet category.

The systematic uncertainty associated to the purity measurement and the non-fragmentation photon fraction is 10% each as a conservative estimate.

The $Z(\rightarrow ll)$ +jets process is very similar to $Z(\rightarrow \nu\nu)$ +jets. Also, both of them are based on the same generator which have leading order precision.

The double ratio, $R^{data/MC} \left(\frac{N_{Z(\ell)}^{Z(\ell)} CR}{N_{\gamma}^{\gamma} CR} \right)$ is suitable to correct for any possible differences between the modeling of the γ +jets and Z +jets processes, for example due to differences in cross section or object reconstruction and identification efficiencies which are not fully accounted for. The $Z(\rightarrow \ell\ell)$ +jets control region was defined with the following event selection:

- = 2 medium electron or muon with opposite charge (where \vec{p}_T^j was added to the \vec{p}_T^{miss} for both)
- baseline selection (including modified Razor variables, due to p_T^{miss});
- W category: ≥ 1 W mass-tagged AK8 jet;
- top category: ≥ 1 top mass-tagged AK8 jet (no b -subjet requirement);
- $|\Delta\phi_{mega,jets}| < 2.8$;
- $|M_{\ell\ell} - M_Z| < 10$ GeV.

Figure 3.19 shows the resulting control regions in inclusive bins of M_R and R^2 . It is more than 80% pure in $\gamma^*/Z(\rightarrow \ell\ell) + jets$ (Drell-Yan) events, but the number of events is too few to allow to derive a bin-by-bin normalization factor with good enough statistical precision. Instead, the double ratio is calculated which is defined as:

$$R^{data/MC} \equiv \frac{k_{Z(\ell)}}{k_{\gamma}} = \frac{N_{Z(\ell)}^{Data} / N_{Z(\ell)}^{MC}}{N_{\gamma}^{Data} / N_{\gamma}^{MC}}. \quad (3.10)$$

Where, the number of events denoted by N are the pure (other background subtracted) event count for the main process of each control region. The background subtraction is data-driven for the γ +jets region and is based on MC for the other. The resulting double ratios and uncertainties are as follows:

- W 4–5 jet category: $1.02 \pm 0.10(stat) \pm 0.29(sys)$;
- W $6 \leq$ jet category: $1.69 \pm 0.17(stat) \pm 0.49(sys)$;

- Top category: $0.91 \pm 0.10(stat) \pm 0.17(sys)$.

The systematic errors are estimated from the size of the observed Data-MC disagreements seen in Figure 3.19.

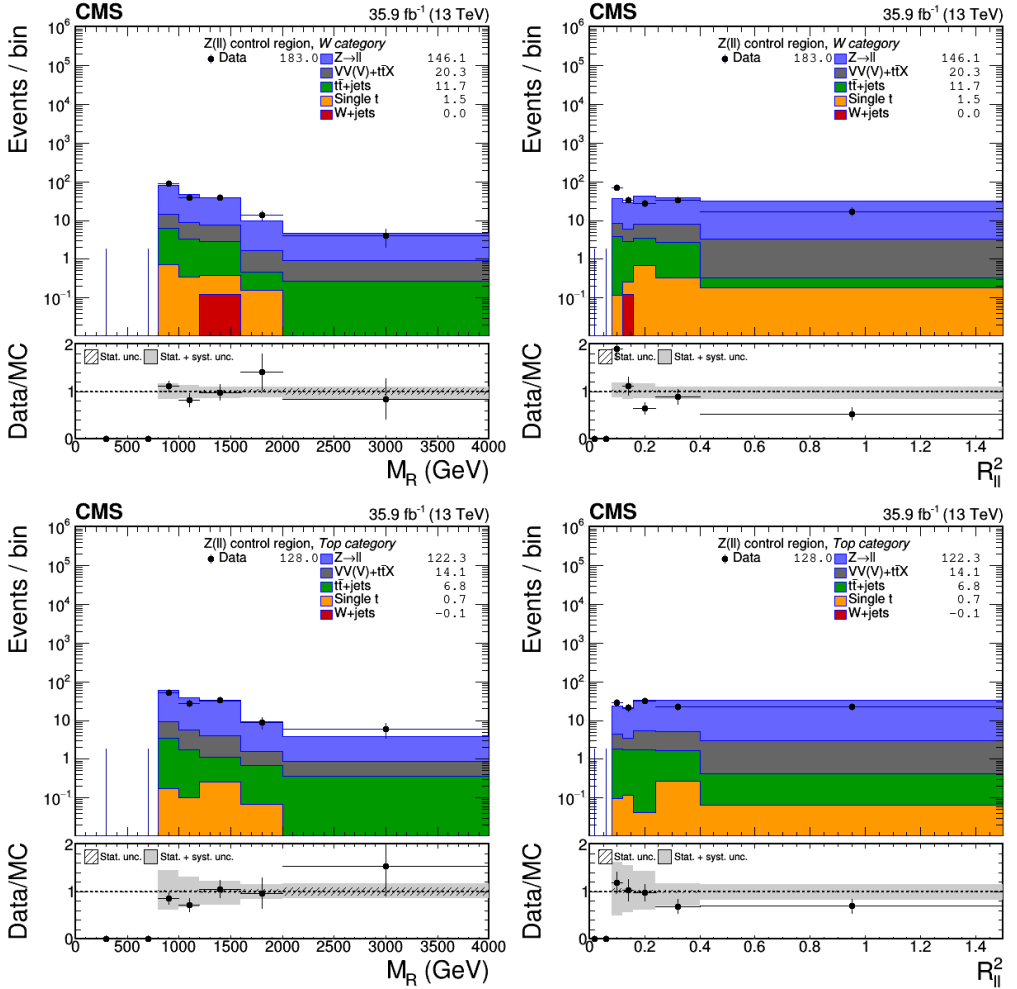


Figure 3.19: Distributions of events in inclusive bins of M_R (left) and R_{ll}^2 (right) in the $Z(\rightarrow ll) + jets$ control region for the W (top) and top (bottom) categories.

Cross-check with a $W(\rightarrow l\nu) + jets$ control region

The control region defined for the validation of the $Z(\rightarrow \nu\nu)+jets$ estimate is exactly the same as the $W(\rightarrow l\nu)+jets$ control region, defined in Section 3.6.3, except that the transverse momentum of the lepton in the event is added to the \vec{p}_T^{miss} , similar to the procedure with the previous control region, which modifies the cut on the R^2 value for the baseline selection. The value of the transverse mass, M_T was kept unchanged in order not to bias the W selection. Figure 3.20 show the distribution of events in the Razor bins in the “one lepton invisible” region which is more than 85% pure in $W(\rightarrow l\nu)+jets$ events.

The following, modified version of Equation 3.9 is used for the $Z \rightarrow \nu\nu+jets$ estimate:

$$N_{i, SR}^{Est, Z(\nu\nu)} = \left(N_{j, 1\ lep\ inv}^{data} - N_{j, 1\ lep\ inv}^{MC, not\ W(l\nu)} \right) \cdot \frac{N_{i, SR}^{MC, Z(\nu\nu)}}{N_{j, 1\ lep\ inv}^{MC, W(l\nu)}}. \quad (3.11)$$

The results of the main estimate is shown with black in Figure 3.21 together with the one lepton invisible region based. There is a good agreement between the two. The main estimate is used as the central value, while the bin-by-bin difference with the other is used as a systematic uncertainty.

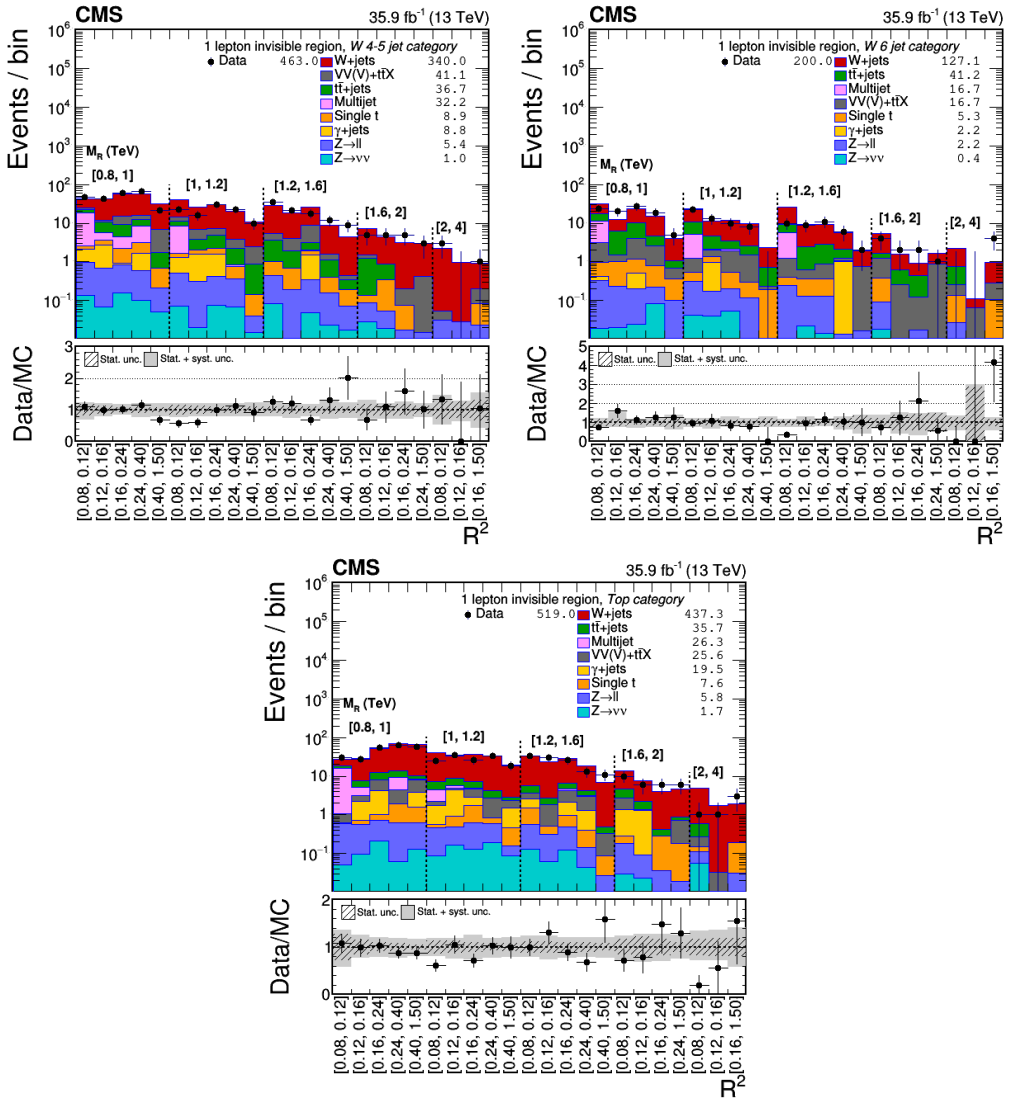


Figure 3.20: The distribution of events in the unrolled razor bins for the W 4-5 jet (top left), W $6 \leq$ jet (top right) and top (bottom) categories in the one lepton invisible control region.

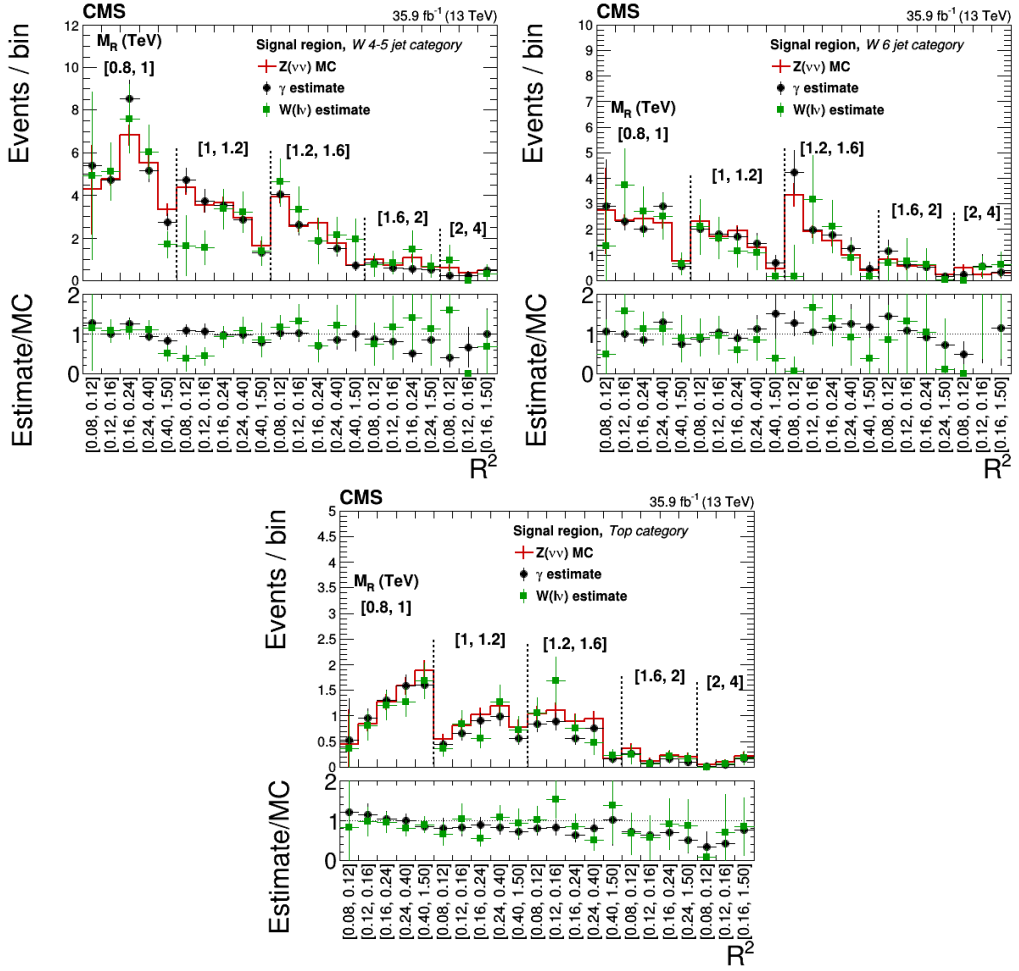


Figure 3.21: The estimated $Z(\rightarrow \nu\nu)+$ jets background contribution in the signal region from the $\gamma+$ jets and $Z(\rightarrow ll)+$ jets control regions and the one lepton invisible control region as a comparison with the direct MC simulation for the W 4–5 jet (top left), W $6 \leq$ jet (top right) and top (bottom) categories.

3.6.6 Validation of the background estimation

The sum of the total background is estimated with the following final formula:

$$\begin{aligned}
N_{i, SR}^{Est} = & \left[\left(N_{j, Multijet CR}^{data} - N_{j, Multijet CR}^{MC, not Multijet} \right) \cdot \frac{N_{i, SR}^{MC, Multijet}}{N_{j, Multijet CR}^{MC, Multijet}} \right] \quad (3.12) \\
& + \left[\left(N_{k, t\bar{t}/single t CR}^{data} - N_{k, t\bar{t}/single t CR}^{MC, not t\bar{t}/single t} \right) \cdot \frac{N_{i, SR}^{MC, t\bar{t}/single t}}{N_{k, t\bar{t}/single t CR}^{MC, t\bar{t}/single t}} \right] \\
& + \left[\left(N_{l, W(l\nu) CR}^{data} - N_{l, W(l\nu) CR}^{MC, not W(l\nu)} \right) \cdot \frac{N_{i, SR}^{MC, W(l\nu)}}{N_{l, W(l\nu) CR}^{MC, W(l\nu)}} \right] \\
& + \left[N_{l, \gamma CR}^{data} \cdot P_{\gamma} \cdot f \cdot R^{data/MC} \left(\frac{N_{Z(ll) CR}^{Z(ll)}}{N_{\gamma CR}^{\gamma}} \right) \cdot \frac{N_{i, SR}^{MC, Z(\nu\nu)}}{N_{l, \gamma CR}^{MC, \gamma}} \right] \\
& + N_{i, SR}^{other MCs}.
\end{aligned}$$

In order to validate the procedure, we replace the signal region selection with two very similar (but signal depleted) selections and check the validity of the estimate which should give bin-by-bin results that have a reasonably good accuracy.

The first, signal-like validation region is defined by reverting the $\Delta\phi_{megajets}$ cut of the signal region (Section 3.5.3) and keeping the rest of the selections the same. The second, multijet validation region is defined also by reverting the $\Delta\phi_{megajets}$ cut but for the multijet region defined in Section 3.6.4. These two closure tests are suitable to test the validity of the modeling for both b tagging and vetoing, some aspects of the top and W tagging and the $\Delta\phi_{megajets}$ modeling of all background types.

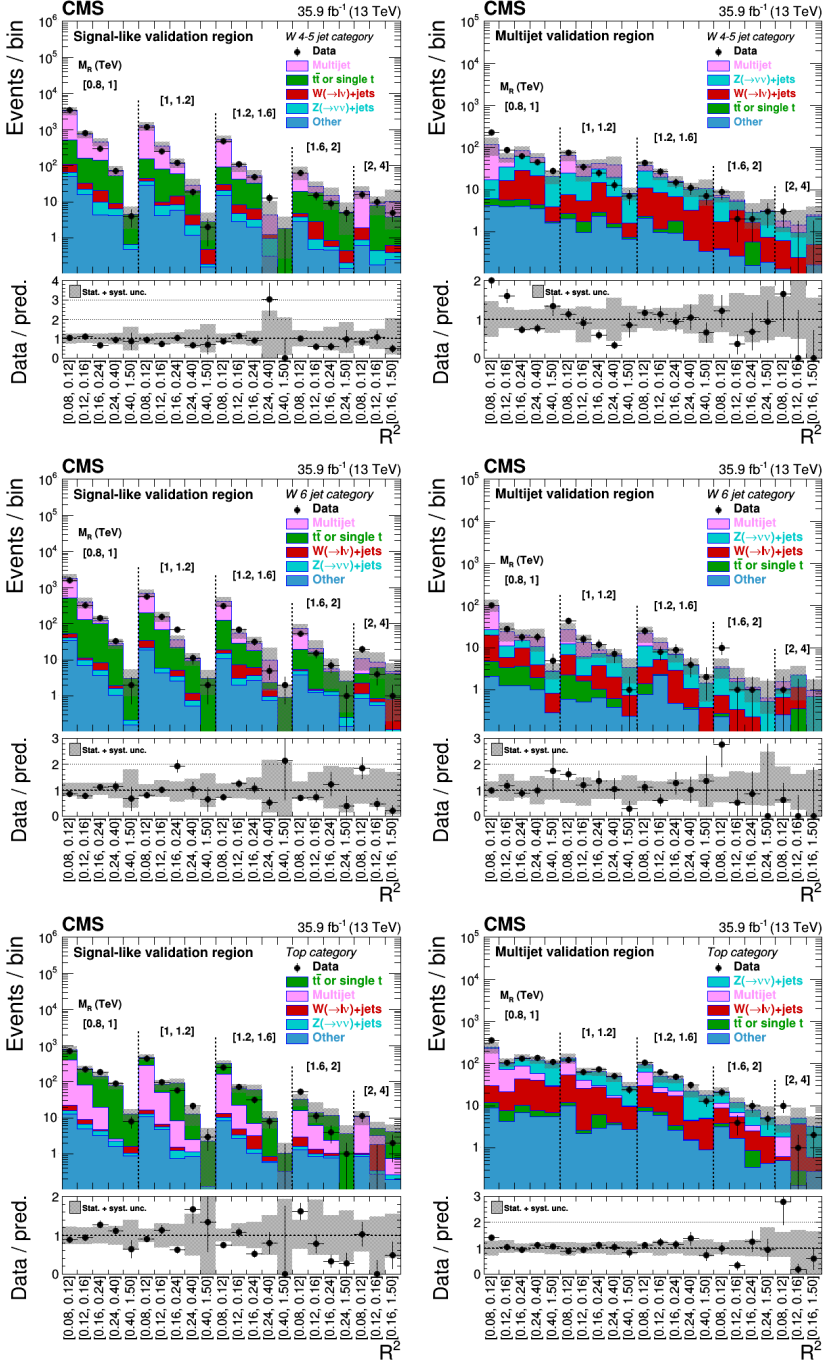


Figure 3.22: Background estimation closure test results in the signal-like (left) and multijet (right) validation regions for the W 4-5 jet (top), W 6 \leq jet (middle) and top (bottom) categories. Data/prediction ratio is shown in the lower panels, where the gray band is the total (systematic and statistical) uncertainty on the prediction.

3.7 Systematic Uncertainties and Corrections

This section details the various systematic uncertainties that are taken into account.

3.7.1 Theory uncertainties

There are various uncertainties related to the modeling of signal and background processes. One of them originate from the fact that the used models are based on perturbative calculations which involve a truncated expansion. It is then compulsory to estimate the uncertainty due to the omission of the uncalculated terms. The conventional method to estimate this uncertainty is the prescription to vary the factorization and renormalization scales up and down by a factor of two. The variation could be done separately or simultaneously. As a conservative estimate, this analysis used the latter, which was seen to give a larger uncertainty than the former cases. Another type of uncertainty was related to the variation of the QCD coupling parameter, $\alpha_s = 0.118 \pm 0.0015$. Both of these uncertainties were seen to be small.

There are uncertainties related to the modeling of the initial state radiation (ISR) of the signal simulations which are based on `MadGraph`. We impose event reweighting based corrections to the ISR jet multiplicity spectrum. The event weight correction factors vary between 0.92 and 0.51 for one to six ISR jets. The half of the difference to unity is taken as a systematic uncertainty in the correction factors.

The p_T spectrum of the `Powheg` $t\bar{t}$ MC samples are seen to diverge from that observed in data [96]. The measured difference from unity for the observed event ratio is used as a systematic uncertainty on the event weight of $t\bar{t}$ events.

Additional systematic uncertainties were derived for the $Z(\rightarrow \nu\nu)+\text{jets}$ and QCD multijet processes based on Data-MC disagreements observed in the $Z(\rightarrow ll)+\text{jets}$ and multijet control regions. For the latter, the regions derived by removing the b-tagging, $\Delta\phi_{\text{mega}j\text{ets}}$ and N-subjettiness requirements were also considered. The average of the bin-by-bin differences from unity in the Data-MC event count ratio was applied as a flat systematic uncertainty for the two corresponding background estimates.

3.7.2 Jet/MET uncertainties

Calibrations are applied on jets in order to correct for the effects of pile-up, non-uniformity of detector response, residual data-simulation jet energy scale differences and jet flavor [97]. Additional corrections are applied on the simulation to match the jet energy resolution observed in data. The associated uncertainties of these corrections are propagated to both the jets and all quantities derived from them, including the missing transverse momentum and the razor variables.

Despite the above corrections, it was observed that the high end of the jet p_T spectrum of AK8 jets was not well modeled for the $\gamma/Z/Z^*+\text{jets}$ processes, therefore a correction was applied to the AK8 jet energy based on a control region similar to the $Z(\rightarrow ll)+\text{jets}$ defined in Section 3.6.5 which does not include the mass-tagged object requirement (Z-1 region in short). The data-MC comparison for this region is shown in Figure 3.23. A scale correction was applied which was seen to improve the data-MC agreement for all $Drell - Yan$ and $\gamma+\text{jets}$ dominant regions. The result of the correction is shown in Figure 3.24 for the $\gamma+\text{jets}$ control region for the W event category. The uncertainties on the scale correction parameters

were applied as a systematic.

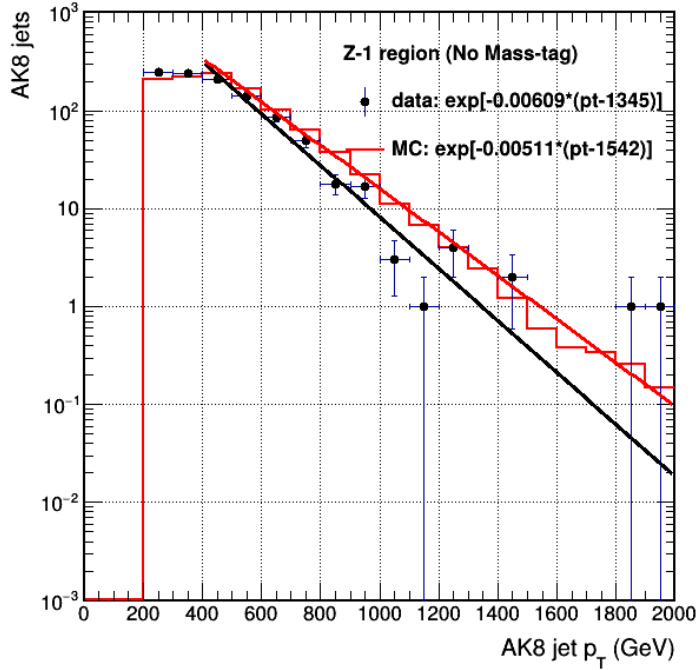


Figure 3.23: Exponential fits to the to AK8 jet p_T distribution in Z-1 region to data and MC. The ratio of the fits was used as a jet energy correction factor for $\gamma/Z/Z * +jets$ simulation samples.

3.7.3 $b/W/top$ tagging

b tagging

Corrections were applied in simulation to the b tagging and mistagging efficiencies of AK4 jets originating from bottom, charm, light quarks ($u/d/s$) and gluons for both Full- and FastSim in order to match the same efficiencies measured in data. The corrections are applied event-by-event with scale factors, which were provided by the CMS b -tagging POG, which correct the event weight based on the generator level flavor of each jet. The size of the

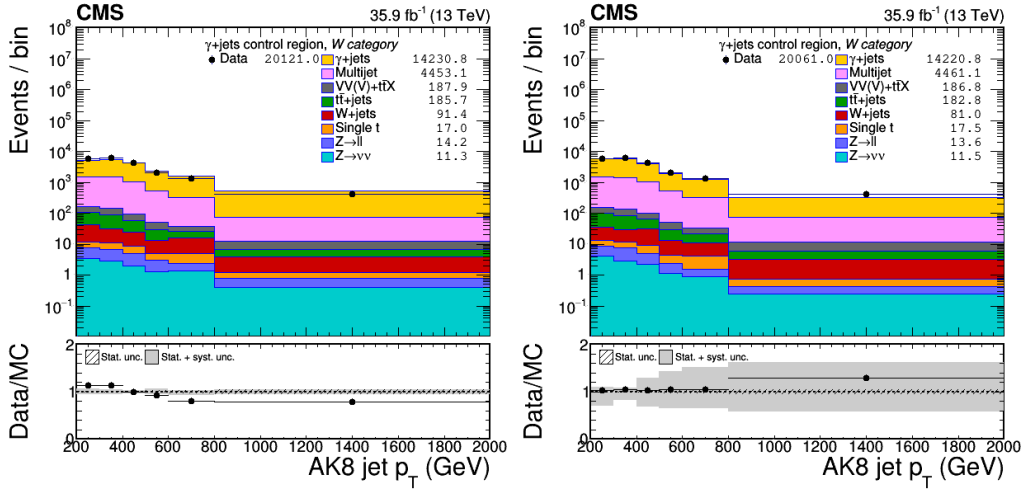


Figure 3.24: The AK8 jet p_T spectrum in the γ +jets control region observed before and after the AK8 jet energy correction for the W event category.

corrections range from 1–7% and 2–20% for tagging and mistagging, respectively. The statistical and systematic uncertainties on the scale factors are below 4%.

W and top tagging

W - and top tagging efficiency scale factors, which are provided by the CMS JetMET POG, are used to correct the Full- and FastSim samples similar to the procedure of b -tagged jets. AK8 jets which are originating from the hadronic decay of W bosons or top quarks are treated separately for the event weight corrections. The sizes of the corrections are 0–4% for W s and 7% for $tops$, and their uncertainties were 6–11% and 4–7%, respectively.

The analysis also uses mistagged W s and $tops$, and also mass- and anti-tagged jets in some of the control regions defined in Section 3.6, which are not originating from real W and top decays. The probability to tag jets as such was measured in a multijet dominant control region, which was

used to derive corrections to the mistagging probability of the simulation by calculating and using so-called “fake rate” scale factors. The size of these corrections, which depends on the p_T and η of the AK8 jets, typically ranges from 3–24% and 5–34% for W s and $tops$, respectively. The statistical and systematic uncertainties are generally below 18% and 16%, but could reach much larger values in low statistics bins. The used scale factor figures are found in Appendix A.

3.7.4 Lepton related uncertainties

The electron reconstruction, identification and isolation efficiencies were corrected in simulation to match that what was measured in data using scale factors, which were derived separately for loose and tight lepton definitions. Similarly, the muon track reconstruction, identification and isolation efficiencies were also corrected. The uncertainties of these correction factors are applied as a systematic. These corrections and uncertainties were provided by another analysis group within CMS.

The above systematic uncertainties and corrections only apply to cases where a lepton was found, therefore the evaluation of the uncertainty related to lost lepton mismodeling was needed. The uncertainty was determined in a control region where the previously mentioned corrections were not applied on purpose in order to measure the differences between data and simulation to determine the size of the discrepancy due to mismodeling. The control region is very similar to the signal region, except that exactly one loose lepton is required without applying the $\Delta\phi_{megajets}$ selection. In order to limit possible signal contamination, an upper cut was applied on the transverse mass, $M_T < 100$ GeV. Figure 3.25 shows the distribution of

p_T and η for the selected lepton in the control region. The observed size of the data-MC disagreement, which ranged from 13–18%, was applied as a systematic uncertainty on the event yield for events where a generator level lepton was present, but was not reconstructed, identified or isolated.

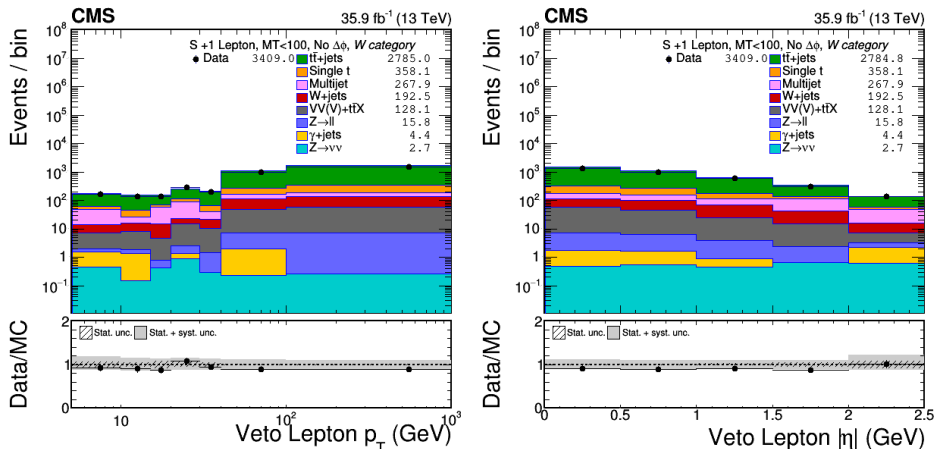


Figure 3.25: Loose lepton p_T (left) and η (right) distributions in the lost lepton control region for the W event category. Data/MC prediction ratios are shown in the lower panels.

3.7.5 Other uncertainties

The uncertainty of the luminosity measurement, which is 2.5%, was measured by the CMS collaboration as described in [98]. The uncertainties of the trigger efficiencies were determined from measurements in data which were described in Section 3.5.2. The measured statistical uncertainties were applied as a systematic uncertainty.

The background simulation was corrected by reweighting to match the distribution of the number of pile-up events determined from data. The number of pile-up events is calculated from instantaneous luminosity measurements by dividing it with the inelastic minimum-bias proton-proton cross

section and the bunch crossing frequency. A conservative choice of 5% was used for the uncertainty of the cross section in the determination of the pileup distribution.

The simulated pile-up distribution was different also for the signal, therefore a correction was performed in order to correct for the difference in the acceptance. The pile-up acceptance corrections and systematics for FastSim were performed with the following procedure:

- The signal region was split to two roughly equal size bins depending on the number of reconstructed vertices (low: < 20 , high: ≥ 20 vertices);
- The relative acceptances ($A_{rel, bin} = A_{bin}/A_{avg.}$) for signal events were calculated for both bins and a linear fit was performed as a function of the average number of vertices in each region;
- The linear fit to the relative acceptance was convoluted with the actual distribution of the number of vertices (normalized to an integral of 1), that is observed from data in a sufficiently loose sample;
- The acceptance correction factor is calculated from the integral of the convoluted function;
- In order to correct for the acceptance difference between data and simulation, due to the different pile-up distributions, the nominal simulated event counts in each bin was multiplied by the above correction factor;
- Finally, the uncertainty of the acceptance correction factor, which was determined from the error of the linear fit, was applied as a systematic uncertainty.

The uncertainties related to extrapolation for empty signal region bins and the $Z(\rightarrow \nu\nu)+\text{jets}$ estimation were already described in Section 3.6.1 and 3.6.5.

3.7.6 Summary of uncertainties

The average bin-by-bin systematic uncertainty of the background estimates are shown for all search regions in Figure 3.26. The various types are categorized as explained in the previous subsections except that the extrapolation uncertainty is shown separately. This alone can dominate in some of the bins, especially for the top event category. The size of the uncertainties varies greatly bin-to-bin and for different event categories. The jet and p_T^{miss} related uncertainties were seen to be the most dominant in the more sensitive bins (i.e. the top event category and/or the high M_{R-R^2} bins).

3.8 Results and Interpretation

The observed data counts in the search regions were statistically compatible with the standard model background prediction. Tables B1, B2 and B3 show the predicted background, selected signal benchmark yields and the observed data counts for all search regions. Figure 3.27 shows the predicted background, observed data counts and benchmark signal yields for all search regions. Additional tables with numerical values can be found in Appendix B. The main source of uncertainty was statistical. It largely originated from the limited number of events available in the data control regions. The precision of the search can be greatly improved with the addition of more data.

Due to the absence of any signal, these results were interpreted as exclusion limits on the parameter space for various SUSY simplified models introduced in Section 3.1; and combined with that of a similar but more inclusive razor analysis within CMS, which excluded the boosted object se-

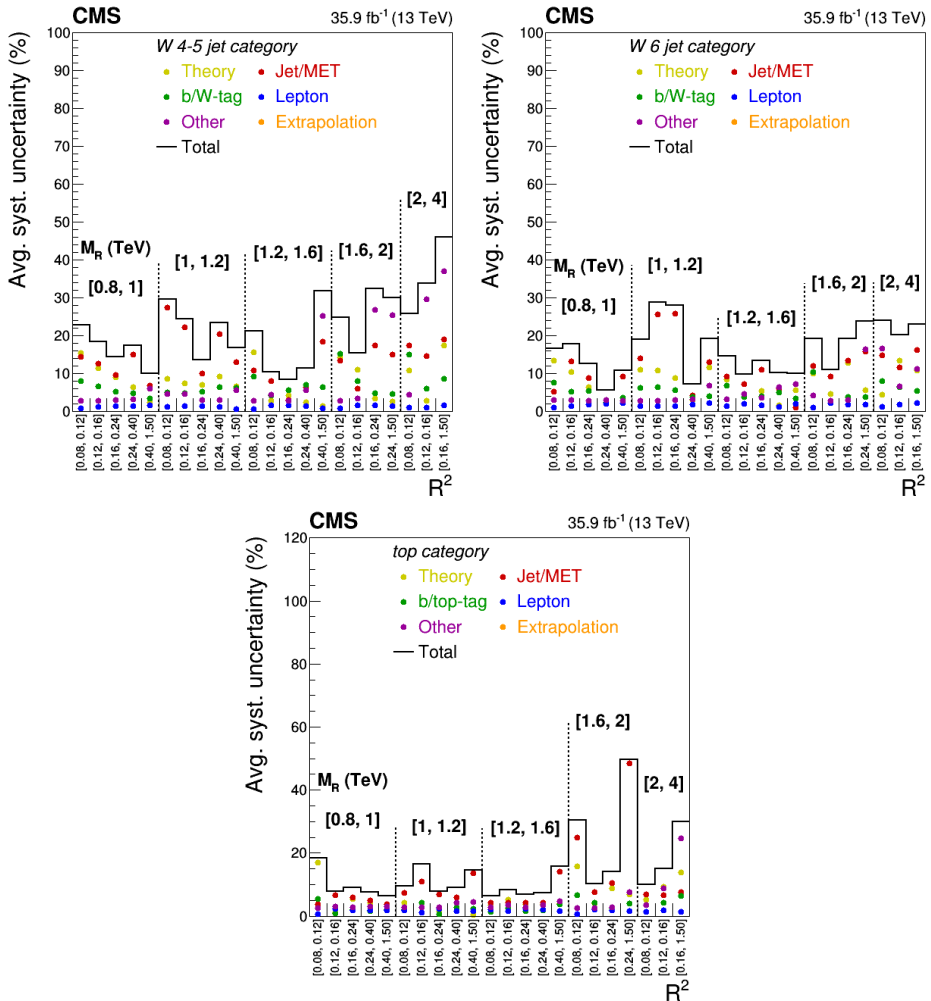


Figure 3.26: The average systematic uncertainty percentages as a function of unrolled M_R - R^2 bins for the W 4–5 jet (top left), $W 6 \leq$ jet (top right) and top (bottom) categories. The various uncertainty sources, which are explained in the previous subsections, are shown with different colors. The total corresponds to all uncertainties added in quadrature.

lection, in order to increase the sensitivity. These results were published together in [105]. The limit setting procedure is based on a simultaneous binned likelihood fit to the observed data in all search regions, which takes into account the predicted SM background and signal yields. The 95% con-

confidence level (CL) upper limits on the SUSY production cross sections are calculated according to the recommended LHC procedure which is based on a modified frequentist approach with the CL_s criterion [99, 100] and uses an asymptotic approximation for the test statistic [101, 102]. The signal model points were considered to be excluded if the gluino and top squark production cross sections, which were calculated with NLO+NLL precision [103], were exceeded by the 95% CL upper limit.

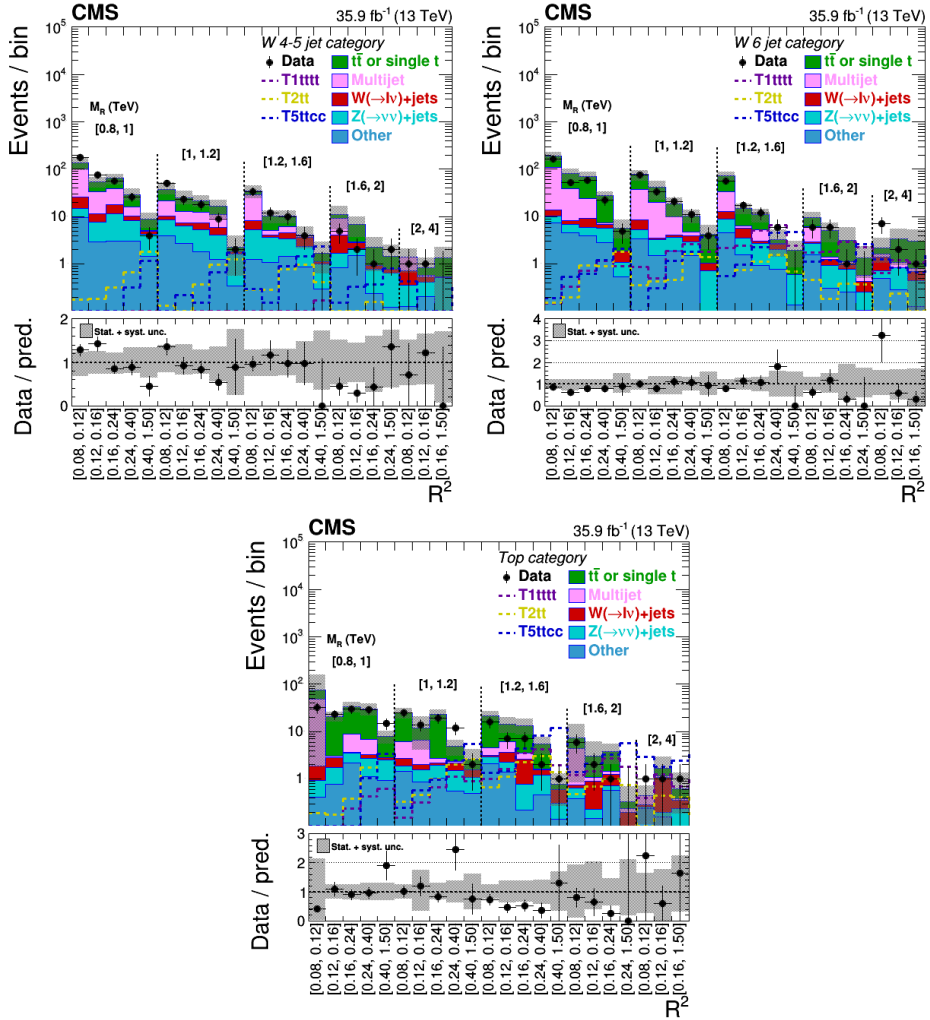


Figure 3.27: The distribution of events for the background prediction and the observed counts in data as a function of unrolled M_R - R^2 bins for the W 4–5 jet (top left), W $6 \leq$ jet (top right) and top (bottom) categories. The background labeled as “Other” is based on the MC prediction for a single top quark, di- and tribosons and associated production of $t\bar{t}$ and a W or Z boson. The shaded region represents the total (statistical and systematic) uncertainty on the background prediction. Additional benchmark signal distributions are shown for the T5ttcc ($m_{\tilde{g}} = 1.4$ TeV, $m_{\tilde{t}} = 320$ GeV and $m_{\tilde{\chi}_1^0} = 300$ GeV), T1tttt ($m_{\tilde{g}} = 1.4$ TeV and $m_{\tilde{\chi}_1^0} = 300$ GeV) and T2tt ($m_{\tilde{t}} = 850$ GeV and $m_{\tilde{\chi}_1^0} = 100$ GeV) simplified models.

The combined exclusion limits, which are shown in Figures 3.28,3.29 and 3.30, indeed gave better limits than what was possible to achieve separately by both analysis. The limits achieved by the non-boosted analysis is shown with the blue contours, and those by this analysis are found in Appendix B. The biggest improvement with the combination came for the low *top* squark mass T5ttcc model, where the *tops* had a higher probability to gain boost compared to the other two models. The combined preliminary results we published [104] improved upon the best, previously observed limits of CMS:

- for the exclusion of the gluino mass by ≈ 100 GeV in the T5ttcc model;
- and by ≈ 20 GeV for the top squark mass in the T2tt model of direct top squark pair production.

The results were also published in the Journal of High Energy Physics [105].

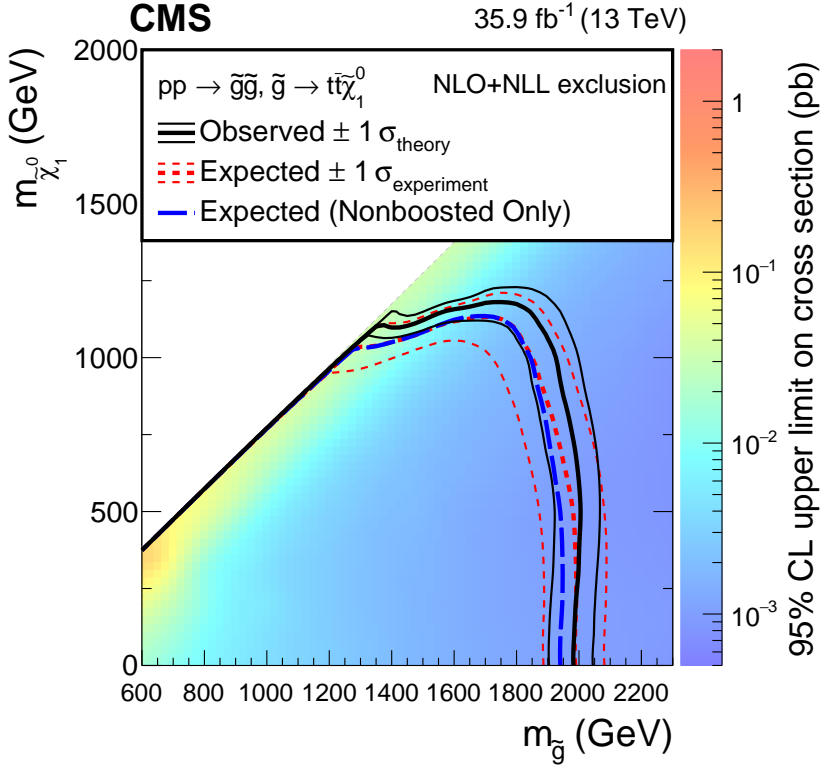


Figure 3.28: 95% CL exclusion limits on the production cross section of gluino pair production where each gluino decays to a neutralino and top quark ($Tt\bar{t}\bar{t}\bar{t}\bar{t}$). The solid black lines show the observed limit from data together with the ± 1 standard deviation contours corresponding to the uncertainties of the NLO+NLL cross section calculations. Similar dashed contours represent the expected limits and the ± 1 standard deviation experimental uncertainties for the combined results (red) and the inclusive non-boosted categories separately (blue).

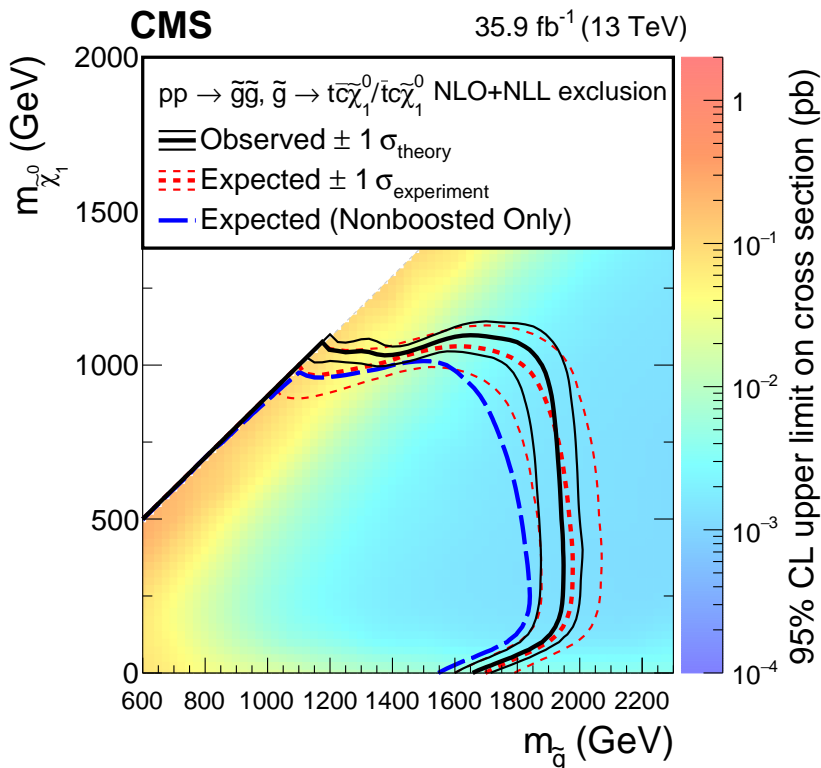


Figure 3.29: 95% CL exclusion limits on the production cross section of gluino pair production where each gluino decays to a top squark and top quark and the former subsequently decays to a neutralino and a charm quark ($T5\tilde{t}tcc$). The mass of the top squark is fixed to be 20 GeV below that of the neutralino. The solid black lines show the observed limit from data together with the ± 1 standard deviation contours corresponding to the uncertainties of the NLO+NLL cross section calculations. Similar dashed contours represent the expected limits and the ± 1 standard deviation experimental uncertainties for the combined results (red) and the inclusive non-boosted categories separately (blue).

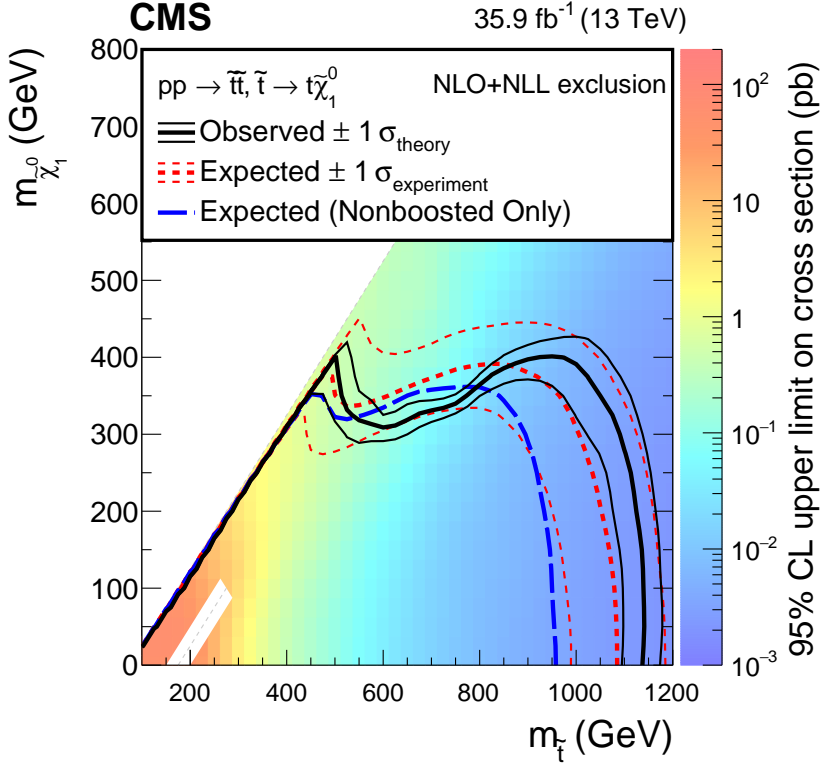


Figure 3.30: 95% CL exclusion limits on the production cross section of pair-produced top squarks each decaying to a neutralino and top quark (T2tt). The solid black lines show the observed limit from data together with the ± 1 standard deviation contours corresponding to the uncertainties of the NLO+NLL cross section calculations. Similar dashed contours represent the expected limits and the ± 1 standard deviation experimental uncertainties for the combined results (red) and the inclusive non-boosted categories separately (blue). The white diagonal band near $m_{\tilde{\chi}_1^0} = 0$ GeV, which is excluded from the plot, corresponds to the region where the difference between the mass of the top squark and the neutralino is very close to the mass of the top quark ($|m_{\tilde{t}} - m_t - m_{\tilde{\chi}_1^0}| < 25$ GeV). The signal acceptance in this region varies greatly with the neutralino mass and is therefore difficult to model.

Acknowledgements

I would like to thank my PhD supervisors, Dr. Viktor Veszprémi and Prof. Dr. Zoltán Trócsányi for their invaluable guidance and support during my studies and in the preparation of my PhD Thesis.

I would like to also thank Danek Kotlinski and Gino Bolla (†) who gave very helpful advice during my work with the pixel detector.

I would like to thank Petar Maksimovic in the formulation of the search strategy and Sezen Sekmen for her unending guidance in bringing the Supersymmetry analysis to completion.

I would like to thank all of my colleagues and lecturers who helped me to gain the knowledge that is required in the challenging field of particle physics.

I wish to thank the Hungarian Scientific Research Fund (OTKA NK 81447, K 109803, K 124850) and the SCOPES 2013-2016 Joint Research Project of the Swiss National Science Foundation for their financial support of my work.

Finally, I would like to thank my family for their relentless support during my journey in the field of experimental physics.

Summary

In the first part of my PhD studies, I was responsible for the coordination of offline calibrations and reconstruction of the CMS pixel detector and the monitoring of its performance. This includes hit efficiency measurements and studying the signals deposited on the detector (clusters) by traversing charged particles.

The second part of my studies involved the search for new particles predicted by the supersymmetric extension of the Standard Model. Up until now no evidence of new particles beyond the Standard Model were found in the LHC. In their most cited papers, the two largest LHC experiments, CMS and ATLAS, both gave exclusions of supersymmetric particle masses beyond the TeV scale. These searches typically looked for large jet multiplicity, b-tagged jets and significant amount of missing transverse energy. Most of these LHC searches use so-called simplified models which consider only a few particles to be light. These models are described by effective Lagrangians with a small number of free parameters. These are usually the masses of particles, branching fractions and production cross-sections. This framework was used to construct analyses that are sensitive to a wide range or more specific SUSY signatures.

In 2012, I participated in one of the Run 1 SUSY searches [10]. In this study I contributed to the determination of systematic uncertainties related to the single lepton identification, reconstruction and data collection efficiencies. The Run 1 data allowed us to exclude the existence of gluinos

above 1.1 TeV in some scenarios. In Run 2, the almost doubled collision energy and the increased luminosity motivated me to pursue the search further with a more specialized approach. The models of our interest were the ones where a pair of heavy gluinos or stops are produced each of which decay to various standard model particles and the weakly interacting LSP. The latter are undetected and cause a large fraction of the momentum to be missing. In these simplified models, the parameters of interest reduce down to the masses of the mother particles (gluinos or stops) and the neutralino. The branching fraction of the main particle decay is usually assumed to be 100%.

Above the TeV scale, the top has a large chance to be boosted due to the decay of their heavy supersymmetric mothers. In our search, we chose to increase the sensitivity to such signals by incorporating boosted object tagging techniques. We also used the razor variables, M_R and R^2 , which have proven to be very sensitive discriminators in many analyses for signals with pair produced heavy objects which decay to hadrons and invisible particles. Standard Model background processes typically produce a nearly exponentially falling distribution, peaked near zero, while signals produce a peak typically at higher values for large mass differences between the masses of the gluino (or top squark) and the neutralino.

Due its important roles in physics, the careful operation and maintenance of the pixel detector was key for the success of the CMS experiment. With the help of my PhD supervisor, we developed a hit efficiency measurement after which I periodically monitored this important detector performance observable. A large dynamic inefficiency was observed at high luminosities [33, 37, 38, 39, 40, 41, 42, 46, 48, 49, 50]. The main source of the inefficiency was identified to originate from the limited size of the internal

data buffers. These measurements helped to finalize the design of the Phase 1 Upgrade pixel detector to mitigate these effects [44]. The improved performance was validated in 2017 after the new detector was deployed [34, 36].

From 2011, I contributed to the calibration of the CMS pixel detector in order to ensure its excellent performance that is required for our physics goals. In the beginning of the data taking period of each year, I did the validation of both the global and internal time alignment of the detector by measuring the hit efficiency and other important cluster properties in order to determine the best working settings [33, 46]. These measurements became crucial in 2017 for the calibration of the Phase 1 Upgrade detector [34, 36] in order to mitigate the negative effects of a timing shift originating from a design issue. I also contributed to the validation of other calibrations through the periodic monitoring of the cluster size and charge [46].

The continuous irradiation of the detector causes a change in the cluster properties. It requires constant monitoring and calibration efforts in order to mitigate possible efficiency and resolution losses. I have performed the analysis of the so-called high voltage bias scans which are measurements of key performance related observables as a function of the applied bias voltage [37, 38, 39, 40, 41]. These measurements served as a validation of the voltage calibration and gave important feedback about the expected lifetime of the detector.

In collaboration with other researchers, of which I was the principal investigator, we performed a search for supersymmetry with 35.867 fb^{-1} proton-proton collision data collected by the CMS detector in 2016 at a center-of-mass energy of 13 TeV. The signal models of interest contained partially or fully merged wide cone top quark jets in the final state. The events were categorized in bins of the Razor variables. The observed data

counts in the search regions were statistically compatible with the standard model background prediction. The main source of uncertainty was statistical. Due to the absence of any signal, these results were interpreted as exclusion limits on the parameter space for various SUSY simplified models; and combined with that of a similar but more inclusive razor analysis within CMS, which excluded the boosted object selection, in order to increase the sensitivity. The combined exclusion limits gave better limits than what was possible to achieve separately by both analysis. The biggest improvement with the combination came for a low *top* squark mass T5ttcc model, where the *tops* had a higher probability to gain boost compared to the other two models. The collaboration published our combined preliminary results in a Physics Analysis Summary [104], which improved upon the best, previously observed limits of CMS:

- for the exclusion of the gluino mass by ≈ 100 GeV in the T5ttcc model;
- and by ≈ 20 GeV for the top squark mass in the T2tt model of direct top squark pair production.

Apart from the preliminary publication, the results were published in the Journal of High Energy Physics [105].

Összefoglaló

A PhD tanulmányaim első részében az előbbi detektor távoli (“offline”) kalibrációs, szoftveres rekonstrukciós valamint a működési monitorozási feladatok koordinációjáért voltam felelős. Ez magába foglalja, többek között, a beütés találási hatások, valamint a töltött részecskék detektorban deponált töltéseinek, vagy röviden klasztereinek vizsgálatát.

A tanulmányaim második részében a SUSY által jósolt új részecskéket kerestem. Eddig az LHC-ban még nem mutatkozott semmilyen jele Standard Modellen túli új fizikának. A két legnagyobb LHC kísérlet, a CMS és az ATLAS bizonyos új SUSY részecskék tömegeit már a TeV-os skálán zárja ki a legtöbbet idézett publikációiban. Ezek az analízisek tipikusan nagy mennyiségű könnyű- és b-kvark eredetű hadron záporokat és jelentős mértékű hiányzó transzverz lendületet jeleit keresték. A legtöbb LHC keresés az úgynevezett egyszerűsített SUSY modelleket használja, amelyek csak egy néhány új részecskéről feltételezik, hogy azok tömege alacsony. Az ilyen modelleket kis számú szabad paraméterrel rendelkező effektív Lagrange-függvényének írják le. Ezek a paraméterek többnyire az új részecskék tömegei, de lehetnek elágazási arányok és hatáskeresztmetszetek is. Az így megkonstruált analízisek szenzitívek lehetnek általános, széles spektrumú de akár jobban elkülönülő, specifikusabb SUSY jelekre is.

2012-ben, az LHC első futási periódusában (angolul Run 1) is részt vettem egy SUSY keresésben [10], melyben az egy leptonos azonosítási, rekonstrukciós és adat gyűjtési hatások mérésével járultam hozzá a leptonnal

kapcsolatos szisztematikus bizonytalanságok becsléséhez. A Run 1-es adatok lehetővé tették a 1.1 TeV alatti tömegű gluínók kizárását bizonyos esetekben. A Run 2-ben majdnem megduplázó tömegközépponti energia és luminozítás arra motivált, hogy egy speciálisabb kereséssel folytassam a kutatásaimat. A vizsgált modellekben nagy tömegű gluínók vagy top skvarkok keletkeztek, melyek más ismert SM részecskékre és a csak gyengén kölcsönható LSP-re bomlottak. Az utóbbi nem detektálható, de jelenlétére utalhat a jelentős hiányzó transzverz impulzus. Az így felépített egyszerűsített modellek szabad paraméterei az anya részecskék (gluínók vagy top skvarkok) és a neutralínó tömegére korlátozódnak. Az elágazási arányt 100%-nak szokás feltételezni.

A TeV-es skálán nagy az esély, hogy a keletkező top kvarkok nagy Lorentz-lökést (“boostot”) kapnak az elbomló nehéz szuperszimmetrikus anya részecskétől. A keresésünk szenzitivitását ezért boostolt objektum felismerési technikákkal növeltük. Ezen kívül az úgynevezett razor változókat (M_R és R^2) is felhasználtuk, melyek hasznosnak bizonyultak a párban keletkező, hadronosan és láthatatlan részecskékre bomló nehéz részecskék azonosításában. A SM hátterek tipikusan nulla közeli csúcsú, exponenciálisan csökkenő eseményeloszlásokat, míg a jel események javarészt nagyobb értéken csúcsosodó eloszlásokat adnak ha nagy a gluínó (vagy top skvark) és a neutrínó tömegei közti különbség.

A fizikában betöltött fontos szerepe miatt a pixel detektor gondos működtetése és karbantartása elsődleges fontosságú volt a CMS kísérlet sikeréhez. A PhD témavezetőm segítségével kifejlesztettük a detektor beütés találási határfokának mérését. Ezt a fontos detektor teljesítmény tényezőt utána rendszeresen monitoroztam is. Nagy luminozításokon nagy mértékű dinamikus határfokvesztést észleltünk [33, 37, 38, 39, 40, 41, 42, 46, 48, 49,

50]. A hatásfokvesztés fő forrását a belső adat pufferek limitált méretével azonosítottuk. A hatásfok mérések segítettek véglegesíteni az első fázisban felújított detektor dizájnját, amellyel mérsékelni lehetett a hatást [44]. 2017-ben, miután az új detektort üzembe helyezték a hatásfok méréseim megerősítették a javuló teljesítményt.

2011-től részt vettem a CMS pixel detektorának kalibrációiban, amellyel hozzájárultam a fizikai célokhoz elengedhetetlen, kiváló detektor teljesítmény biztosításához. Minden év adatgyűjtési periódusának elején én ellenőriztem a detektor időzítését és annak finomhangolását a hatásfok mérések és a pixel klaszter tulajdonságok vizsgálatával, mellyel a legjobb működési beállítást is kiválasztottuk [33, 46]. Ezek a mérések különösen fontossá váltak 2017-ben, az első fázisban felújított detektor kalibrációja során [34, 36], amikor egy nem várt dizájn probléma folytán fellépő időzítési eltérés hatását kellett a minimumra mérsékelni. Más további kalibráció validációjához is hozzájárultam a pixel klaszter töltések és méretek rendszeres monitorozásával.

Az állandó besugárzás eredményeképp a detektor klasztereinek tulajdonságai megváltoznak. A lehetséges hatásfok- és felbontás veszteség mérséklése állandó monitorozási és kalibrációs törekvéseket igényel. Én végeztem el az úgynevezett magas feszültségű pásztázások kiértékelését [37, 38, 39, 40, 41], amely a fontosabb teljesítmény változók mérését jelentette a rákapcsolt magas feszültség változtatása közben. Ezek a mérések a feszültség kalibrációk érvényesítéséhez, valamint a detektor várható életkorának meghatározásához is hozzájárultak.

Vezető kutatóként, más kutatókkal együttműködésben egy szuperszimmetria keresést végeztünk el a CMS detektor 2016-os, 35.867b^{-1} mennyiségű, 13 TeV tömegközépponti energiájú proton-proton ütközési adatainak

kiértékelésével. A vizsgált jel eseménytípusok végállapotai részben vagy teljesen egybeolvadó, nagy kúpszögű, top kvark bomlásból eredő hadron záporokat, idegen szóval boostolt objektumokat tartalmaztak. Az eseményeket a razor változók értéke szerint különböző tartományokba osztályoztuk. A jel tartomány adatban megfigyelt eseményszámai statisztikusan egyeztek a Standard Modell által becsült háttér események számával. A legnagyobb mérési bizonytalanság statisztikus jellegű volt. A megfigyelt jel hiányában az eredményeket különböző egyszerűsített SUSY modellek paraméter terében való kizárásként értelmeztük, valamint a szenzitivitás javításának céljából kombináltuk egy hasonló de még inkluzívabb razor analízis eredményeivel, amely eseményválogatásában kizárta az általunk vizsgált boostolt objektumokat. A kombináció jobb kizárási határokat adott, mint a két analízis által külön-külön elértek. A legnagyobb javulást a kis tömegű top skvarkot feltételező $T5ttcc$ modell esetében értük el, ahol a top kvarkoknak nagyobb esélye volt, hogy jelentősebb lendületre (boostra) tegyenek szert, mint a másik két vizsgált modell esetében.

A kollaboráció egy fizikai analízis összefoglalóban előzetesen publikálta [104] a kombinált eredményünket, amely javított a már előzőleg a CMS által megfigyelt legjobb kizárási határokon is az alábbiak szerint:

- ≈ 100 GeV-vel növelte a kizárt gluínók tömegét a $T5ttcc$ modell esetében;
- és ≈ 20 GeV-vel növelte a kizárt top skvarkok tömegét a $T2tt$, top skvark-pár keletkezési modell esetében.

Az előzetes publikáción kívül az eredmények megjelentek a JHEP nemzetközi folyóiratban is [105].

Bibliography

- [1] Y. A. Golfand and E. P. Likhtman, “Extension of the Algebra of Poincare Group Generators and Violation of p Invariance,” JETP Lett. **13** (1971) 323 [Pisma Zh. Eksp. Teor. Fiz. **13** (1971) 452].
- [2] J. Wess and B. Zumino, “Supergauge Transformations in Four-Dimensions,” Nucl. Phys. B **70** (1974) 39. doi:10.1016/0550-3213(74)90355-1
- [3] H. P. Nilles, “Supersymmetry, Supergravity and Particle Physics,” Phys. Rept. **110** (1984) 1. doi:10.1016/0370-1573(84)90008-5
- [4] H. E. Haber and G. L. Kane, “The Search for Supersymmetry: Probing Physics Beyond the Standard Model,” Phys. Rept. **117** (1985) 75. doi:10.1016/0370-1573(85)90051-1
- [5] R. Barbieri, S. Ferrara and C. A. Savoy, “Gauge Models with Spontaneously Broken Local Supersymmetry,” Phys. Lett. **119B** (1982) 343. doi:10.1016/0370-2693(82)90685-2
- [6] S. Dawson, E. Eichten, C. Quigg, “Search for supersymmetric particles in hadron-hadron collisions,” Phys. Rev. D **31** (1985) 1581. doi:10.1103/PhysRevD.31.1581
- [7] S. Chatrchyan *et al.* [CMS Collaboration], “The CMS Experiment at the CERN LHC,” JINST **3** (2008) S08004. doi:10.1088/1748-0221/3/08/S08004

- [8] S. Chatrchyan *et al.* [CMS Collaboration], “Observation of a new boson at a mass of 125 GeV with the CMS experiment at the LHC,” Phys. Lett. B **716** (2012) 30 doi:10.1016/j.physletb.2012.08.021 [arXiv:1207.7235 [hep-ex]].
- [9] G. Aad *et al.* [ATLAS Collaboration], “Observation of a new particle in the search for the Standard Model Higgs boson with the ATLAS detector at the LHC,” Phys. Lett. B **716** (2012) 1 doi:10.1016/j.physletb.2012.08.020 [arXiv:1207.7214 [hep-ex]].
- [10] S. Chatrchyan *et al.* [CMS Collaboration], “Search for supersymmetry in pp collisions at $\sqrt{s}=8$ TeV in events with a single lepton, large jet multiplicity, and multiple b jets,” Phys. Lett. B **733** (2014) 328 doi:10.1016/j.physletb.2014.04.023 [arXiv:1311.4937 [hep-ex]].
- [11] C. Rogan, “Kinematical variables towards new dynamics at the LHC,” arXiv:1006.2727 [hep-ph].
- [12] V. Khachatryan *et al.* [CMS Collaboration], “Search for supersymmetry in pp collisions at $\sqrt{s} = 8$ TeV in final states with boosted W bosons and b jets using razor variables,” Phys. Rev. D **93** (2016) no.9, 092009 doi:10.1103/PhysRevD.93.092009 [arXiv:1602.02917 [hep-ex]].
- [13] V. Khachatryan *et al.* [CMS Collaboration], “Inclusive search for supersymmetry using razor variables in pp collisions at $\sqrt{s} = 13$ TeV,” Phys. Rev. D **95** (2017) no.1, 012003 doi:10.1103/PhysRevD.95.012003 [arXiv:1609.07658 [hep-ex]].
- [14] A. J. Larkoski, S. Marzani, G. Soyez and J. Thaler, “Soft Drop,” JHEP **1405** (2014) 146 doi:10.1007/JHEP05(2014)146 [arXiv:1402.2657 [hep-ph]].
- [15] J. Thaler and K. Van Tilburg, “Identifying Boosted Objects with N-subjettiness,” JHEP **1103** (2011) 015 doi:10.1007/JHEP03(2011)015 [arXiv:1011.2268 [hep-ph]].

- [16] D. Bertolini, P. Harris, M. Low and N. Tran, “Pileup Per Particle Identification,” JHEP **1410** (2014) 059 doi:10.1007/JHEP10(2014)059 [arXiv:1407.6013 [hep-ph]].
- [17] A. M. Sirunyan *et al.* [CMS Collaboration], “Jet algorithms performance in 13 TeV data,” CMS Physics Analysis Summary CMS-PAS-JME-16-003 (2017) <http://cds.cern.ch/record/2256875>.
- [18] S. Chatrchyan *et al.* [CMS Collaboration], “Interpretation of Searches for Supersymmetry with simplified Models,” Phys. Rev. D **88** (2013) no.5, 052017 doi:10.1103/PhysRevD.88.052017 [arXiv:1301.2175 [hep-ex]].
- [19] S. Chatrchyan *et al.* [CMS Collaboration], “Search for supersymmetry in hadronic final states with missing transverse energy using the variables α_T and b-quark multiplicity in pp collisions at $\sqrt{s} = 8$ TeV,” Eur. Phys. J. C **73** (2013) no.9, 2568 doi:10.1140/epjc/s10052-013-2568-6 [arXiv:1303.2985 [hep-ex]].
- [20] S. Chatrchyan *et al.* [CMS Collaboration], “Search for gluino mediated bottom- and top-squark production in multijet final states in pp collisions at 8 TeV,” Phys. Lett. B **725** (2013) 243 doi:10.1016/j.physletb.2013.06.058 [arXiv:1305.2390 [hep-ex]].
- [21] V. Khachatryan *et al.* [CMS Collaboration], “Searches for electroweak neutralino and chargino production in channels with Higgs, Z, and W bosons in pp collisions at 8 TeV,” Phys. Rev. D **90** (2014) no.9, 092007 doi:10.1103/PhysRevD.90.092007 [arXiv:1409.3168 [hep-ex]].
- [22] V. Khachatryan *et al.* [CMS Collaboration], “Searches for Supersymmetry using the M_{T2} Variable in Hadronic Events Produced in pp Collisions at 8 TeV,” JHEP **1505** (2015) 078 doi:10.1007/JHEP05(2015)078 [arXiv:1502.04358 [hep-ex]].

- [23] G. Aad *et al.* [ATLAS Collaboration], “Search for squarks and gluinos using final states with jets and missing transverse momentum with the ATLAS detector in $\sqrt{s} = 7$ TeV proton-proton collisions,” *Phys. Lett. B* **710** (2012) 67 doi:10.1016/j.physletb.2012.02.051 [arXiv:1109.6572 [hep-ex]].
- [24] G. Aad *et al.* [ATLAS Collaboration], “Search for squarks and gluinos using final states with jets and missing transverse momentum with the ATLAS detector in $\sqrt{s} = 7$ TeV proton-proton collisions,” *Phys. Lett. B* **701** (2011) 186 doi:10.1016/j.physletb.2011.05.061 [arXiv:1102.5290 [hep-ex]].
- [25] G. Aad *et al.* [ATLAS Collaboration], “Search for squarks and gluinos with the ATLAS detector in final states with jets and missing transverse momentum using 4.7 fb^{-1} of $\sqrt{s} = 7$ TeV proton-proton collision data,” *Phys. Rev. D* **87** (2013) no.1, 012008 doi:10.1103/PhysRevD.87.012008 [arXiv:1208.0949 [hep-ex]].
- [26] G. Aad *et al.* [ATLAS Collaboration], “Search for squarks and gluinos with the ATLAS detector in final states with jets and missing transverse momentum using $\sqrt{s} = 8$ TeV proton-proton collision data,” *JHEP* **1409** (2014) 176 doi:10.1007/JHEP09(2014)176 [arXiv:1405.7875 [hep-ex]].
- [27] J. Alwall, P. Schuster and N. Toro, “Simplified Models for a First Characterization of New Physics at the LHC,” *Phys. Rev. D* **79** (2009) 075020 doi:10.1103/PhysRevD.79.075020 [arXiv:0810.3921 [hep-ph]].
- [28] J. Alwall, M. P. Le, M. Lisanti and J. G. Wacker, “Model-Independent Jets plus Missing Energy Searches,” *Phys. Rev. D* **79** (2009) 015005 doi:10.1103/PhysRevD.79.015005 [arXiv:0809.3264 [hep-ph]].
- [29] D. Alves *et al.* [LHC New Physics Working Group], “Simplified Models for LHC New Physics Searches,” *J. Phys. G* **39** (2012) 105005 doi:10.1088/0954-3899/39/10/105005 [arXiv:1105.2838 [hep-ph]].

- [30] CMS Collaboration, “Images for US LHC CMS Detector Upgrade Project”, CMS-doc-11814, <https://cms-docdb.cern.ch/cgi-bin/PublicDocDB/ShowDocument?docid=11806>.
- [31] S. Chatrchyan *et al.* [CMS Collaboration], “Description and performance of track and primary-vertex reconstruction with the CMS tracker”, JINST **9** (2014) no.10, P10009 doi:10.1088/1748-0221/9/10/P10009 [arXiv:1405.6569 [physics.ins-det]].
- [32] CMS Collaboration, “SketchUp Drawings of the Phase 1 pixel detector alongside the current pixel detector”, CMS-doc-6473-v1, <https://cms-docdb.cern.ch/cgi-bin/PublicDocDB/ShowDocument?docid=6473>.
- [33] J. Karancsi [CMS Collaboration], “Operational Experience with the CMS Pixel Detector”, JINST **10** (2015) no.05, C05016 doi:10.1088/1748-0221/10/05/C05016 [arXiv:1411.4185 [physics.ins-det]].
- [34] V. Veszpremi [CMS Collaboration], “Performance verification of the CMS Phase-1 Upgrade Pixel detector”, JINST **12** (2017) no.12, C12010 doi:10.1088/1748-0221/12/12/C12010 [arXiv:1710.03842 [physics.ins-det]].
- [35] A. Starodumov *et al.* [CMS Collaboration], “High rate capability and radiation tolerance of the PROC600 readout chip for the CMS pixel detector”, JINST **12** (2017) no.01, C01078 doi:10.1088/1748-0221/12/01/C01078.
- [36] J. Sonneveld [CMS Collaboration], “Commissioning and first results from the CMS phase 1 upgrade pixel detector,” PoS Vertex **2017** (2018) 018 doi:10.22323/1.309.0018 [arXiv:1807.08987 [physics.ins-det]].
- [37] A. Gaz [CMS Collaboration], “CMS Pixel status”, Nucl. Instrum. Meth. A **731** (2013) 13. doi:10.1016/j.nima.2013.04.001.

- [38] V. Veszpremi [CMS Collaboration], “Operation and performance of the CMS tracker”, *JINST* **9** (2014) C03005 doi:10.1088/1748-0221/9/03/C03005 [arXiv:1402.0675 [physics.ins-det]].
- [39] V. Veszpremi [CMS Collaboration], “Radiation experience with the CMS pixel detector”, *JINST* **10** (2015) no.04, C04039 doi:10.1088/1748-0221/10/04/C04039 [arXiv:1411.5990 [physics.ins-det]].
- [40] M. Malberti [CMS Collaboration], “Operation and performance of the CMS tracker”, *PoS TIPP* **2014** (2014) 347 doi:10.22323/1.213.0347 <https://pos.sissa.it/213/347/pdf>.
- [41] A. De Cosa [CMS Collaboration], “CMS Pixel Detector: Operational Experience and Run 1 to Run 2 Transition”, *PoS Vertex* **2014** (2015) 003 doi:10.22323/1.227.0003 <https://pos.sissa.it/227/003/pdf>.
- [42] C. Lange [CMS Collaboration], “CMS inner detector: the Run 1 to Run 2 transition and first experience of Run 2”, *PoS VERTEX* **2015** (2015) 002 doi:10.22323/1.254.0002 <https://pos.sissa.it/254/002/pdf>.
- [43] L. Rossi, P. Fischer, T. Rohe, and N. Wermes, “Pixel detectors: From fundamentals to applications”, ISBN 978-3-540-28332-4, Springer-Verlag, Berlin, Heidelberg (2006) doi:10.1007/3-540-28333-1.
- [44] D. A. Matzner Dominguez *et al.* [CMS Collaboration], “CMS Technical Design Report for the Pixel Detector Upgrade,” *CERN-LHCC-2012-016*, *CMS-TDR-011*, *FERMILAB-DESIGN-2012-02* (2012), doi:10.2172/1151650.
- [45] M. Bartók [for CMS Collaboration], “Simulation of the Dynamic Inefficiency of the CMS Pixel Detector”, *JINST* **10** (2015) no.05, C05006 doi:10.1088/1748-0221/10/05/C05006 [arXiv:1411.6770 [physics.ins-det]].

- [46] J. Karancsi [CMS Collaboration], “Operational experience with the CMS pixel detector in LHC Run II”, JINST **11** (2016) no.12, C12057 doi:10.1088/1748-0221/11/12/C12057.
- [47] G. Benelli [CMS Collaboration], “Operation and performance of the CMS Tracker detector during early Run II”, ICHEP 2016 conference poster, 3-10 Aug 2016, Chicago, USA.
- [48] B. R. Vormwald [CMS Collaboration], “The CMS Tracker Upgrades – Pushing the Limits”, DPG2017 conference talk, 27-31 Mar 2017, Münster, Germany.
- [49] H. R. Delannoy [CMS Collaboration], “CMS Tracker performance in 2016”, TIPP2017 conference talk, 22-26 May 2017, Beijing, China.
- [50] M. Lipinski [CMS Collaboration], “The Phase-1 upgrade of the CMS pixel detector”, JINST **12** (2017) no.07, C07009 doi:10.1088/1748-0221/12/07/C07009.
- [51] M. Meinhard *et al.* [CMS Tracker Group], “Performance of the modules for layer 1 of the CMS phase 1 pixel detector upgrade”, JINST **12** (2017) no.12, C12002. doi:10.1088/1748-0221/12/12/C12002
- [52] A. M. Sirunyan *et al.* [CMS Collaboration], “Inclusive search for supersymmetry in pp collisions at $\sqrt{s} = 13$ TeV using razor variables and boosted object identification in zero and one lepton final states”, Paper submitted to JHEP (15 Dec 2018) <http://cms-results.web.cern.ch/cms-results/public-results/publications/SUS-16-017/> [arXiv:1812.06302 [hep-ex]].
- [53] J. Alwall, M. Herquet, F. Maltoni, O. Mattelaer and T. Stelzer, “MadGraph 5 : Going Beyond”, JHEP **1106** (2011) 128 doi:10.1007/JHEP06(2011)128 [arXiv:1106.0522 [hep-ph]].

- [54] T. Sjöstrand *et al.*, “An Introduction to PYTHIA 8.2”, *Comput. Phys. Commun.* **191** (2015) 159 doi:10.1016/j.cpc.2015.01.024 [arXiv:1410.3012 [hep-ph]].
- [55] S. Hoeche, F. Krauss, N. Lavesson, L. Lonnblad, M. Mangano, A. Schalicke and S. Schumann, “Matching parton showers and matrix elements”, doi:10.5170/CERN-2005-014.288 hep-ph/0602031.
- [56] J. Alwall *et al.*, “Comparative study of various algorithms for the merging of parton showers and matrix elements in hadronic collisions”, *Eur. Phys. J. C* **53** (2008) 473 doi:10.1140/epjc/s10052-007-0490-5 [arXiv:0706.2569 [hep-ph]].
- [57] J. Alwall *et al.*, “The automated computation of tree-level and next-to-leading order differential cross sections, and their matching to parton shower simulations”, *JHEP* **1407** (2014) 079 doi:10.1007/JHEP07(2014)079 [arXiv:1405.0301 [hep-ph]].
- [58] R. Frederix and S. Frixione, “Merging meets matching in MC@NLO”, *JHEP* **1212** (2012) 061 doi:10.1007/JHEP12(2012)061 [arXiv:1209.6215 [hep-ph]].
- [59] S. Frixione, E. Laenen, P. Motylinski and B. R. Webber, “Angular correlations of lepton pairs from vector boson and top quark decays in Monte Carlo simulations”, *JHEP* **0704** (2007) 081 doi:10.1088/1126-6708/2007/04/081 [hep-ph/0702198 [HEP-PH]].
- [60] P. Artoisenet, R. Frederix, O. Mattelaer and R. Rietkerk, “Automatic spin-entangled decays of heavy resonances in Monte Carlo simulations”, *JHEP* **1303** (2013) 015 doi:10.1007/JHEP03(2013)015 [arXiv:1212.3460 [hep-ph]].
- [61] P. Nason, “A New method for combining NLO QCD with shower Monte Carlo algorithms”, *JHEP* **0411** (2004) 040 doi:10.1088/1126-6708/2004/11/040 [hep-ph/0409146].

- [62] S. Frixione, P. Nason and C. Oleari, “Matching NLO QCD computations with Parton Shower simulations: the POWHEG method”, *JHEP* **0711** (2007) 070 doi:10.1088/1126-6708/2007/11/070 [arXiv:0709.2092 [hep-ph]].
- [63] S. Alioli, P. Nason, C. Oleari and E. Re, “A general framework for implementing NLO calculations in shower Monte Carlo programs: the POWHEG BOX”, *JHEP* **1006** (2010) 043 doi:10.1007/JHEP06(2010)043 [arXiv:1002.2581 [hep-ph]].
- [64] S. Frixione, P. Nason and G. Ridolfi, “A Positive-weight next-to-leading-order Monte Carlo for heavy flavour hadroproduction”, *JHEP* **0709** (2007) 126 doi:10.1088/1126-6708/2007/09/126 [arXiv:0707.3088 [hep-ph]].
- [65] S. Alioli, P. Nason, C. Oleari and E. Re, “NLO single-top production matched with shower in POWHEG: s- and t-channel contributions”, *JHEP* **0909** (2009) 111 Erratum: [*JHEP* **1002** (2010) 011] doi:10.1007/JHEP02(2010)011, 10.1088/1126-6708/2009/09/111 [arXiv:0907.4076 [hep-ph]].
- [66] E. Re, “Single-top Wt-channel production matched with parton showers using the POWHEG method”, *Eur. Phys. J. C* **71** (2011) 1547 doi:10.1140/epjc/s10052-011-1547-z [arXiv:1009.2450 [hep-ph]].
- [67] T. Melia, P. Nason, R. Rontsch and G. Zanderighi, “W+W-, WZ and ZZ production in the POWHEG BOX”, *JHEP* **1111** (2011) 078 doi:10.1007/JHEP11(2011)078 [arXiv:1107.5051 [hep-ph]].
- [68] P. Nason and G. Zanderighi, “ W^+W^- , WZ and ZZ production in the POWHEG-BOX-V2”, *Eur. Phys. J. C* **74** (2014) no.1, 2702 doi:10.1140/epjc/s10052-013-2702-5 [arXiv:1311.1365 [hep-ph]].

- [69] V. Khachatryan *et al.* [CMS Collaboration], “Event generator tunes obtained from underlying event and multiparton scattering measurements”, *Eur. Phys. J. C* **76** (2016) no.3, 155 doi:10.1140/epjc/s10052-016-3988-x [arXiv:1512.00815 [hep-ex]].
- [70] V. Khachatryan *et al.* [CMS Collaboration], “Investigations of the impact of the parton shower tuning in PYTHIA8 in the modelling of $t\bar{t}$ at $\sqrt{s} = 8$ and 13 TeV”, CMS Physics Analysis Summary CMS-PAS-TOP-16-021 (2016) <https://cds.cern.ch/record/2235192>.
- [71] R. D. Ball *et al.* [NNPDF Collaboration], “Parton distributions for the LHC Run II”, *JHEP* **1504** (2015) 040 doi:10.1007/JHEP04(2015)040 [arXiv:1410.8849 [hep-ph]].
- [72] S. Agostinelli *et al.* [GEANT4 Collaboration], “GEANT4: A Simulation toolkit”, *Nucl. Instrum. Meth. A* **506** (2003) 250. doi:10.1016/S0168-9002(03)01368-8.
- [73] S. Abdullin *et al.* [CMS Collaboration], “The fast simulation of the CMS detector at LHC”, *J. Phys. Conf. Ser.* **331** (2011) 032049. doi:10.1088/1742-6596/331/3/032049.
- [74] M. Aliev, H. Lacker, U. Langenfeld, S. Moch, P. Uwer and M. Wiedermann, “HATHOR: HAdronic Top and Heavy quarks crOss section calculatoR”, *Comput. Phys. Commun.* **182** (2011) 1034 doi:10.1016/j.cpc.2010.12.040 [arXiv:1007.1327 [hep-ph]].
- [75] P. Kant, O. M. Kind, T. Kintscher, T. Lohse, T. Martini, S. Mölbitz, P. Rieck and P. Uwer, “HatHor for single top-quark production: Updated predictions and uncertainty estimates for single top-quark production in hadronic collisions”, *Comput. Phys. Commun.* **191** (2015) 74 doi:10.1016/j.cpc.2015.02.001 [arXiv:1406.4403 [hep-ph]].

- [76] N. Kidonakis, “Top Quark Production”, doi:10.3204/DESY-PROC-2013-03/Kidonakis arXiv:1311.0283 [hep-ph].
- [77] M. Czakon and A. Mitov, “Top++: A Program for the Calculation of the Top-Pair Cross-Section at Hadron Colliders”, *Comput. Phys. Commun.* **185** (2014) 2930 doi:10.1016/j.cpc.2014.06.021 [arXiv:1112.5675 [hep-ph]].
- [78] Y. Li and F. Petriello, “Combining QCD and electroweak corrections to dilepton production in FEWZ”, *Phys. Rev. D* **86** (2012) 094034 doi:10.1103/PhysRevD.86.094034 [arXiv:1208.5967 [hep-ph]].
- [79] A. Kalogeropoulos and J. Alwall, “The SysCalc code: A tool to derive theoretical systematic uncertainties”, arXiv:1801.08401 [hep-ph].
- [80] A. M. Sirunyan *et al.* [CMS Collaboration], “Particle-flow reconstruction and global event description with the CMS detector”, *JINST* **12** (2017) no.10, P10003 doi:10.1088/1748-0221/12/10/P10003 [arXiv:1706.04965 [physics.ins-det]].
- [81] V. Khachatryan *et al.* [CMS Collaboration], “Performance of Electron Reconstruction and Selection with the CMS Detector in Proton-Proton Collisions at $\sqrt{s} = 8$ TeV”, *JINST* **10** (2015) no.06, P06005 doi:10.1088/1748-0221/10/06/P06005 [arXiv:1502.02701 [physics.ins-det]].
- [82] V. Khachatryan *et al.* [CMS Collaboration], “Studies of Higgs boson production in the four-lepton final state at $\sqrt{s} = 13$ TeV”, CMS Physics Analysis Summary CMS-PAS-TOP-16-021 (2016) <https://cds.cern.ch/record/2139978>.
- [83] V. Khachatryan *et al.* [CMS Collaboration], “Measurements of properties of the Higgs boson and search for an additional resonance in the four-lepton final state at $\sqrt{s} = 13$ TeV”, CMS Physics Analysis Summary CMS-PAS-HIG-16-0334 (2016) <https://cds.cern.ch/record/2204926>.

- [84] M. Cacciari and G. P. Salam, “Pileup subtraction using jet areas”, *Phys. Lett. B* **659** (2008) 119 doi:10.1016/j.physletb.2007.09.077 [arXiv:0707.1378 [hep-ph]].
- [85] A. M. Sirunyan *et al.* [CMS Collaboration], “Performance of the CMS muon detector and muon reconstruction with proton-proton collisions at $\sqrt{s} = 13$ TeV”, *JINST* **13** (2018) no.06, P06015 doi:10.1088/1748-0221/13/06/P06015 [arXiv:1804.04528 [physics.ins-det]].
- [86] A. M. Sirunyan *et al.* [CMS Collaboration], “Performance of reconstruction and identification of τ leptons decaying to hadrons and ν_τ in pp collisions at $\sqrt{s} = 13$ TeV”, CMS-TAU-16-003 paper submitted to JINST, <https://cds.cern.ch/record/2637646/>, [arXiv:1809.02816 [hep-ex]].
- [87] M. Cacciari, G. P. Salam and G. Soyez, “The anti- k_t jet clustering algorithm”, *JHEP* **0804** (2008) 063 doi:10.1088/1126-6708/2008/04/063 [arXiv:0802.1189 [hep-ph]].
- [88] V. Khachatryan *et al.* [CMS Collaboration], “Performance of Photon Reconstruction and Identification with the CMS Detector in Proton-Proton Collisions at $\sqrt{s} = 8$ TeV”, *JINST* **10** (2015) no.08, P08010 doi:10.1088/1748-0221/10/08/P08010 [arXiv:1502.02702 [physics.ins-det]].
- [89] M. Cacciari, G. P. Salam and G. Soyez, “FastJet User Manual”, *Eur. Phys. J. C* **72** (2012) 1896 doi:10.1140/epjc/s10052-012-1896-2 [arXiv:1111.6097 [hep-ph]].
- [90] V. Khachatryan *et al.* [CMS Collaboration], “Pileup Removal Algorithms”, CMS Physics Analysis Summary CMS-PAS-JME-14-001 (2014) <https://cds.cern.ch/record/1751454>.

- [91] M. Cacciari, G. P. Salam and G. Soyez, “The Catchment Area of Jets”, *JHEP* **0804** (2008) 005 doi:10.1088/1126-6708/2008/04/005 [arXiv:0802.1188 [hep-ph]].
- [92] V. Khachatryan *et al.* [CMS Collaboration], “Jet energy scale and resolution in the CMS experiment in pp collisions at 8 TeV”, *JINST* **12** (2017) no.02, P02014 doi:10.1088/1748-0221/12/02/P02014 [arXiv:1607.03663 [hep-ex]].
- [93] A. M. Sirunyan *et al.* [CMS Collaboration], “Identification of heavy-flavour jets with the CMS detector in pp collisions at 13 TeV”, *JINST* **13** (2018) no.05, P05011 doi:10.1088/1748-0221/13/05/P05011 [arXiv:1712.07158 [physics.ins-det]].
- [94] A. M. Sirunyan *et al.* [CMS Collaboration], “Performance of missing transverse momentum in pp collisions at $\sqrt{s}=13$ TeV using the CMS detector”, CMS Physics Analysis Summary CMS-PAS-JME-17-001 (2018) <https://cds.cern.ch/record/2628600>.
- [95] N. C. Strobbe, “The Razor Boost analysis - Another step in the hunt for new physics at CMS,” CMS-TS-2015-027, CERN-THESIS-2015-178.
- [96] V. Khachatryan *et al.* [CMS Collaboration], “Measurement of differential cross sections for top quark pair production using the lepton+jets final state in proton-proton collisions at 13 TeV”, *Phys. Rev. D* **95** (2017) no.9, 092001 doi:10.1103/PhysRevD.95.092001 [arXiv:1610.04191 [hep-ex]].
- [97] V. Khachatryan *et al.* [CMS Collaboration], “Jet energy scale and resolution in the CMS experiment in pp collisions at 8 TeV”, *JINST* **12** (2017) no.02, P02014 doi:10.1088/1748-0221/12/02/P02014 [arXiv:1607.03663 [hep-ex]].
- [98] CMS Collaboration [CMS Collaboration], “CMS Luminosity Measurements for the 2016 Data Taking Period”, CMS-PAS-LUM-17-001.

- [99] A. L. Read, “Presentation of search results: The CL(s) technique”, *J. Phys. G* **28** (2002) 2693. doi:10.1088/0954-3899/28/10/313
- [100] T. Junk, “Confidence level computation for combining searches with small statistics”, *Nucl. Instrum. Meth. A* **434** (1999) 435 doi:10.1016/S0168-9002(99)00498-2 [hep-ex/9902006].
- [101] [ATLAS and CMS Collaborations and LHC Higgs Combination Group], “Procedure for the LHC Higgs boson search combination in summer 2011”, ATL-PHYS-PUB-2011-011, CMS-NOTE-2011-005.
- [102] G. Cowan, K. Cranmer, E. Gross and O. Vitells, “Asymptotic formulae for likelihood-based tests of new physics”, *Eur. Phys. J. C* **71** (2011) 1554 Erratum: [*Eur. Phys. J. C* **73** (2013) 2501] doi:10.1140/epjc/s10052-011-1554-0, 10.1140/epjc/s10052-013-2501-z [arXiv:1007.1727 [physics.data-an]].
- [103] C. Borschensky, M. Krämer, A. Kulesza, M. Mangano, S. Padhi, T. Plehn and X. Portell, “Squark and gluino production cross sections in pp collisions at $\sqrt{s} = 13, 14, 33$ and 100 TeV”, *Eur. Phys. J. C* **74** (2014) no.12, 3174 doi:10.1140/epjc/s10052-014-3174-y [arXiv:1407.5066 [hep-ph]].
- [104] CMS Collaboration [CMS Collaboration], “Inclusive search for supersymmetry using razor variables in pp collisions at $\sqrt{s} = 13$ TeV,” CMS-PAS-SUS-16-017 <https://cds.cern.ch/record/2637598>.
- [105] A. M. Sirunyan *et al.* [CMS Collaboration], “Inclusive search for supersymmetry in pp collisions at $\sqrt{s} = 13$ TeV using razor variables and boosted object identification in zero and one lepton final states,” *JHEP* **1903** (2019) 031 doi:10.1007/JHEP03(2019)031 [arXiv:1812.06302 [hep-ex]]. **IF: 5.541**

Appendices

A Boosted object tagging scale factors

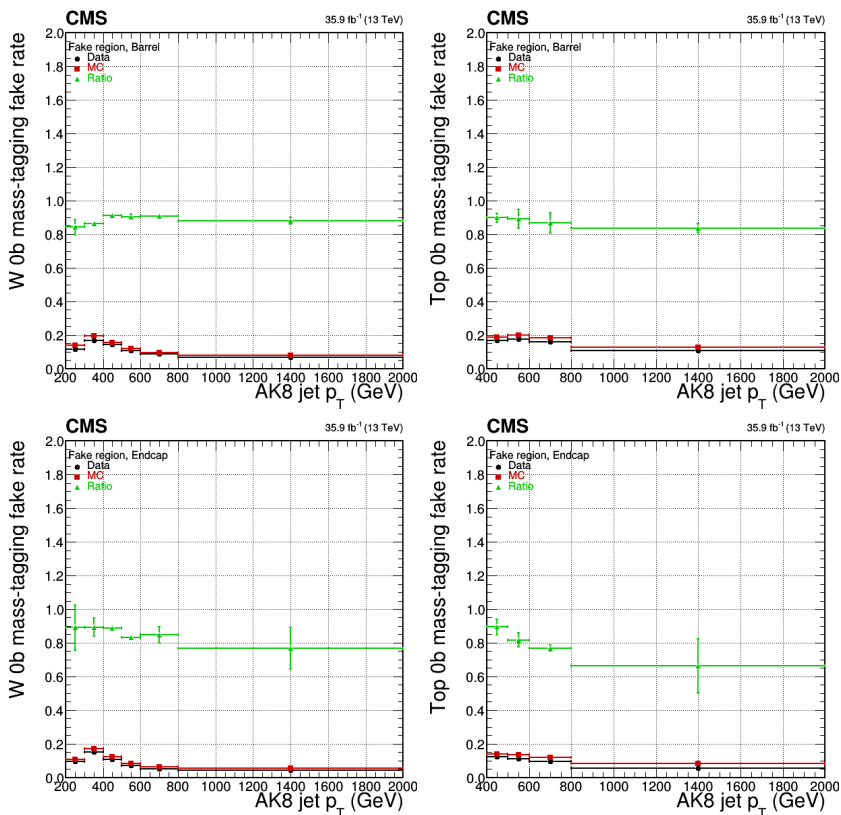


Figure A1: W mass-tagging (left) and top mass-tagging (including subjet b -tag veto) (right) fake rates and scale factors as a function of AK8 jet p_T , for barrel (top) and endcap (bottom) regions. The control region is selected with a veto of charged leptons and b -tags, at least three AK4 jets and an AK8 jet and $\Delta\phi_{megajets} \geq 2.8$. The error bars show both the statistical and the systematic uncertainty. The latter contains a variation of the jet energy scale and the number of b -tags.

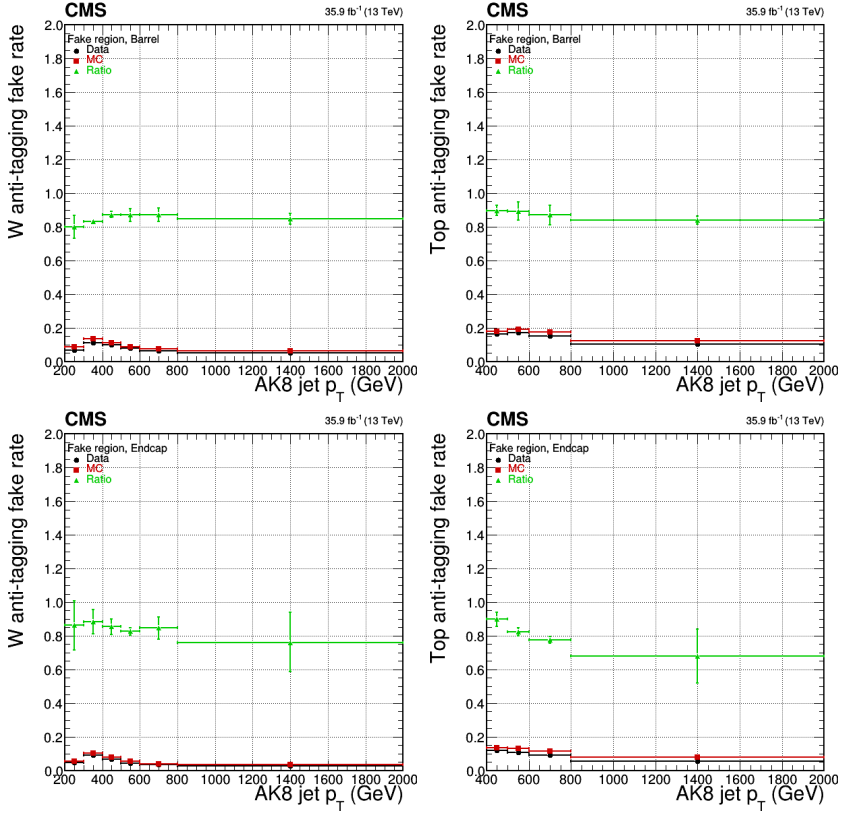


Figure A2: W anti-tagging (left), top anti-tagging (including subjet b -tag veto, right) fake rates and scale factors as a function of AK8 jet p_T , for barrel (top) and endcap (bottom) regions. The control region is selected with a veto of charged leptons and b -tags, at least three AK4 jets and an AK8 jet and $\Delta\phi_{megajets} \geq 2.8$. The error bars show both the statistical and the systematic uncertainty. The latter contains a variation of the jet energy scale and the number of b -tags.

B Additional tables and figures

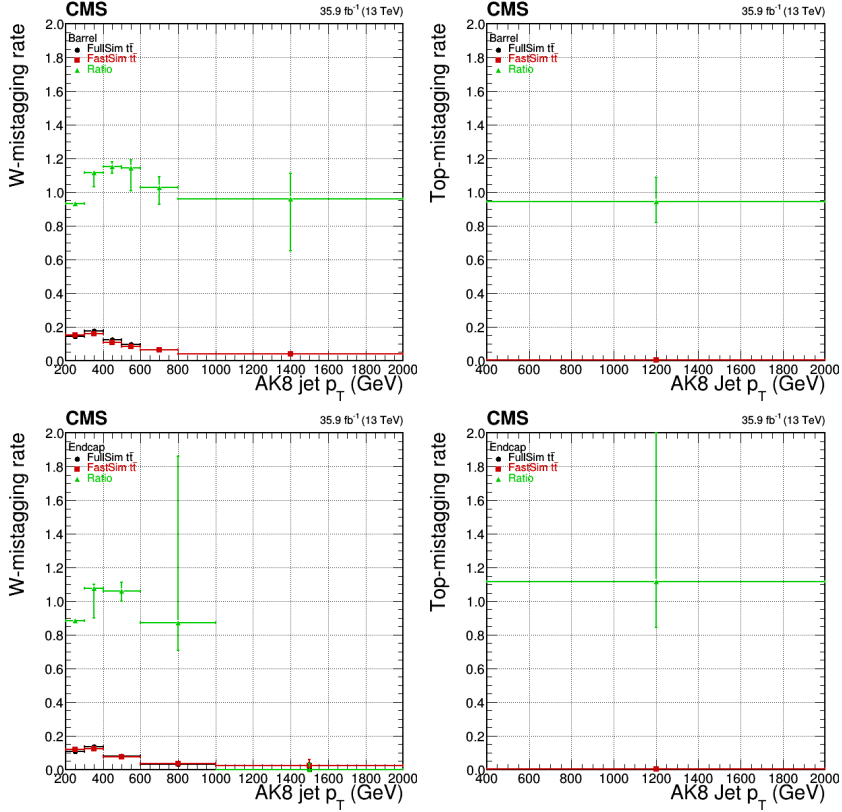


Figure A3: W -mistagging (left), top -mistagging (right) rates and scale factors as a function of AK8 jet p_T , for barrel (top) and endcap (bottom) regions. The control region is selected with a veto of charged leptons and b -tags, at least three AK4 jets and an AK8 jet and $\Delta\phi_{megajets} \geq 2.8$. The error bars show both the statistical and the systematic uncertainty. The latter contains a variation of the jet energy scale and the number of b -tags.

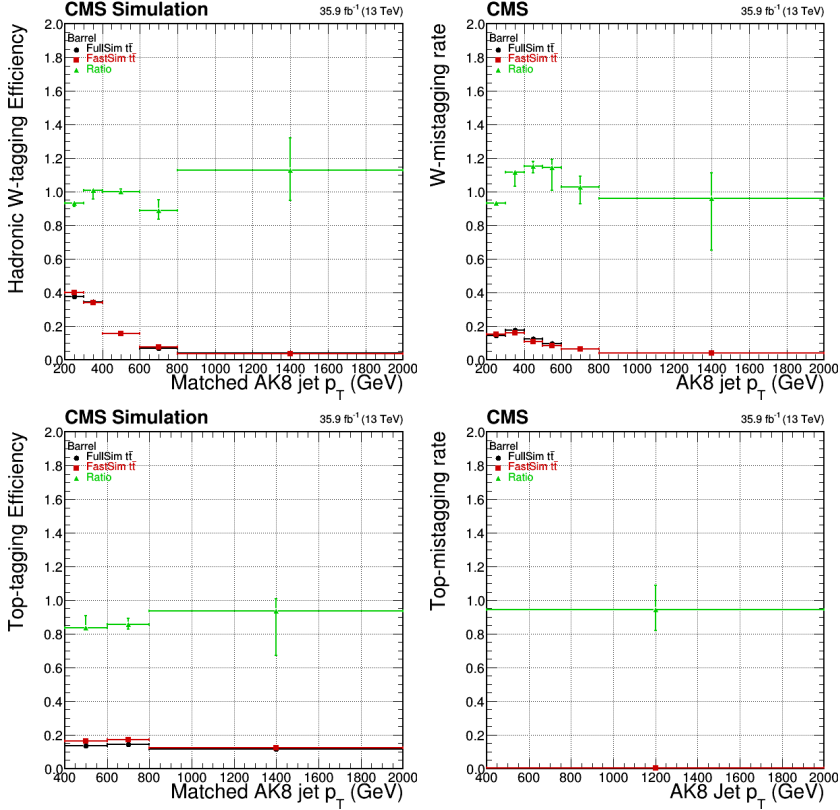


Figure A4: W -tagging (top left), W -mistagging (top right), top -tagging (bottom left) and top -mistagging FullSim/FastSim efficiencies and scale factors as a function of AK8 jet p_T for the barrel region. The measurement was done in a $t\bar{t}$ sample reconstructed with both types of simulations requiring at least one top quark or a hadronically decaying W within $\Delta R = 0.8$ from the AK8 jet. The error bars show both the statistical and the systematic uncertainty. The latter is calculated from the difference from the measurement in the baseline selection region defined in Section 3.5.1.

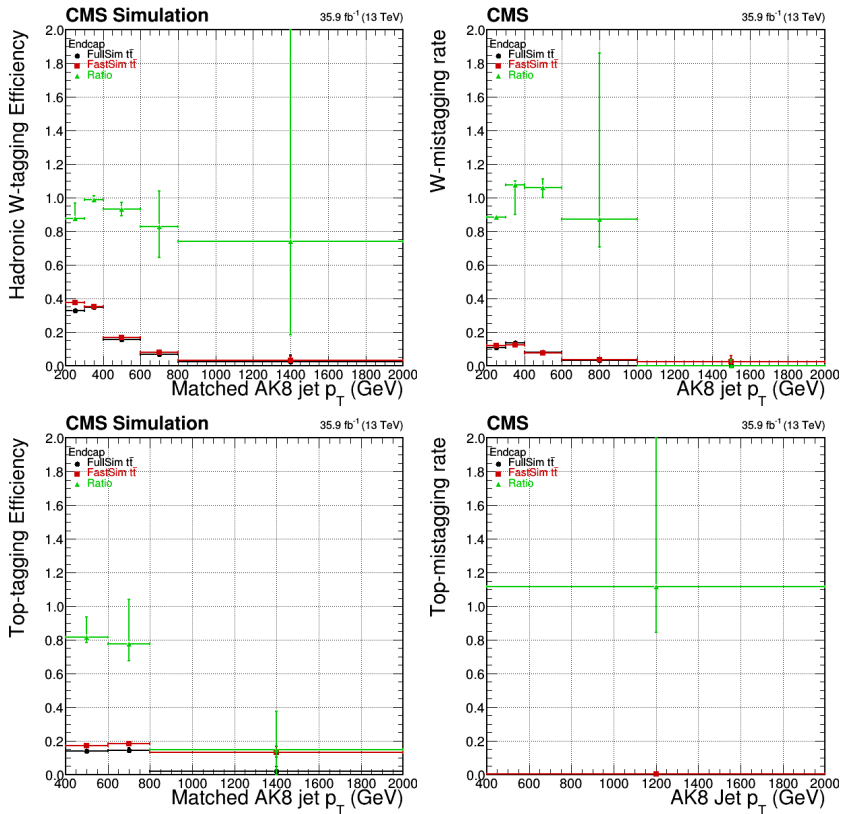


Figure A5: W -tagging (top left), W -mistagging (top right), top -tagging (bottom left) and top -mistagging FullSim/FastSim efficiencies and scale factors as a function of AK8 jet p_T for the endcap region. The measurement was done in a $t\bar{t}$ sample reconstructed with both types of simulations requiring at least one top quark or a hadronically decaying W within $\Delta R = 0.8$ from the AK8 jet. The error bars show both the statistical and the systematic uncertainty. The latter is calculated from the difference from the measurement in the baseline selection region defined in Section 3.5.1.

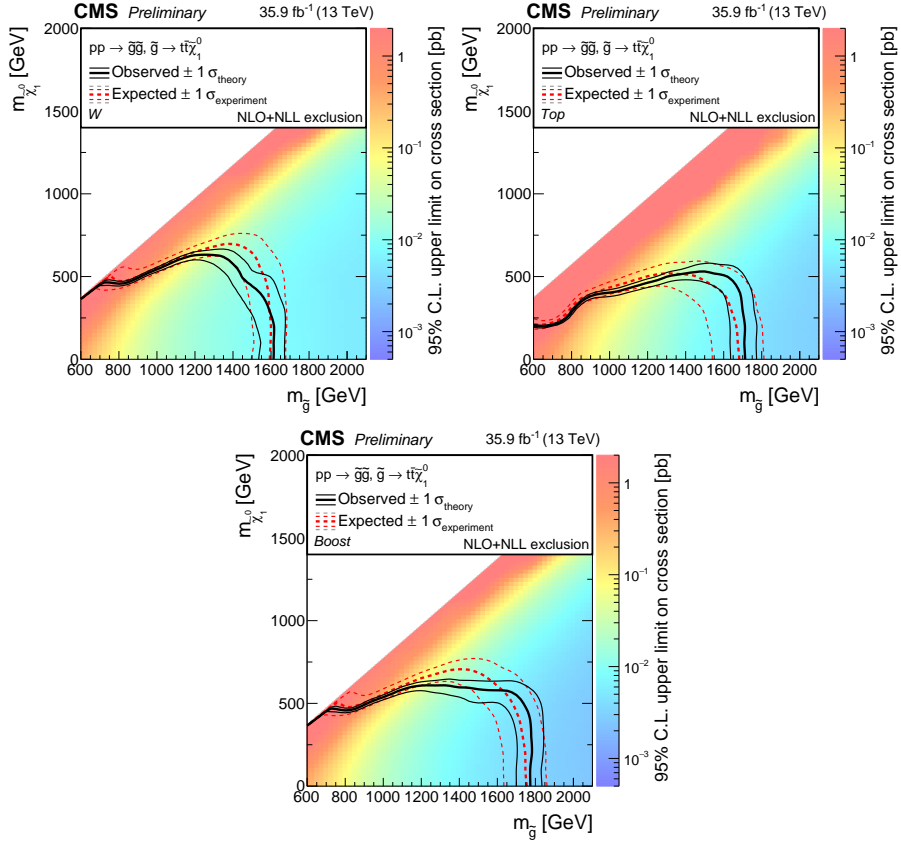


Figure B1: 95% CL exclusion limits on the production cross section of gluino pair production where each gluino decays to a neutralino and top quark ($T1tttt$). The top left plot shows the combination of the two boosted W categories, the top right shows the limit with top category alone and the bottom one shows the combination of all boosted categories. The solid black lines show the observed limit from data together with the ± 1 standard deviation contours corresponding to the uncertainties of the NLO+NLL cross section calculations. Similar dashed contours represent the expected limits and the ± 1 standard deviation experimental uncertainties.

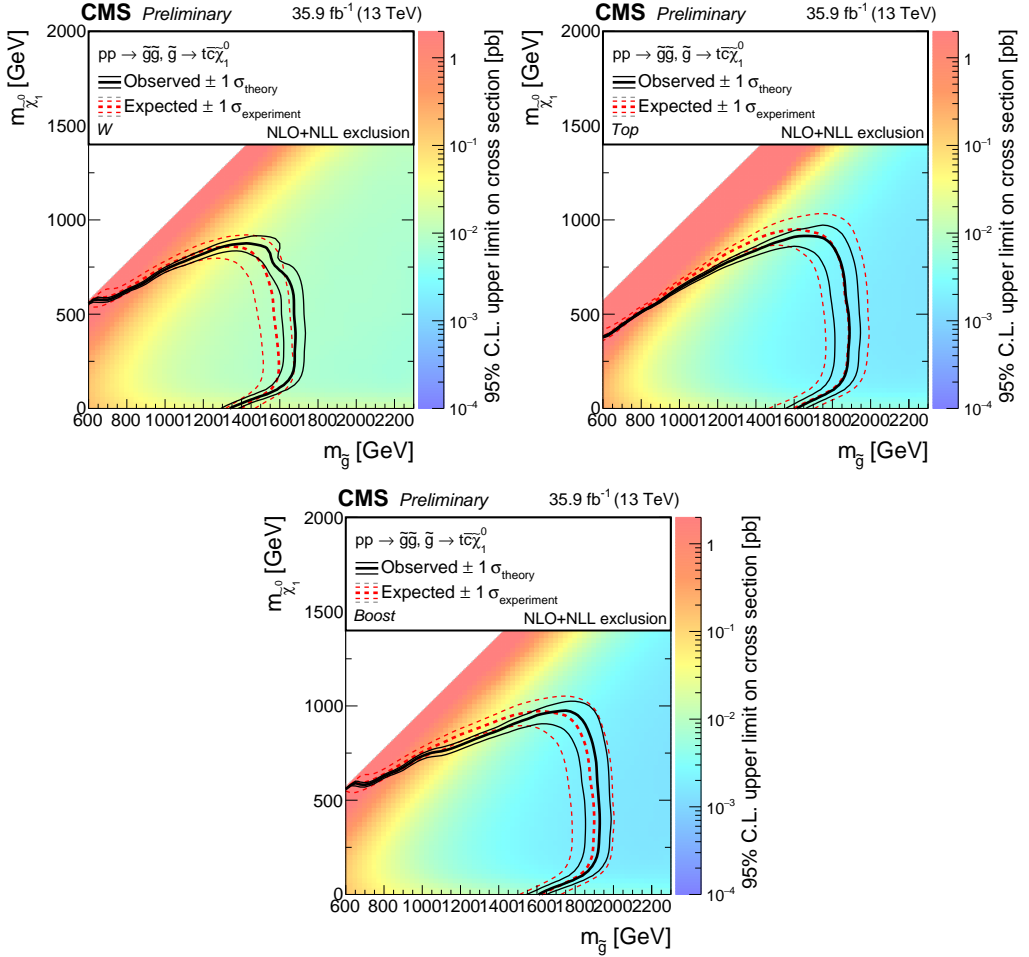


Figure B2: 95% CL exclusion limits on the production cross section of gluino pair production where each gluino decays to a top squark and top quark and the former subsequently decays to a neutralino and a charm quark ($T5ttcc$). The top left plot shows the combination of the two boosted W categories, the top right show the limit with top category alone and the bottom one shows the combination of all boosted categories. The mass of the top squark is fixed to be 20 GeV below that of the neutralino. The solid black lines show the observed limit from data together with the ± 1 standard deviation contours corresponding to the uncertainties of the NLO+NLL cross section calculations. Similar dashed contours represent the expected limits and the ± 1 standard deviation experimental uncertainties.

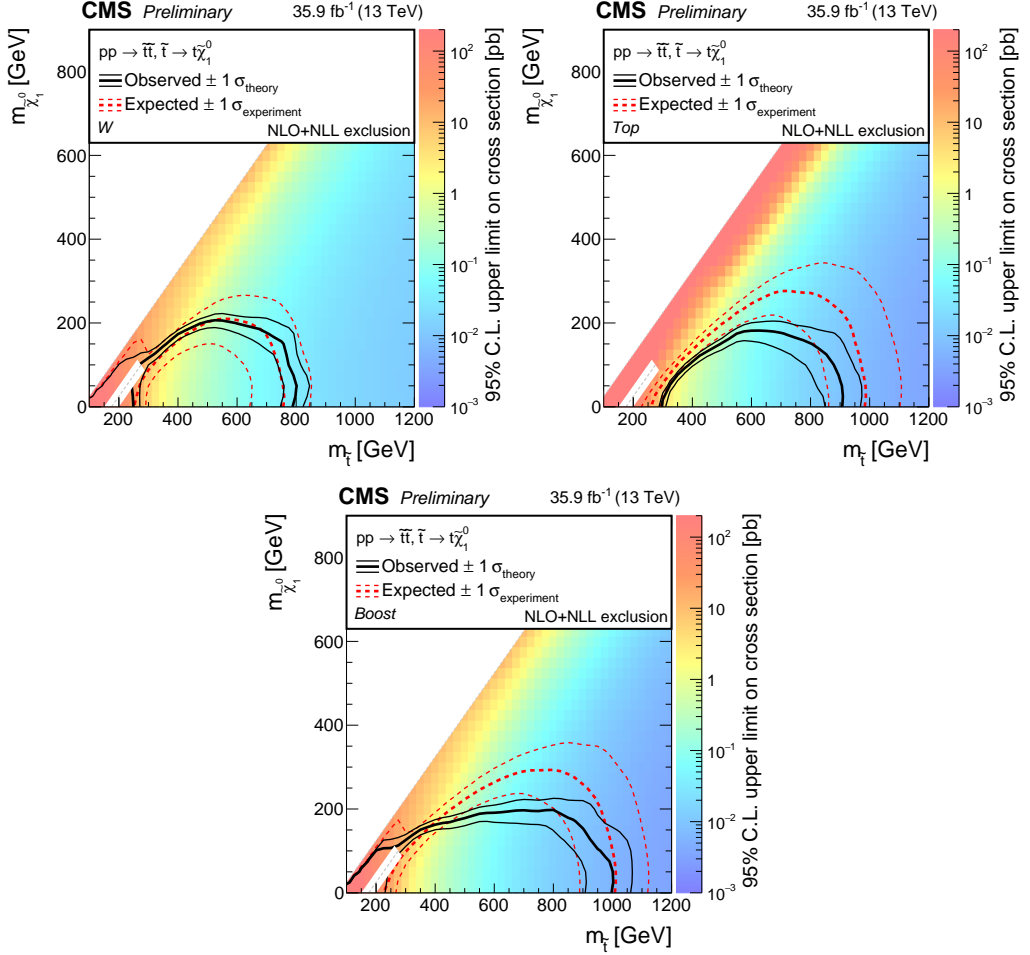


Figure B3: 95% CL exclusion limits on the production cross section of pair-produced top squarks each decaying to a neutralino and top quark (T2tt). The top left plot shows the combination of the two boosted W categories, the top right show the limit with top category alone and the bottom one shows the combination of all boosted categories. The solid black lines show the observed limit from data together with the ± 1 standard deviation contours corresponding to the uncertainties of the NLO+NLL cross section calculations. Similar dashed contours represent the expected limits and the ± 1 standard deviation experimental uncertainties. The white diagonal band near $m_{\tilde{\chi}_1^0} = 0$ GeV, which is excluded from the plot, corresponds to the region where the difference between the mass of the top squark and the neutralino is very close to the mass of the top quark ($|m_{\tilde{t}} - m_t - m_{\tilde{\chi}_1^0}| < 25$ GeV). The signal acceptance in this region varies greatly with the neutralino mass and is therefore difficult to model.

Table B1: The total number of predicted yields for the background and selected signal benchmark points and the observed data counts in the signal region for the W 4-5 jet category.

M_R (GeV)	R^2	Bg. Prediction	T5ttcc 2000 300	T2tt 1200 100	Observed
[800, 1000]	[0.08,0.12]	$16776.03 \pm 42.53^{+3119.40}_{-4751.61}$	$0.00 \pm 0.00^{+0.00}_{-0.00}$	$0.01 \pm 1.35^{+1.35}_{-0.01}$	21779
	[0.12,0.16]	$6477.91 \pm 29.29^{+1230.65}_{-1146.09}$	$0.15 \pm 0.31^{+0.31}_{-0.15}$	$0.70 \pm 0.48^{+0.45}_{-0.45}$	8977
	[0.16,0.24]	$7397.24 \pm 43.82^{+882.34}_{-1264.11}$	$0.00 \pm 0.00^{+0.00}_{-0.00}$	$1.64 \pm 0.63^{+0.71}_{-0.66}$	6272
	[0.24,0.40]	$3311.85 \pm 31.55^{+1003.72}_{-291.19}$	$0.21 \pm 0.35^{+0.38}_{-0.21}$	$5.34 \pm 1.15^{+1.41}_{-1.46}$	3030
	[0.40,1.50]	$976.92 \pm 14.06^{+80.83}_{-134.41}$	$2.13 \pm 0.75^{+0.97}_{-0.83}$	$17.44 \pm 2.52^{+3.26}_{-3.90}$	453
	[0.08,0.12]	$4398.37 \pm 26.56^{+1571.68}_{-669.38}$	$0.39 \pm 0.38^{+0.51}_{-0.38}$	$0.57 \pm 0.40^{+0.50}_{-0.30}$	5870
[1000, 1200]	[0.12,0.16]	$2904.44 \pm 20.44^{+1036.85}_{-432.67}$	$0.00 \pm 0.00^{+0.00}_{-0.00}$	$1.58 \pm 0.71^{+0.93}_{-0.72}$	2669
	[0.16,0.24]	$2515.66 \pm 20.59^{+381.63}_{-232.93}$	$0.21 \pm 0.21^{+0.45}_{-0.21}$	$2.09 \pm 0.73^{+0.80}_{-0.76}$	2046
	[0.24,0.40]	$1916.04 \pm 36.27^{+252.69}_{-682.54}$	$0.94 \pm 0.50^{+0.56}_{-0.58}$	$5.45 \pm 1.26^{+1.63}_{-1.77}$	1021
	[0.40,1.50]	$200.70 \pm 3.08^{+36.17}_{-25.78}$	$3.54 \pm 1.01^{+1.11}_{-1.07}$	$23.54 \pm 2.79^{+3.54}_{-3.62}$	208
	[0.08,0.12]	$4464.88 \pm 23.58^{+877.26}_{-1036.31}$	$0.45 \pm 0.29^{+0.29}_{-0.29}$	$2.47 \pm 0.79^{+0.87}_{-1.09}$	4330
	[0.12,0.16]	$1217.55 \pm 13.68^{+90.93}_{-173.93}$	$1.54 \pm 0.65^{+0.66}_{-0.84}$	$4.80 \pm 1.95^{+2.06}_{-2.08}$	1359
[1200, 1600]	[0.16,0.24]	$1229.02 \pm 14.25^{+109.24}_{-97.11}$	$1.19 \pm 0.54^{+0.68}_{-0.61}$	$5.85 \pm 1.35^{+1.46}_{-1.52}$	1112
	[0.24,0.40]	$587.12 \pm 8.72^{+55.67}_{-72.67}$	$3.45 \pm 0.94^{+1.00}_{-1.03}$	$16.46 \pm 2.28^{+2.62}_{-3.62}$	432
	[0.40,1.50]	$133.14 \pm 2.39^{+45.09}_{-38.96}$	$9.07 \pm 1.94^{+2.67}_{-2.06}$	$27.32 \pm 3.02^{+3.62}_{-4.63}$	0
	[0.08,0.12]	$1192.30 \pm 13.43^{+294.95}_{-311.07}$	$0.43 \pm 0.32^{+0.39}_{-0.32}$	$0.96 \pm 0.39^{+1.18}_{-0.94}$	593
	[0.12,0.16]	$579.10 \pm 25.82^{+96.63}_{-82.26}$	$1.22 \pm 0.47^{+0.66}_{-0.72}$	$2.35 \pm 0.83^{+1.09}_{-1.00}$	200
	[0.16,0.24]	$190.32 \pm 4.66^{+53.82}_{-73.53}$	$4.13 \pm 1.31^{+1.36}_{-1.44}$	$3.57 \pm 1.05^{+1.26}_{-1.54}$	96
[1600, 2000]	[0.24,1.50]	$127.22 \pm 3.42^{+59.80}_{-30.24}$	$19.93 \pm 2.39^{+3.17}_{-3.18}$	$13.98 \pm 2.80^{+3.13}_{-3.11}$	238
	[0.08,0.12]	$209.62 \pm 3.76^{+48.20}_{-56.79}$	$2.62 \pm 0.80^{+0.88}_{-0.93}$	$0.66 \pm 0.36^{+0.36}_{-0.56}$	91
	[0.12,0.16]	$78.16 \pm 1.75^{+40.80}_{-17.48}$	$2.39 \pm 0.81^{+0.87}_{-0.86}$	$1.80 \pm 0.83^{+0.84}_{-1.07}$	122
	[0.16,0.24]	$117.32 \pm 15.20^{+27.86}_{-63.04}$	$20.23 \pm 2.54^{+3.32}_{-2.99}$	$6.08 \pm 1.38^{+1.47}_{-1.55}$	0

Table B2: The total number of predicted yields for the background and selected signal benchmark points and the observed data counts in the signal region for the W 6 $_{\leq}$ jet category.

M_R (GeV)	R^2	Bg. Prediction	T1tttt 2000 300	T3ttcc 2000 300	T2tt 1200 100	Observed
[800, 1000]	[0.08,0.12]	$21791.12 \pm 89.18^{+3671.53}_{-3588.31}$	$0.24 \pm 5.85^{+5.85}_{-0.24}$	$0.00 \pm 0.00^{+0.00}_{-0.00}$	$1.05 \pm 10.07^{+10.08}_{-1.05}$	18668
	[0.12,0.16]	$9465.89 \pm 92.48^{+1165.38}_{-2539.62}$	$0.00 \pm 0.00^{+0.00}_{-0.00}$	$0.00 \pm 0.00^{+0.00}_{-0.00}$	$0.19 \pm 0.06^{+0.59}_{-0.19}$	5713
	[0.16,0.24]	$7940.64 \pm 94.43^{+1334.26}_{-742.78}$	$0.00 \pm 0.00^{+0.00}_{-0.00}$	$0.00 \pm 0.00^{+0.35}_{-0.00}$	$3.19 \pm 0.94^{+1.00}_{-1.05}$	6542
	[0.24,0.40]	$2845.60 \pm 20.83^{+160.70}_{-166.26}$	$0.35 \pm 0.25^{+0.26}_{-0.31}$	$1.65 \pm 0.56^{+0.74}_{-0.63}$	$5.79 \pm 1.39^{+1.48}_{-1.57}$	2275
[1000, 1200]	[0.40,1.50]	$704.70 \pm 10.83^{+104.71}_{-56.39}$	$0.69 \pm 0.35^{+0.47}_{-0.48}$	$1.51 \pm 0.62^{+0.63}_{-0.79}$	$12.18 \pm 1.75^{+2.02}_{-2.79}$	545
	[0.08,0.12]	$9030.73 \pm 54.75^{+1615.27}_{-1865.25}$	$0.00 \pm 0.00^{+0.00}_{-0.00}$	$0.27 \pm 0.26^{+0.29}_{-0.27}$	$1.45 \pm 0.60^{+0.68}_{-0.63}$	8794
	[0.12,0.16]	$5059.34 \pm 66.70^{+1007.04}_{-1979.14}$	$0.00 \pm 0.00^{+0.00}_{-0.00}$	$0.28 \pm 0.17^{+0.18}_{-0.28}$	$2.48 \pm 0.82^{+0.91}_{-0.89}$	3967
	[0.16,0.24]	$2152.60 \pm 33.88^{+302.77}_{-706.07}$	$0.50 \pm 0.33^{+0.33}_{-0.33}$	$1.78 \pm 0.74^{+0.89}_{-0.82}$	$5.60 \pm 1.40^{+2.01}_{-1.65}$	2359
[1200, 1600]	[0.24,0.40]	$1088.99 \pm 12.67^{+67.79}_{-85.38}$	$1.31 \pm 0.55^{+0.65}_{-0.60}$	$2.90 \pm 0.83^{+0.87}_{-0.99}$	$9.72 \pm 1.87^{+2.19}_{-2.57}$	1189
	[0.40,1.50]	$376.06 \pm 9.56^{+108.01}_{-48.17}$	$3.62 \pm 1.13^{+1.20}_{-1.32}$	$4.96 \pm 1.10^{+1.21}_{-1.60}$	$18.64 \pm 2.33^{+2.83}_{-2.77}$	404
	[0.08,0.12]	$8163.41 \pm 52.19^{+1079.33}_{-1411.77}$	$3.37 \pm 1.64^{+1.70}_{-1.70}$	$1.97 \pm 0.68^{+0.69}_{-0.73}$	$4.62 \pm 1.12^{+1.25}_{-1.43}$	6272
	[0.12,0.16]	$1624.77 \pm 14.53^{+158.42}_{-128.22}$	$2.17 \pm 0.73^{+0.84}_{-1.01}$	$1.81 \pm 0.72^{+0.81}_{-0.81}$	$5.96 \pm 1.26^{+1.54}_{-1.88}$	1761
[2000, 4000]	[0.16,0.24]	$1129.60 \pm 12.80^{+156.16}_{-155.93}$	$8.60 \pm 1.34^{+1.45}_{-1.45}$	$6.42 \pm 1.31^{+1.47}_{-1.58}$	$11.28 \pm 1.60^{+2.12}_{-2.54}$	1318
	[0.24,0.40]	$359.81 \pm 7.40^{+47.68}_{-30.45}$	$11.13 \pm 1.67^{+1.99}_{-2.09}$	$8.10 \pm 1.34^{+1.59}_{-2.21}$	$15.45 \pm 2.03^{+2.89}_{-2.97}$	711
	[0.40,1.50]	$211.02 \pm 9.43^{+20.89}_{-22.36}$	$14.10 \pm 2.39^{+3.02}_{-3.06}$	$17.46 \pm 2.13^{+2.66}_{-2.47}$	$20.80 \pm 2.36^{+3.92}_{-3.51}$	0
	[0.08,0.12]	$1059.43 \pm 10.51^{+208.24}_{-224.14}$	$5.34 \pm 1.22^{+1.33}_{-1.55}$	$2.45 \pm 0.63^{+0.80}_{-0.74}$	$5.51 \pm 1.23^{+1.44}_{-1.45}$	637
[1600, 2000]	[0.12,0.16]	$686.07 \pm 17.05^{+59.42}_{-101.05}$	$10.78 \pm 1.62^{+1.91}_{-2.22}$	$2.64 \pm 0.86^{+0.90}_{-0.95}$	$5.06 \pm 1.13^{+1.30}_{-1.30}$	654
	[0.16,0.24]	$280.86 \pm 6.99^{+84.62}_{-35.04}$	$15.63 \pm 2.21^{+2.88}_{-3.94}$	$6.60 \pm 1.14^{+1.29}_{-1.82}$	$8.66 \pm 1.64^{+2.95}_{-2.19}$	92
	[0.24,1.50]	$135.15 \pm 3.36^{+37.59}_{-20.63}$	$45.84 \pm 4.27^{+6.79}_{-6.25}$	$42.11 \pm 3.32^{+4.38}_{-5.50}$	$15.73 \pm 2.04^{+2.77}_{-4.89}$	0
	[0.08,0.12]	$181.48 \pm 3.46^{+67.43}_{-169.64}$	$15.95 \pm 1.94^{+2.86}_{-2.69}$	$6.47 \pm 1.25^{+1.57}_{-1.62}$	$5.84 \pm 1.16^{+1.63}_{-1.63}$	693
[2000, 4000]	[0.12,0.16]	$374.91 \pm 21.65^{+69.45}_{-90.77}$	$20.11 \pm 2.21^{+2.87}_{-2.75}$	$7.60 \pm 1.30^{+1.50}_{-1.57}$	$5.82 \pm 1.45^{+1.80}_{-2.21}$	228
	[0.16,1.50]	$272.02 \pm 8.34^{+34.51}_{-75.51}$	$80.03 \pm 4.37^{+8.26}_{-8.82}$	$44.37 \pm 3.73^{+6.42}_{-5.91}$	$11.10 \pm 1.78^{+2.92}_{-2.54}$	122

Table B3: The total number of predicted yields for the background and selected signal benchmark points and the observed data counts in the signal region for the *top* category.

M_R (GeV)	R^2	Bg. Prediction	T1tttt 2000 300	T5ttcc 2000 300	T2tt 1200 100	Observed
[800, 1000]	[0.08,0.12]	9513.48 ± 30.47 ^{+1809.24} _{-1714.58}	0.00 ± 0.00 ^{+0.00} _{-0.00}	0.00 ± 0.00 ^{+0.00} _{-0.00}	0.74 ± 8.78 ^{+8.78} _{-0.74}	3251
	[0.12,0.16]	2135.98 ± 17.10 ^{+236.88} _{-98.12}	0.00 ± 0.00 ^{+0.00} _{-0.00}	0.00 ± 0.00 ^{+0.00} _{-0.00}	0.62 ± 0.43 ^{+0.43} _{-0.47}	2236
	[0.16,0.24]	3446.99 ± 21.33 ^{+294.42} _{-347.89}	0.00 ± 0.00 ^{+0.00} _{-0.00}	0.00 ± 0.00 ^{+0.00} _{-0.00}	2.03 ± 0.77 ^{+0.84} _{-0.79}	3172
	[0.24,0.40]	3160.47 ± 22.62 ^{+189.00} _{-320.82}	0.13 ± 0.13 ^{+0.13} _{-0.13}	0.77 ± 0.38 ^{+0.42} _{-0.65}	8.24 ± 1.46 ^{+1.71} _{-1.52}	2832
	[0.40,1.50]	837.97 ± 7.69 ^{+75.34} _{-44.44}	0.45 ± 0.32 ^{+0.42} _{-0.32}	4.52 ± 1.05 ^{+1.13} _{-1.12}	26.05 ± 2.72 ^{+3.35} _{-4.33}	1569
[1000, 1200]	[0.08,0.12]	2642.07 ± 19.33 ^{+245.87} _{-307.88}	0.00 ± 0.00 ^{+0.00} _{-0.00}	0.50 ± 0.35 ^{+0.35} _{-0.35}	1.36 ± 0.68 ^{+0.68} _{-0.73}	2654
	[0.12,0.16]	1437.20 ± 10.32 ^{+303.09} _{-217.44}	0.00 ± 0.00 ^{+0.00} _{-0.00}	0.36 ± 0.23 ^{+0.23} _{-0.23}	4.93 ± 1.06 ^{+1.19} _{-1.34}	1470
	[0.16,0.24]	2347.83 ± 25.68 ^{+201.42} _{-181.98}	0.16 ± 0.16 ^{+0.16} _{-0.16}	0.84 ± 0.55 ^{+0.56} _{-0.56}	9.31 ± 1.65 ^{+1.71} _{-1.71}	1999
	[0.24,0.40]	480.08 ± 4.95 ^{+36.34} _{-44.38}	1.64 ± 0.59 ^{+0.60} _{-0.62}	2.82 ± 0.78 ^{+0.96} _{-0.79}	22.39 ± 2.50 ^{+3.09} _{-2.85}	1236
	[0.40,1.50]	246.92 ± 5.43 ^{+39.35} _{-33.66}	1.26 ± 0.53 ^{+0.57} _{-0.55}	4.70 ± 1.06 ^{+1.91} _{-1.16}	44.66 ± 3.65 ^{+5.48} _{-5.31}	212
[1200, 1600]	[0.08,0.12]	2280.19 ± 18.45 ^{+202.09} _{-125.39}	1.89 ± 0.70 ^{+0.76} _{-0.73}	1.41 ± 0.48 ^{+0.81} _{-0.82}	6.50 ± 1.30 ^{+1.40} _{-1.48}	1574
	[0.12,0.16]	1662.15 ± 13.83 ^{+120.84} _{-144.31}	1.84 ± 0.57 ^{+0.70} _{-0.81}	2.98 ± 0.86 ^{+0.91} _{-1.16}	11.05 ± 1.79 ^{+2.05} _{-1.91}	824
	[0.16,0.24]	1454.34 ± 17.58 ^{+121.33} _{-83.04}	5.81 ± 1.12 ^{+1.25} _{-1.24}	6.52 ± 1.28 ^{+1.41} _{-1.34}	32.53 ± 3.03 ^{+3.96} _{-3.42}	794
	[0.24,0.40]	589.75 ± 8.77 ^{+34.68} _{-52.94}	7.73 ± 1.30 ^{+1.52} _{-1.37}	17.37 ± 2.01 ^{+2.38} _{-2.62}	63.84 ± 4.31 ^{+6.51} _{-5.21}	205
	[0.40,1.50]	72.53 ± 1.17 ^{+12.89} _{-8.09}	8.04 ± 1.33 ^{+1.63} _{-1.45}	42.37 ± 3.26 ^{+4.92} _{-4.98}	81.67 ± 4.96 ^{+7.93} _{-6.19}	90
[1600, 2000]	[0.08,0.12]	814.42 ± 5.60 ^{+143.08} _{-316.33}	4.92 ± 0.90 ^{+1.09} _{-0.96}	3.51 ± 0.93 ^{+1.41} _{-1.00}	7.45 ± 1.39 ^{+1.50} _{-1.60}	599
	[0.12,0.16]	272.21 ± 5.02 ^{+27.62} _{-20.51}	7.72 ± 1.39 ^{+1.58} _{-1.46}	7.32 ± 1.32 ^{+1.53} _{-1.40}	14.78 ± 2.12 ^{+2.42} _{-2.55}	214
	[0.16,0.24]	375.56 ± 5.66 ^{+48.81} _{-61.48}	18.33 ± 1.95 ^{+2.39} _{-2.24}	15.98 ± 1.93 ^{+2.37} _{-2.18}	26.11 ± 2.72 ^{+3.57} _{-3.02}	99
	[0.24,1.50]	42.21 ± 0.66 ^{+26.58} _{-15.42}	47.88 ± 3.29 ^{+5.69} _{-4.59}	108.66 ± 5.28 ^{+10.01} _{-7.45}	71.08 ± 4.63 ^{+7.29} _{-5.63}	0
	[0.08,0.12]	101.45 ± 1.19 ^{+8.09} _{-11.48}	21.03 ± 2.14 ^{+2.92} _{-2.39}	21.30 ± 2.23 ^{+2.77} _{-2.51}	13.08 ± 2.03 ^{+2.77} _{-2.48}	94
[2000, 4000]	[0.12,0.16]	130.43 ± 5.00 ^{+19.66} _{-19.21}	28.28 ± 2.52 ^{+3.50} _{-2.99}	23.42 ± 2.46 ^{+3.46} _{-2.76}	13.70 ± 1.98 ^{+2.33} _{-2.35}	132
	[0.16,1.50]	59.75 ± 0.89 ^{+8.40} _{-19.02}	92.16 ± 4.51 ^{+8.40} _{-6.91}	171.69 ± 6.45 ^{+14.67} _{-11.27}	44.63 ± 3.63 ^{+5.74} _{-4.35}	117